

## MODULES FOR EXPERIMENTS IN STELLAR ASTROPHYSICS (MESA)

BILL PAXTON<sup>1</sup>, LARS BILDSTEN<sup>1</sup>, AARON DOTTER<sup>2,5</sup>, FALK HERWIG<sup>2</sup>, PIERRE LESAFFRE<sup>3</sup>, AND FRANK TIMMES<sup>4</sup>

<sup>1</sup> Kavli Institute for Theoretical Physics and Department of Physics, Kohn Hall, University of California, Santa Barbara, CA 93106, USA

<sup>2</sup> Department of Physics and Astronomy, University of Victoria, P.O. Box 3055, STN CSC, Victoria, BC V8W 3P6, Canada

<sup>3</sup> LERMA-LRA, CNRS UMR8112, Observatoire de Paris and Ecole Normale Supérieure, 24 Rue Lhomond, 75231 Paris Cedex 05, France

<sup>4</sup> School of Earth and Space Exploration, Arizona State University, P.O. Box 871404, Tempe, AZ 85287-1404, USA

Received 2010 September 4; accepted 2010 November 5; published 2010 December 15

### ABSTRACT

Stellar physics and evolution calculations enable a broad range of research in astrophysics. Modules for Experiments in Stellar Astrophysics (MESA) is a suite of open source, robust, efficient, thread-safe libraries for a wide range of applications in computational stellar astrophysics. A one-dimensional stellar evolution module, MESA star, combines many of the numerical and physics modules for simulations of a wide range of stellar evolution scenarios ranging from very low mass to massive stars, including advanced evolutionary phases. MESA star solves the fully coupled structure and composition equations simultaneously. It uses adaptive mesh refinement and sophisticated timestep controls, and supports shared memory parallelism based on OpenMP. State-of-the-art modules provide equation of state, opacity, nuclear reaction rates, element diffusion data, and atmosphere boundary conditions. Each module is constructed as a separate Fortran 95 library with its own explicitly defined public interface to facilitate independent development. Several detailed examples indicate the extensive verification and testing that is continuously performed and demonstrate the wide range of capabilities that MESA possesses. These examples include evolutionary tracks of very low mass stars, brown dwarfs, and gas giant planets to very old ages; the complete evolutionary track of a  $1 M_{\odot}$  star from the pre-main sequence (PMS) to a cooling white dwarf; the solar sound speed profile; the evolution of intermediate-mass stars through the He-core burning phase and thermal pulses on the He-shell burning asymptotic giant branch phase; the interior structure of slowly pulsating B Stars and Beta Cepheids; the complete evolutionary tracks of massive stars from the PMS to the onset of core collapse; mass transfer from stars undergoing Roche lobe overflow; and the evolution of helium accretion onto a neutron star. MESA can be downloaded from the project Web site (<http://mesa.sourceforge.net/>).

*Key words:* methods: numerical – stars: evolution – stars: general

*Online-only material:* color figures

### CONTENTS

1. INTRODUCTION	2
2. MODULE DESIGN AND IMPLEMENTATION	3
3. NUMERICAL METHODS	3
4. MICROPHYSICS	4
4.1. Mathematical Constants, Physical and Astronomical Data	4
4.2. Equation of State	4
4.3. Opacities	6
4.4. Thermonuclear and Weak Reactions	8
4.5. Nuclear Reaction Networks	8
5. MACROPHYSICS	8
5.1. The Mixing Length Theory of Convection	8
5.2. Convective Overshoot Mixing	9
5.3. Atmosphere Boundary Conditions	10
5.4. Diffusion and Gravitational Settling	10
5.5. Testing MESA Modules in an Existing Stellar Evolution Code	11
6. STELLAR STRUCTURE AND EVOLUTION	11
6.1. Starting Models and Basic Input/Output	12
6.2. Structure and Composition Equations	13
6.3. Convergence to a Solution	14
6.4. Timestep Selection	14
6.5. Mesh Adjustment	14
6.6. Mass Loss and Accretion	15
6.7. Resolution Sensitivity	16
6.8. Multithreading	16
6.9. Visualization with PGstar	17
7. MESA star RESULTS: COMPARISONS AND CAPABILITIES	17
7.1. Low-mass Stellar Structure and Evolution	18
7.1.1. Low-mass Pre-main Sequence Stars, Contracting Brown Dwarfs and Giant Planets	18

7.1.2. Code Comparisons of $0.8 M_{\odot}$ and $1 M_{\odot}$ Models	20
7.1.3. The MESA star Solar Model	20
7.2. Intermediate-mass Structure and Evolution	20
7.2.1. Comparison of EVOL and MESA star	21
7.2.2. Interior Structure of Slowly Pulsating B Stars and Beta Cepheids	22
7.3. High Mass Stellar Structure and Evolution	23
7.3.1. $25 M_{\odot}$ Model Comparisons	23
7.3.2. Comparison of 15, 20, and $25 M_{\odot}$ Models	24
7.3.3. $1000 M_{\odot}$ Metal-free Star Capabilities	25
7.4. Stellar Evolution with Mass Transfer	25
7.4.1. Mass Transfer in a Binary	26
7.4.2. Rapid Helium Accretion onto a Neutron Star	26
8. SUMMARY AND CONCLUSION	27
APPENDIX A. MANIFESTO	28
A.1. Motivation for a New Tool	28
A.2. MESA Philosophy	28
A.3. Establishment of the MESA Council	29
APPENDIX B. CODE TESTING AND VERIFICATION	29

## 1. INTRODUCTION

Much of the information that astronomers use to study the universe comes from starlight. Interpretation of that starlight requires a detailed understanding of stellar astrophysics, especially as it relates to stellar atmospheres, structure, and evolution. Stellar structure and evolution models underpin much of modern astrophysics as they are used to analyze: the Sun through helioseismology (e.g., Bahcall et al. 1998), the pulsational properties of many nearby stars with asteroseismic data from, e.g., *CoRot* (Degrroote et al. 2009) and *Kepler* (Gilliland et al. 2010), the color–magnitude diagrams of resolved stellar and sub-stellar populations in the Milky Way and nearby galaxies (e.g., VandenBerg 2000; Dotter et al. 2010), the integrated light of distant galaxies and star clusters via population synthesis techniques (e.g., Worthey 1994; Coelho et al. 2007), stellar yields and galactic chemical evolution (e.g., Timmes et al. 1995), physics of the first stars (Fujimoto et al. 2000), and a variety of aspects in time domain astrophysics (e.g., LSST<sup>6</sup>).

Stellar evolution is broadly recognized as the first key problem in computational astrophysics. The introduction of electronic computers enabled the solution of the highly nonlinear, coupled differential equations of stellar structure and evolution, and the first detailed reports of computer programs for stellar evolution soon appeared (Iben & Ehrman 1962; Henyey et al. 1964; Hofmeister et al. 1964; Kippenhahn et al. 1967). Implicit in the development of these codes was a sufficiently mature theoretical understanding of stars (Chandrasekhar 1939; Schwarzschild 1958, see as well the compilation of references later in this section), development of a concise yet sufficiently accurate treatment of convection (Böhm-Vitense 1958), as well as a better understanding of the properties of stellar matter, including nucleosynthesis (Burbridge et al. 1957; Cameron 1957). Further improvements and alternative implementations became available addressing, for example, the numerical stability of computations (Sugimoto 1970), more efficient methods for following shell burning in low-mass stars (Eggleton 1971), and the hydrodynamics of advanced burning in massive stars (Weaver et al. 1978). Progress continues on stellar evolution codes, with

code developments and comparisons often facilitated by the opening of new observational windows. For example, the participants (Christensen-Dalsgaard 2008; Degl’Innocenti et al. 2008; Demarque et al. 2008; Eggenberger et al. 2008; Hui-Bon-Hoa 2008; Morel & Lebreton 2008; Roxburgh 2008; Scuflaire et al. 2008; Ventura et al. 2008; Weiss & Schlattl 2008) in the *CoRot* Evolution and Seismic Tools Activity (Lebreton et al. 2008) are a representative sample of the active community.

Modules for Experiments in Stellar Astrophysics (MESA) began as an effort to improve upon the EZ stellar evolution code (Eggleton 1971; Paxton 2004). It employs modern software engineering tools and techniques to target modern computer architectures that are significantly different from those available to the pioneers half a century ago. As the pieces of the new system started to emerge, it became clear that the parts would be of greater value than the whole if they were carefully structured for independent use. MESA includes a new one-dimensional stellar evolution code, MESA star, but is designed to be useful for a wide range of stellar physics applications. The physical inputs to stellar evolution models, such as the equation of state (EOS), opacities, and nuclear reaction networks, have a broader application than stellar evolution calculations alone. MESA is designed so that each of the individual components is usable on its own, with the intention of facilitating verification test suites among different codes and encouraging new computational experiments in stellar astrophysics.

MESA star approaches stellar physics, structure, and evolution with modern, sophisticated numerical methods and updated physics that give it a very wide range of applicability. The numerical and computational methods employed allow MESA star to consistently evolve stellar models through challenging phases, e.g., the He core flash in low-mass stars and advanced nuclear burning in massive stars, that have posed substantial challenges for stellar evolution codes in the past.

MESA is open source: anyone can download the source code, compile it, and run it for their own research or education purposes. It is meant to engage the broader community of astrophysicists in related fields and encourage contributions in the form of testing, finding and fixing bugs, adding new capabilities, and, generally, sharing experience with the MESA community. The philosophy and guidelines of MESA are described in more detail in the MESA manifesto (see Appendix A).

<sup>5</sup> Current address: Space Telescope Science Institute, 3700 San Martin Drive, Baltimore, MD 21218, USA.

<sup>6</sup> <http://www.lsst.org/lsst/scibook>

This paper serves as an introduction to MESA and demonstrates its current capabilities. We assume that the reader is familiar with the basic stellar physics and numerical methods, both of which are essential to arrive at meaningful solutions when using MESA. For background material we refer the reader to Eddington (1926), Chandrasekhar (1939), Schwarzschild (1958), Cox & Giuli (1968), Clayton (1984), Iben (1991), Press et al. (1992), Hansen & Kawaler (1995), Arnett (1996), and Kippenhahn & Weigert (1996).

The MESA codebase is in constant development, and future capabilities and applications will be detailed in subsequent papers. The paper is outlined as follows. Section 2 explains the design and implementation of MESA modules; Sections 3–5 describe the numerical, microphysics, and macrophysical modules; Section 6 describes the stellar evolution module MESA star; Section 7 presents a series of tests and code comparisons that serve as rudimentary verification and demonstrates the broader capabilities of MESA star; and Section 8 summarizes the material presented.

## 2. MODULE DESIGN AND IMPLEMENTATION

Each MESA module is responsible for a different aspect of numerics or physics required to construct computational models for stellar astrophysics. Each has a similar organization: a public interface, a private implementation, a makefile to create a library, and a test suite for verification. Each module includes an installation script that builds the library, tests it, and, if the test succeeds, exports it to the MESA libraries directory. Comparisons between local and expected results are carried out with the open source `ndiff` utility.<sup>7</sup> There is a global install script for MESA that performs the installation of each of the modules in the required order to satisfy dependencies. The installation on UNIX-like systems, including Linux and Mac OS X requires a modern, up-to-date Fortran compiler.<sup>8</sup> A template module, `package_template`, exists for initiation of new modules by the community. Variable definitions are given in Table 1, and all current MESA modules are listed in Table 2, along with the function they perform and the section in this paper where the description resides.

The MESA modules are “thread-safe”—meaning that more than one process can execute the module routines at the same time—allowing applications to utilize multicore processors. A module is thread-safe if all of its shared data are read-only after initialization. This has been accomplished in MESA by eliminating common blocks and SAVE statements and instead using local variables or dynamic allocation for all working memory. Evaluations of local microphysics, such as the EOS, opacity, and nuclear reaction networks can be carried out in parallel using the OpenMP application programming interface.<sup>9</sup> The capability of MESA star to take advantage of multithreading is discussed in Section 6.8.

## 3. NUMERICAL METHODS

MESA includes several modules that provide numerical methods. The following briefly describes each one presently available and references the relevant literature (or Web-based resource) where the full description resides.

<sup>7</sup> See <http://www.math.utah.edu/~beebe/software/ndiff/>. MESA installs its own copy of `ndiff` the first time the main installation process is performed.

<sup>8</sup> Information about supported compilers and installation is provided on the MESA project Web site, <http://mesa.sourceforge.net>.

<sup>9</sup> <http://openmp.org>

**Table 1**  
Variable Index

Name	Description	First Appears
A	Atomic mass number	Section 4.4
$a$	Acceleration at the cell face	Section 6.2
$\alpha$	Order of convergence	Section 6.7
$\alpha_{\text{MLT}}$	Mixing length parameter	Section 5.1
C	“Spacetime” parameter for convergence study	Section 6.7
$C_P$	Specific heat at constant pressure	Section 4.2
$C_V$	Specific heat at constant volume	Section 4.2
$c_s$	Sound speed	Section 7.2.2
$X_P$	$\equiv d\ln P/d\ln\rho _T$	Section 4.2
$X_T$	$\equiv d\ln P/d\ln T _\rho$	Section 4.2
D	Eulerian diffusion coefficient	Section 5.2
$D_{\text{OV}}$	Overshoot diffusion coefficient	Section 5.2
$\Delta$	Grid difference	Section 6.5
$\delta$	Time difference	Section 6.5
$dm$	Mass of a cell	Section 6.2
$dP_s$	$P$ difference between surface and center of first cell	Section 6.2
$dT_s$	$T$ difference in between surface and center of first cell	Section 6.2
$\delta t$	Timestep	Section 6.4
E	Energy	Section 4.2
$e_{\text{nuc}}$	Nuclear energy generation in erg g <sup>-1</sup>	Section 4.5
$\epsilon$	Power per unit mass (nuclear, thermal neutrino, gravity)	Section 6.2
$\epsilon_F$	Fermi energy	Section 7.1
F	Mass flow rate	Section 6.2
f	Overshoot mixing parameter	Section 5.2
g	Local gravity	Section 5.1
$\Gamma_1$	$\equiv d\ln P/d\ln\rho _S$	Section 4.2
$\Gamma$	Coulomb coupling parameter	Section 4.2
$\Gamma_3$	$\equiv d\ln T/d\ln\rho _S + 1$	Section 4.2
$\nabla_{\text{ad}}$	Adiabatic temperature gradient	Section 4.2
$\nabla_{\text{rad}}$	Radiative temperature gradient	Section 5.1
$\nabla_T$	Actual temperature gradient	Section 5.1
$\kappa_s$	Opacity at the surface of the outermost cell	Section 5.3
L	Total luminosity	Section 5.1
$L_{\text{conv}}$	Convective luminosity	Section 5.1
$\Lambda$	Mixing length ( $\alpha_{\text{MLT}}\lambda_P$ )	Section 5.1
$\lambda_P$	Pressure scale height	Section 5.1
m	Mass interior to cell	Section 6.2
$M_c$	Inner mass (not modeled) for central BC	Section 6.6
$M_m$	Modeled mass	Section 6.6
$\mu$	Mean molecular weight per gas particle	Section 4.2
$\mu_e$	Mean molecular weight per electron	Section 4.2
N	Brunt–Väisälä frequency	Section 7.2.2
$\eta$	Dimensionless electron degeneracy parameter	Section 6.5
P	Total pressure	Section 4.2
$P_{\text{gas}}$	Gas pressure	Section 4.2
$P_s$	Pressure at surface of outermost cell	Section 5.3
q	Relative mass coordinate	Section 6.6
$\rho$	Density	Section 4.2
R	Total radius	Section 5.1
$R_{\text{CZ}}$	Radius of the base of the solar convective zone	Section 7.1
r	Radius at the cell face	Section 6.2
S	Entropy	Section 4.2
$\sigma$	Lagrangian diffusion coefficient	Section 5.1
T	Temperature	Section 4.2
$T_s$	Temperature at surface of outermost cell	Section 5.3
$T_{\text{eff}}$	Effective temperature	Section 5.3
$\tau_s$	Optical depth at the surface of the outermost cell	Section 5.3
$\tau$	Optical depth	Section 5.3
v	Velocity at the cell face	Section 6.2

**Table 1**  
(Continued)

Name	Description	First Appears
$v_c$	Timestep control target	Section 6.4
$v_{\text{conv}}$	Convective velocity	Section 5.1
$v_t$	Timestep control variable	Section 6.4
$w$	Diffusion velocity	Section 5.4
$X$	H mass fraction	Section 4.2
$X_i$	Mass fraction of the $i$ th isotope	Section 6.2
$\xi$	Relative difference in convergence study	Section 6.7
$Y$	He mass fraction	Section 4.3
$Y_e$	Electrons per baryon ( $\bar{Z}/\bar{\Lambda}$ )	Section 7.3
$Z$	Metals' mass fraction ( $1 - X - Y$ )	Section 4.2
$Z$	Atomic number	Section 5.4
$z$	Distance from convective boundary	Section 5.2

The `mtx` module provides an interface to linear algebra routines for matrix manipulation. A large set of BLAS and LAPACK routines are included, but the `mtx` module can easily be modified to accept these routines from other linear algebra packages, e.g., GotoBLAS<sup>10</sup> or the Intel Math Kernel Library<sup>11</sup> (MKL). Sparse matrix operations are supported, including a subset of the SPARSKIT sparse matrix iterative solver<sup>12</sup> and an interface to the Intel version of the PARDISO sparse matrix direct solver. The routines in `num` make use of these matrix routines.

Modules `interp_1d` and `interp_2d` deal with one-dimensional and two-dimensional interpolation, respectively. One-dimensional interpolation is carried out using either a piecewise monotonic cubic method (Huynh 1993; Suresh & Huynh 1997) or a monotonicity-preserving method (Steffen 1990). Compared with the piecewise monotonic method, the monotonicity-preserving method is stricter and does not allow an interpolated value to range outside of the given values (Steffen 1990). Module `interp_2d` includes parts of the PSPLINE package<sup>13</sup> and routines by both Akima (1996) and Renka (1999) for bivariate interpolation and surface fitting on a grid or with a scattered set of data points. Both single- and double-precision versions of the two-dimensional interpolation routines are provided.

Module `num` provides a variety of solvers for stiff and non-stiff systems of ordinary differential equations (ODEs) and a Newton–Raphson solver for multidimensional, nonlinear root finding. The family of ODE solvers is derived from the routines of Hairer & Wanner (1996). The non-stiff ODE class are explicit Runge–Kutta integrators of orders 5 and 8 with dense output, automatic stepsize control, and optional monitoring for stiffness. The stiff ODE solvers are linearly implicit Runge–Kutta, with second-, third-, and fourth-order versions and two implicit extrapolation integrators of variable order: either midpoint or Euler. All integrators support dense, banded, or sparse matrix routines, analytic or numerical difference Jacobians, explicit or implicit ODE systems, dense output, and automatic stepsize control.

The Newton–Raphson solver for multidimensional, nonlinear root finding supports square, banded, and sparse matrices and analytic or automatic numerical differencing for the Jacobians. It has the ability to reuse Jacobians and employs a line search

method to give improved convergence. The multidimensional Newton–Raphson solver is used by MESA `star` to solve highly nonlinear systems of differential-algebraic equations with tens of thousands of variables (see Section 6). The structure of the Newton–Raphson solver is derived from Lesaffre's version of the Eggleton stellar evolution code (Eggleton 1971; Pols et al. 1995; Lesaffre et al. 2006) and some details of the implementation will be described in Section 6.

The `alert` module provides a framework for reporting messages, including errors, to the terminal. The `utils` module provides a number of functions for checking if a variable has been assigned a bad value (e.g., NaN or infinity) and tracking Fortran I/O unit numbers in use. It also provides subroutines for basic file I/O and for allocating arrays of different types and dimensions, including a Fortran implementation of a hash tree that is used by the stellar evolution module to update the model mesh. Programs and scripts that are used for testing that each module has compiled correctly are stored in `utils`.

## 4. MICROPHYSICS

The MESA microphysics modules provide the physical properties of stellar matter, with each module focusing on a separate aspect of the physics. As a general note, “log” in this paper refers to the base-10 logarithm; where the natural logarithm is intended we have used “ln.”

### 4.1. Mathematical Constants, Physical and Astronomical Data

The MESA module `const` contains mathematical, physical, and astronomical constants relevant to stellar astrophysics in cgs units. The primary source for physical constants is the CODATA Recommended Values of the Fundamental Physical Constants (Mohr et al. 2008). Values for the solar age, mass, radius, and luminosity are taken from Bahcall et al. (2005).

The MESA module `chem` is a collection of data, functions, and subroutines to manage the chemical elements and their isotopes. It contains basic information about the chemical elements and their isotopes from hydrogen through uranium. It includes routines for translating between atomic weights and numbers and isotope names. It contains full listings of solar abundances on several scales (Anders & Grevesse 1989; Grevesse & Noels 1993; Grevesse & Sauval 1998; Lodders 2003; Asplund et al. 2005). Module `chem` contains a framework for the user to provide an arbitrary set of species in a text file.

### 4.2. Equation of State

The EOS is delivered by the `eos` module. It works with density,  $\rho$ , and temperature,  $T$ , as independent variables. These are the natural variables in a Helmholtz free energy formulation of the thermodynamics. However, as some calculations are more naturally performed using pressure,  $P$ , and  $T$  (as in a Gibbs free energy formulation), a simple root find can provide  $\rho$  given the desired  $P_{\text{gas}} = P - aT^4/3$  and  $T$ . While conceptually simple, this can impose a substantial computational overhead if done for each `eos` call. To alleviate this computational burden, the root finds are pre-processed, creating a set of tables indexed by  $P_{\text{gas}}$  and  $T$ . As a result, the runtime cost of evaluating `eos` using  $P_{\text{gas}}$  and  $T$  is the same as for using  $\rho$  and  $T$ , as long as the  $P_{\text{gas}} - T$  requests are within the pre-computed ranges. When outside those ranges, the root find is performed during runtime, slowing the computations.

The MESA  $\rho$ – $T$  tables are based on the 2005 update of the OPAL EOS tables (Rogers & Nayfonov 2002). To extend to

<sup>10</sup> <http://www.tacc.utexas.edu/resources/software>

<sup>11</sup> <http://software.intel.com/en-us/intel-mkl/>

<sup>12</sup> <http://www-users.cs.umn.edu/~saad/software/SPARSKIT/sparskit.html>

<sup>13</sup> <http://w3.pppl.gov/NTCC/PSPLINE>

**Table 2**  
MESA Module Definitions and Purposes

Name	Type	Purpose	Section
alert	Utility	Error handling	3
atm	Microphysics	Gray and non-gray atmospheres; tables and integration	5.3
const	Utility	Numerical and physical constants	4.1
chem	Microphysics	Properties of elements and isotopes	4.1
diffusion	Macrophysics	Gravitational settling and chemical and thermal diffusion	5.4
eos	Microphysics	Equation of state	4.2
interp_1d	Numerics	One-dimensional interpolation routines	3
interp_2d	Numerics	Two-dimensional interpolation routines	3
ionization	Microphysics	Average ionic charges for diffusion	5.4
jina	Macrophysics	Large nuclear reaction nets using reaclib	4.5
kap	Microphysics	Opacities	4.3
karo	Microphysics	Alternative low- $T$ opacities for C and N enhanced material	4.3
mlt	Macrophysics	Mixing length theory	5.1
mtx	Numerics	Linear algebra matrix solvers	3
net	Macrophysics	Small nuclear reaction nets optimized for performance	4.5
neu	Microphysics	Thermal neutrino rates	4.5
num	Numerics	Solvers for ordinary differential and differential-algebraic equations	3
package_template	Utility	Template for creating a new MESA module	2
rates	Microphysics	Nuclear reaction rates	4.4
screen	Microphysics	Nuclear reaction screening	4.5
star	Evolution	One-dimensional stellar evolution	6
utils	Utility	Miscellaneous utilities	3
weaklib	Microphysics	Rates for weak nuclear reactions	4.5

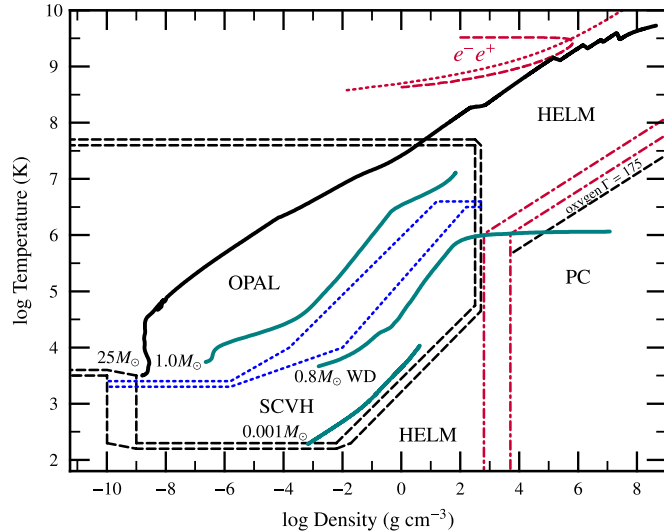


**Figure 1.**  $\rho$ - $T$  coverage of the equations of state used by the eos module for  $Z \leq 0.04$ . Inside the region bounded by the black dashed lines we use MESA EOS tables that were constructed from the OPAL and SCVH tables. The OPAL and SCVH tables were blended in the region shown by the blue dotted lines, as described in the text. Regions outside of the black dashed lines utilize the HELM and PC EOSs, which, respectively, incorporate electron–positron pairs at high temperatures and crystallization at low temperatures. The blending of the MESA table and the HELM/PC results occurs between the black dashed lines and is described in the text. The dotted red line shows where the number of electrons per baryon has doubled due to pair production, and the region to the left of the dashed red line has  $\Gamma_1 < 4/3$ . The very low density cold region in the leftmost part of the figure is treated as an ideal, neutral gas. The region below the black dashed line labeled as  $\Gamma = 175$  would be in a crystalline state for a plasma of pure oxygen and is fully handled by the PC EOS. The red dot-dashed line shows where MESA blends the PC and HELM EOSs. The green lines show stellar profiles for a main-sequence star ( $M = 1.0 M_\odot$ ), a contracting object of  $M = 0.001 M_\odot$ , and a cooling white dwarf of  $M = 0.8 M_\odot$ . The heavy dark line is an evolved  $25 M_\odot$  star that has a maximum infalling speed of  $1000 \text{ km s}^{-1}$ . The jagged behavior reflects the distinct burning shells.

(A color version of this figure is available in the online journal.)

lower temperatures and densities, we use the SCVH tables (Saumon et al. 1995) and construct a smooth transition between these tables in the overlapping region that we define (shown by the blue dotted lines in Figure 1). The limited thermodynamic information available from these EOSs restricts our blending to the output quantities listed in Table 3. The resulting MESA tables are more finely gridded than the original tables (so that no information is lost) and are provided at six  $X$  and three  $Z$  values:  $X = (0.0, 0.2, 0.4, 0.6, 0.8, 1.0)$  and  $Z = (0.0, 0.02, 0.04)$  in keeping with the OPAL tables, allowing for Helium rich compositions. In order to save space, the MESA tables are not rectangular in the independent variables. Instead, the region occupied by usual stellar models is roughly rectangular in the stellar modeling motivated variables,  $\log T$  and  $\log Q = \log \rho - 2 \log T + 12$ . The range in  $\log T$  is from 2.1 to 8.2 in steps of 0.02 and the range in  $\log Q$  is from −10.0 to 5.69 in steps of 0.03. Partials with  $\log T$  and  $\log Q$  are derived from the interpolating polynomials, while partials with respect to  $\log \rho$  then follow. The resulting region of these MESA tables is that inside of the dashed black lines of Figure 1. The MESA  $P_{\text{gas}}-T$  tables are rectangular in  $\log T$  and  $\log W = \log P_{\text{gas}} - 4 \log T$  over a range  $-17.2 \leq \log W \leq -2.9$  and  $2.1 \leq \log T \leq 8.2$ .

Outside the region covered by the MESA tables, the HELM (Timmes & Swesty 2000), and PC (Potekhin & Chabrier 2010) EOSs are employed. Both HELM and PC assume complete ionization and were explicitly constructed from a free energy approach, guaranteeing thermodynamic consistency. In nearly all cases, the full ionization assumption is appropriate since the OPAL and SCVH tables are used at those cooler temperatures where partial ionization is significant.<sup>14</sup> Since the MESA tables are only constructed for  $Z \leq 0.04$ , eos uses HELM and PC for  $Z > 0.04$  in the whole  $\rho$ - $T$  plane.

HELM was constructed for high temperatures (up to  $\log T = 13$ ) and densities (up to  $\log \rho = 15$ ), and accounts for the onset

<sup>14</sup> We discuss the ionization states of trace heavy elements in Section 5.4.

**Table 3**  
eos Output Quantities and Units

Output	Definition	Units
$P_{\text{gas}}$	Gas pressure	$\text{erg cm}^{-3}$
$E$	Internal energy	$\text{erg g}^{-1}$
$S$	Entropy per gram	$\text{erg g}^{-1} \text{K}^{-1}$
$dE/d\rho _T$		$\text{erg cm}^3 \text{g}^{-2}$
$C_V$	Specific heat at constant $V \equiv 1/\rho$	$\text{erg g}^{-1} \text{K}^{-1}$
$dS/d\rho _T$		$\text{erg cm}^3 \text{g}^{-2} \text{K}^{-1}$
$dS/dT _\rho$		$\text{erg g}^{-1} \text{K}^{-2}$
$\chi_\rho$	$\equiv d\ln P/d\ln\rho _T$	None
$\chi_T$	$\equiv d\ln P/d\ln T _\rho$	None
$C_P$	Specific heat at constant pressure	$\text{erg g}^{-1} \text{K}^{-1}$
$\nabla_{\text{ad}}$	Adiabatic $T$ gradient with pressure	None
$\Gamma_1$	$\equiv d\ln P/d\ln\rho _S$	None
$\Gamma_3$	$\equiv d\ln T/d\ln\rho _S + 1$	None
$\eta$	Ratio of electron chemical potential to $k_B T$	None
$\mu$	Mean molecular weight per gas particle	None
$1/\mu_e$	Mean number of free electrons per nucleon	None

of electron–positron pair production at high temperatures. The dotted red line in Figure 1 shows where the number of electrons per baryon has doubled due to pair production. The domination of pairs in the plasma creates a region where  $\Gamma_1 < 4/3$  (to the left of the dashed red line). The blending region to HELM (from the MESA tables) is shown by the black dashed lines in Figure 1 and can be modified by the user. In this transition region, the blend of the two EOSs is performed in a way that preserves thermodynamic consistency. Therefore, if each separate EOS satisfies Maxwell’s relations, the blend will also satisfy them. To accomplish this, we linearly sum the EOS quantities  $Q_i$  (i.e.,  $P$ ,  $E$ ,  $S$  and their partial derivatives with respect to  $\rho$  and  $T$ ) needed to satisfy Maxwell’s relations (Timmes & Swesty 2000).<sup>15</sup> The blend is calculated by defining the boundary limits, inside of which we define a fractional “distance,”  $F$ , from the boundary. As  $F$  varies from 0 to 1, we use the smoothing function  $S = (1 - \cos(F\pi))/2$  and for each of the nine quantities we construct  $Q_i = SQ_i^A + (1 - S)Q_i^B$ , where  $Q_i^A$  and  $Q_i^B$  are the outputs from the two EOSs. We then use these to rederive the thermodynamic quantities ( $\chi_\rho$ ,  $\chi_T$ ,  $C_P$ ,  $\nabla_{\text{ad}}$ ,  $\Gamma_3$ ,  $\Gamma_1$ ) delivered by the eos routine.

In late stages of the cooling of white dwarfs, the ions in the core will crystallize. For pure oxygen, the crystallization limit corresponds to a value of the Coulomb coupling parameter,  $\Gamma \approx 175$ , shown by the black dashed line in Figure 1. In this region, we use the PC EOS, which accounts for the modified thermodynamics of a crystal, as well as carefully handling mixtures (e.g., carbon and oxygen). The blend between PC and HELM (as shown by the dot-dashed red lines in Figure 1) is performed in the same manner as described above. In the dense liquid realm, the blending region is defined by the Coulomb coupling parameter,  $\Gamma = \bar{Z}^2 e^2 / a_i k_B T$ , where  $a_i$  is the mean ion spacing, and  $\bar{Z}$  is the average ion charge. The default choice is PC for  $\Gamma > 80$  and HELM for  $\Gamma < 40$ . The PC EOS is not constructed for arbitrarily low densities, forcing a transition to HELM at  $\log \rho < 2.8$ , with the blend beginning at  $\log \rho = 3.7$ . These boundaries may be re-defined by the user if needed.

In addition to the two independent variables, the eos module requires as input  $X$ ,  $Z$ ,  $\bar{A}$  (the mass-averaged atomic weight of metals) and  $\bar{Z}$  (the mass-averaged atomic charge of metals).

<sup>15</sup> The more conventional forms of these nine thermodynamic quantities are displayed in the first nine rows in Table 3.

When operating in the regime where the PC EOS is implemented, the mass fractions for all isotopes with mass fractions above a specified minimum are needed (default is 0.01), allowing PC to correctly handle isotope mixtures. It returns a total of 16 quantities (listed in Table 3) as well as the partial derivatives of each quantity with respect to the independent variables. The tables are interpolated in the independent variables using bicubic splines from interp\_2d with partial derivatives determined from the splines. Separate quadratic interpolations are performed in  $X$  and  $Z$ .

The construction of eos tables as outlined above is the default option for MESA but the eos module has the flexibility to accept tables from any source so long as the tables conform to the MESA standard format. For example, the comparison with the Stellar Code Calibration project (Weiss et al. 2007) described in Section 7.1.2 utilizes tables constructed using FreeEOS.<sup>16</sup> The FreeEOS code does not cover the same range of  $\rho$  and  $T$  as SCVH+OPAL+HELM but the eos module is designed with this flexibility in mind: the table dimensions are specified in the table headers and the module dynamically allocates arrays of the appropriate size to hold them when the tables are read in.

Since not all EOS sources may be in the tabular form desired by eos, we have created a module, other\_eos, that provides the user an opportunity to incorporate their own EOS and use it with the stellar evolution module MESA\_star.

#### 4.3. Opacities

The pre-processor make\_kap resides within the kap module and constructs the MESA opacity tables by combining radiative opacities with the electron conduction opacities from Cassisi et al. (2007). In the rare circumstances where  $\rho$  or  $T$  are outside the region covered by Cassisi et al. (2007) ( $-6 \leq \log \rho \leq 9.75$  and  $3 \leq \log T \leq 9$ ), the Iben (1975) fit to the Hubbard & Lampe (1969) electron conduction opacity is used for non-degenerate cases, while the Yakovlev & Urpin (1980) fits are used for degenerate cases. Radiative opacities are taken from Ferguson et al. (2005) for  $2.7 \leq \log T \leq 4.5$  and OPAL (Iglesias & Rogers 1993, 1996) for  $3.75 \leq \log T \leq 8.7$ . The low  $T$  opacities of Ferguson et al. (2005) include the effects of molecules and grains on the radiative opacity. Tables from OP (Seaton et al. 2005) can be used in place of OPAL as the table format is identical. The radiative opacity is dominated by Compton scattering for  $\log T > 8.7$  and is calculated using the equations of Buchler & Yueh (1976) up to a density of  $10^6 \text{ g cm}^{-3}$ . We use the HELM EOS to calculate the increasing number of electrons and positrons per baryon when pair production becomes prevalent, an important opacity enhancement.

The OPAL tables with fixed metal distributions are called Type 1 (Iglesias & Rogers 1993, 1996) and cover the region  $0.0 \leq X \leq 1 - Z$  and  $0.0 \leq Z \leq 0.1$ . Additionally, there is support for the OPAL Type 2 (Iglesias & Rogers 1996) tables that allow for varying amounts of C and O beyond that accounted for by  $Z$ ; these are needed during helium burning and beyond. These have a range  $0.0 \leq X \leq 0.7$  and  $0.0 \leq Z \leq 0.1$ .

The resulting kap tables cover the large range  $2.7 \leq \log T \leq 10.3$  and  $-8 \leq \log R \leq 8$  ( $R = \rho/T_6^3$ , so  $\log R = \log \rho - 3 \log T + 18$ ), as shown by the heavy orange and black lines in Figure 2. The MESA release includes MESA opacity tables derived from Type 1 and 2 OPAL tables, tables from OP, and Ferguson et al. (2005). The heavy orange lines delineate the boundaries where we use existing tables to make the MESA opacity table.

<sup>16</sup> <http://freeeos.sourceforge.net>

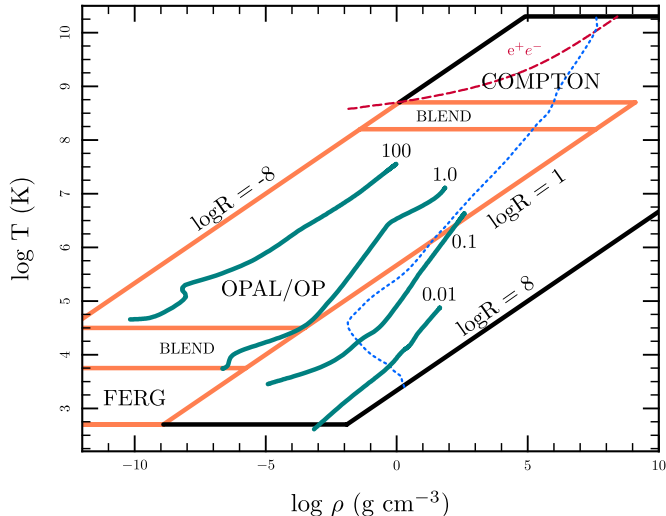


**Figure 2.** Sources of the standard MESA opacity tables. Construction of opacity tables requires incorporating different sources, denoted by the labels. The heavy orange lines denote regions where input tables exist for radiative opacities, whereas the heavy black lines extend into regions where we use algorithms to derive the total opacities, described in the text. Above the dashed red line, the number of electrons and positrons from pair production exceeds the number of electrons from ionization, and is accounted for in the opacity table. The opacity in the region to the right of the dashed blue line is dominated by electron conduction. Also shown are stellar profiles for stars on main sequence ( $M = 0.1, 1.0$ , and  $100 M_{\odot}$ ) or just below (a contracting  $M = 0.01 M_{\odot}$  brown dwarf).

(A color version of this figure is available in the online journal.)

The blended regions in Figure 2 are where two distinct sources of radiative opacities exist for the same parameters, requiring a smoothing function that blends them in a manner adequate for derivatives. The blend is calculated at a fixed  $\log R$  by defining the upper ( $\log T_U$ ) and lower ( $\log T_L$ ) boundaries of the blending region in  $\log T$  space, where  $\kappa_U$  ( $\kappa_L$ ) is the opacity source above (below) the blend. We perform the interpolation by defining  $F = (\log T - \log T_L)/(\log T_U - \log T_L)$ , and using a smooth function  $S = (1 - \cos(F\pi))/2$  for

$$\log \kappa = S \log \kappa_U(R, T) + (1 - S) \log \kappa_L(R, T). \quad (1)$$

At high temperatures, the blend from Compton to OPAL (or OP) has  $\log T_U = 8.7$  and  $\log T_L = 8.2$ . At low temperatures, the blend between Ferguson et al. (2005) and OPAL has  $\log T_U = 4.5$  and  $\log T_L = 3.75$ .

The absence of tabulated radiative opacities for  $\log R > 1$  and  $\log T < 8.2$  (the region below the heavy dashed line in Figure 2) leads us to use the radiative opacity at  $\log R = 1$  (for a specific  $\log T$ ) when combining with the electron conduction opacities. This introduces errors in the MESA opacity table between  $\log R = 1$  and the region to the right of the dashed blue line in Figure 2 where conductive opacities become dominant. However, as we show in Figure 3, main-sequence stars are always efficiently convective in this region of parameter space, alleviating the issue.

The module `kap` gives the user the resulting opacities by interpolating in  $\log T$  and  $\log R$  with bicubic splines from `interp_2d`. The user has the option of either linear or cubic interpolation in  $X$  and  $Z$  and can specify whether to use the fixed metal (Type 1) tables or the varying C and O (Type 2) tables. In the latter case, the user must specify the reference C and O in the initial composition.

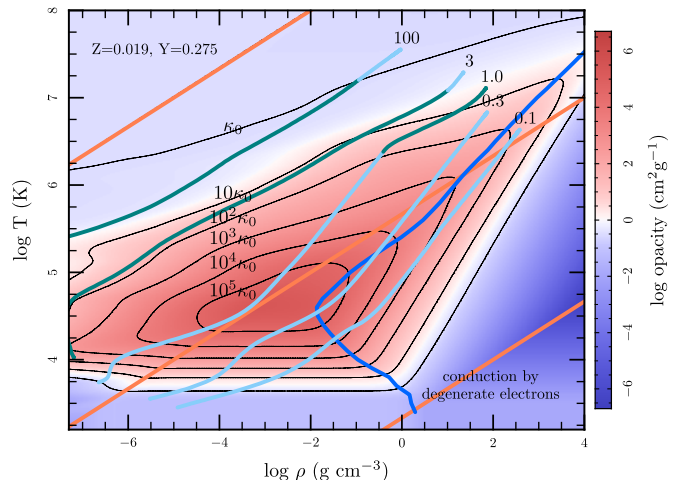


**Figure 3.** Resulting MESA opacities for  $Z = 0.019$ ,  $Y = 0.275$ . The underlying shades show the value of  $\kappa$ , whereas the contours are in units of the electron scattering opacity,  $\kappa_0 = 0.2(1 + X) \text{ cm}^2 \text{ g}^{-1}$ . The orange lines show (top to bottom) where  $\log R = -8$ ,  $\log R = 1$ , and  $\log R = 8$ . Stellar interior profiles for main sequence stars of mass  $M = 0.1, 0.3, 1.0, 3.0$ , and  $100 M_{\odot}$  are shown by the green (radiative regions)-light blue (convective regions) lines. Electron conduction dominates the opacity to the right of the dark blue line (which is where the radiative opacity equals the conductive opacity).

(A color version of this figure is available in the online journal.)

For requests outside the  $\log T$  and  $\log R$  boundaries, the following is done. The region to the left of  $\log R = -8$  and below  $\log T = 8.7$  is electron scattering dominated, so the cross-section per electron is density independent. However, the increasing importance of the Compton effect as the temperature increases (which is incorporated in the OPAL/OP tabulated opacities) must be included, so we use the opacity from the table at  $\log R = -8$  at the appropriate value of  $\log T$ . For higher temperatures ( $\log T > 8.7$ ) electron–positron pairs become prevalent, as exhibited by the red dashed line that shows where the number of positrons and electrons from pair production exceeds the number of electrons from ionization. MESA incorporates the enhancement to the opacity from these increasing numbers of leptons per baryon.

At the end of a star’s life, low enough entropies can be reached that an opacity for  $\log R > 8$  is needed. When `kap` is called in this region, we simply use the value at  $\log R = 8$  for the same  $\log T$ . For regions where  $Z > 0.1$ , the table at  $Z = 0.1$  is used.

The resulting opacities for  $Z = 0.019$  and  $Y = 0.275$  are shown in Figure 3, both as a color code, and as contours relative to the electron scattering opacity,  $\kappa_0 = 0.2(1 + X) \text{ cm}^2 \text{ g}^{-1}$ . The orange lines show (top to bottom) where  $\log R = -8$ ,  $\log R = 1$  and  $\log R = 8$ . We show a few stellar profiles for main-sequence stars as marked. The green parts of the line are where heat transfer is dominated by heat transport, requiring an opacity, whereas the light blue parts of the line are where the model is convective. As is evident, nearly all of the stellar cases of interest (shown by the green-blue lines) are safely within the boundaries of the MESA tables. The lack of radiative opacities in the higher density region to the right of  $\log R = 1$  implies opacity uncertainties until the dark blue line is reached (where the conductive opacity takes over). However, the stellar models are convectively efficient in this region, so that the poor value for  $\kappa$  does not impact the result as long as the convective zone’s existence is independent of the opacity (the typical case for these stars, where the ionization zone causes the convection).

It is also possible to generate a new set of `kap` readable opacity tables using the `make_kap` pre-processor. The requirements

are high-temperature radiative opacities in the standard OPAL format and low-temperature radiative opacities in the number and format provided by Ferguson et al. (2005).<sup>17</sup> Specific high-temperature radiative opacities can be made by using the OPAL site<sup>18</sup> or the Opacity Project site.<sup>19</sup>

Since not all opacity sources can be placed in the tabular form desired by `kap`, we have created a module, `other_kap`, that provides the user an opportunity to incorporate their own opacity source. A simple flag tells `MESA star` to call `other_kap` rather than `kap`, allowing for experiments with new opacity schemes and physics updates. The first example of such an implementation that has now become a `MESA` module is `karo`. It was developed to study the stellar evolution effects of dust-driven winds in carbon-rich stars, using the Rosseland opacities of Lederer & Aringer (2009) and the hydro-dynamical wind models of Mattsson et al. (2010).

#### 4.4. Thermonuclear and Weak Reactions

The `rates` module contains thermonuclear reaction rates from Caughlan & Fowler (1988, CF88) and Angulo et al. (1999, NACRE), with preference given to the NACRE rate when available. The reaction rate library includes more than 300 rates for elements up to nickel, and includes the weak reactions needed for hydrogen burning (e.g., positron emissions, electron captures), as well as neutron–proton conversions and a few other electron and neutron capture reactions. Significant updates to the NACRE rates have been included for  $^{14}\text{N}(p,\gamma)^{15}\text{O}$  (Imbriani et al. 2004), triple- $\alpha$  (Fynbo et al. 2005),  $^{14}\text{N}(\alpha,\gamma)^{18}\text{F}$  (Görres et al. 2000), and  $^{12}\text{C}(\alpha,\gamma)^{16}\text{O}$  (Kunz et al. 2002). In these special cases, the rate can be selected from CF88, NACRE, or the newer reference by the user at run time.

The `weaklib` module calculates lepton captures and  $\beta$ -decay rates for the high densities and temperatures encountered in late stages of stellar evolution. The rates are based on the tabulations of Fuller et al. (1985), Oda et al. (1994), and Langanke & Martínez-Pinedo (2000) for isotopes with  $45 < A < 65$ . The most recent tabulations of Langanke & Martínez-Pinedo (2000) take precedence, followed by Oda et al. (1994), then Fuller et al. (1985). The user can override this to create tables using any combination of these or other sources.

The `screen` module calculates electron screening factors for thermonuclear reactions in both the weak and strong regimes. The treatment has two options. One is based on Dewitt et al. (1973) and Grabske et al. (1973). The other<sup>20</sup> combines Grabske et al. (1973) in the weak regime and Alastuey & Jancovici (1978) with plasma parameters from Itoh et al. (1979) in the strong regime.

The `neu` module calculates energy-loss rates and their derivatives from neutrinos generated by a range of processes including plasmon decay, pair annihilation, bremsstrahlung, recombination, and photo-neutrinos (i.e., neutrino pair production in Compton scattering). It is based on the publicly available routine (see footnote 20, derived from the fitting formulae of Itoh et al. 1996).

#### 4.5. Nuclear Reaction Networks

The `net` module implements nuclear reaction networks and is derived from publicly available code<sup>20</sup>. It includes a “basic”

network of eight isotopes:  $^1\text{H}$ ,  $^3\text{He}$ ,  $^4\text{He}$ ,  $^{12}\text{C}$ ,  $^{14}\text{N}$ ,  $^{16}\text{O}$ ,  $^{20}\text{Ne}$ , and  $^{24}\text{Mg}$ , and extended networks for more detailed calculations including coverage of hot CNO reactions,  $\alpha$ -capture chains,  $(\alpha,p)+(p,\gamma)$  reactions, and heavy-ion reactions (Timmes 1999). In addition to using existing networks, the user can create a new network by listing the desired isotopes and reactions in a data file that is read at run time. The amount of heat deposited in the plasma by reactions is derived from the nuclear masses in `chem`, taken from the JINA Reaclib database (Rauscher & Thielemann 2000; Sakharuk et al. 2006; Cyburt et al. 2010), and accounts for positron annihilations and energy lost to weak neutrinos, using Bahcall (1997, 2002) for the hydrogen burning reactions. The list of approximately 350 reactions is stored in a data file that catalogs the reaction name, the input and output species, and their heat release.

The `jina` module is an alternative nuclear network module that specializes in large networks. It is based on the “netjina” package by Ed Brown and uses the JINA Reaclib database for thermonuclear reaction rates (Rauscher & Thielemann 2000; Sakharuk et al. 2006),<sup>21</sup> the `rates` and `weaklib` modules for weak interactions, and `screen` for electron screening. Most importantly, it allows the user to create large nuclear networks by specifying the list of isotopes to consider. All nuclear reactions (both strong and weak) linking the isotopes in the set are automatically included in the network. In all, `jina` covers more than 76,000 nuclear reactions involving more than 4500 isotopes. The `jina` module is slower than `net` for small networks but the flexibility and capacity to handle large networks make it advantageous in some cases.

Both `net` and `jina` include one-zone burn routines that operate on a user-defined initial composition, nuclear network, and a trajectory comprising density and temperature as a function of time. The one-zone burn routines interface with `mtx` and `num`, enabling the use of the sparse matrix solver, which substantially improves performance compared to the dense matrix solver for networks of more than a few hundred isotopes. Figures 4 and 5 demonstrate these one-zone routines operating on conditions appropriate for the Sun on the main sequence and for a core He-burning star, respectively. Both examples were evolved at fixed density and temperature for 10 Gyr. Each figure compares three networks of varying size in terms of the mass fractions and net energy generation per unit mass,  $e_{\text{nuc}}$  ( $\text{erg g}^{-1}$ ), produced. Tables 4 and 5 complement Figures 4 and 5, respectively, by listing the final values from each of the one-zone burn simulations. These comparisons indicate that the eight isotope network produces results that agree with larger networks to 4–5 significant figures in net energy generation per unit mass and generally 2–3 significant figures in the mass fractions of various isotopes. Hence, the eight isotope network is sufficiently accurate to describe the energy generation for hydrogen and helium burning.

## 5. MACROPHYSICS

### 5.1. The Mixing Length Theory of Convection

The `mlt` module implements the standard mixing length theory (MLT) of convection as presented by Cox & Giuli (1968, chap. 14). There are options both for computing the actual temperature gradient,  $\nabla_T$ , when the total luminosity,  $L$ , is specified and for computing the convective luminosity,  $L_{\text{conv}}$ , when  $\nabla_T$  is specified. The `mlt` module calculates diffusion

<sup>17</sup> <http://webs.wichita.edu/physics-opacity>

<sup>18</sup> <http://opalopacity.llnl.gov/new.html>

<sup>19</sup> <http://cdsweb.u-strasbg.fr/topbase/op.html>

<sup>20</sup> [http://cococabed.asu.edu/code\\_pages/codes.shtml](http://cococabed.asu.edu/code_pages/codes.shtml)

<sup>21</sup> <http://groups.nscl.msu.edu/jina/reaclib/db/index.php>

**Table 4**  
Comparison of One-zone Solar Burn Results at 10 Gyr

Network	$\log_{10} e_{\text{nuc}}$	$\log_{10} X(^1\text{H})$	$\log_{10} X(^4\text{He})$	$\log_{10} X(^{12}\text{C})$	$\log_{10} X(^{14}\text{N})$	$\log_{10} X(^{16}\text{O})$
jina 25	18.63757961	-3.87550319	-0.008144854	-4.40235799	-1.9195882	-3.07400339
net 25	18.63685339	-3.87550517	-0.008145036	-4.40235799	-1.9195882	-3.07400333
net 8	18.63675658	-3.93650004	-0.008137607	-4.39650625	-1.9135911	-3.04585377

**Table 5**  
Comparison of One-zone He-burn Results at 10 Gyr

Network	$\log_{10} e_{\text{nuc}}$	$\log_{10} X(^{12}\text{C})$	$\log_{10} X(^{16}\text{O})$	$\log_{10} X(^{22}\text{Ne})$	$\log_{10} X(^{26}\text{Mg})$
jina 200	17.9085633	-0.721578469	-0.108630252	-1.50380756	-4.01520633
net 11	17.9086380	-0.721576540	-0.108630957	-1.50385214	-3.99780015
net 8	17.9083877	-0.718866029	-0.107692784	...	...

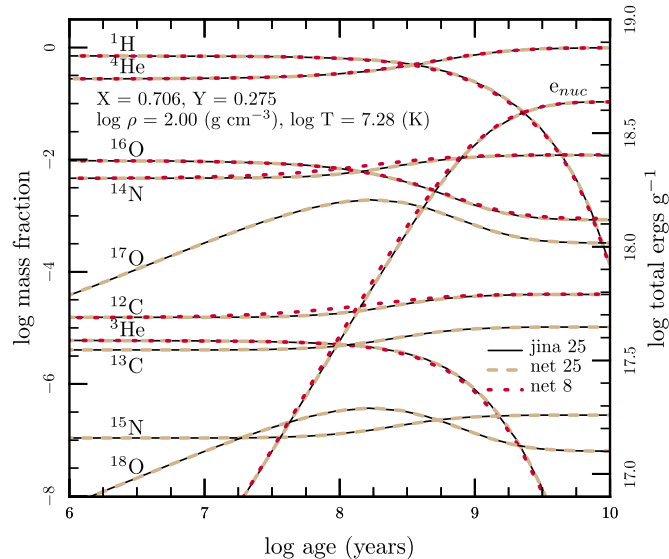


**Figure 4.** One-zone hydrogen burn at constant  $T = 19 \times 10^6$  K and  $\rho = 100$  g cm $^{-3}$  by three different networks. The number following net or jina indicates the number of isotopes considered in that network. The 25 isotope networks expand on the eight isotope network by including minor contributors to the pp and CNO cycles. The plot shows the evolution of the mass fraction abundances of the ten most abundant isotopes and net energy generation per unit mass,  $e_{\text{nuc}}$  (erg g $^{-1}$ ), as a function of time. The left-hand axis shows the mass fraction, while the right-hand axis shows the net energy generation per unit mass.

(A color version of this figure is available in the online journal.)

coefficients for those codes, such as MESA star, that treat convective mixing of elements as a diffusive process. The quantities listed in Table 6 and their partial derivatives with respect to several physical variables are returned by the mlt module.

In addition to the standard MLT of Cox and Giuli, the mlt module includes the option to use the modified MLT of Henyey et al. (1965). Whereas the standard MLT assumes high optical depths and no radiative losses, the Henyey et al. (1965) variation allows the convective efficiency to vary with the opaqueness of the convective element, an important effect for convective zones near the outer layers of stars. If the Henyey et al. (1965) option is used, the parameters  $v$  (a mixing length velocity multiplier) and  $y$  (a parameter that sets the temperature gradient in a rising bubble) may be set by the user. They default to the recommended values of  $y = 1/3$  and  $v = 8$ .

Toward the center of a star, the commonly used definition of the pressure scale height,  $\lambda_P = P/g\rho$ , diverges as  $g \rightarrow 0$ .

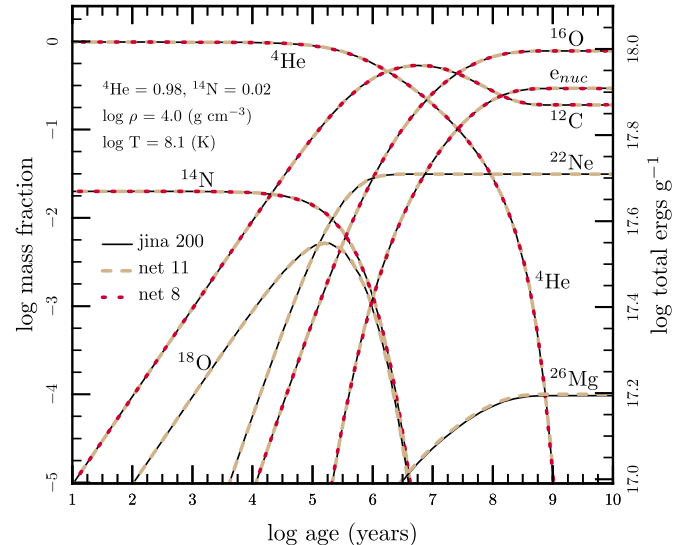


**Figure 5.** Equivalent to Figure 4 but now showing a one-zone helium burn at constant  $\log T = 8.1$  and  $\log \rho = 4.0$ . The “net 11” network adds  $^{18}\text{O}$ ,  $^{22}\text{Ne}$ , and  $^{26}\text{Mg}$  to the eight isotope network; “jina 200” includes about 200 isotopes up to  $^{71}\text{Ge}$ .

(A color version of this figure is available in the online journal.)

**Table 6**  
MESA mlt Output Quantities and Units

Output	Definition	Units
$\nabla_T$	Actual temperature gradient <sup>a</sup>	Dimensionless
$\nabla_{\text{rad}}$	Radiative temperature gradient <sup>a</sup>	Dimensionless
$L_{\text{conv}}$	Convective luminosity <sup>b</sup>	erg s $^{-1}$
$L$	Total luminosity <sup>c</sup>	erg s $^{-1}$
$\lambda_P$	Pressure scale height	cm
$\Lambda$	Mixing length ( $\equiv \alpha_{\text{MLT}} \lambda_P$ )	cm
$v_{\text{conv}}$	Convective velocity	cm s $^{-1}$
$D$	Eulerian diffusion coefficient	cm $^2$ s $^{-1}$
$\sigma$	Lagrangian diffusion coefficient ( $\equiv D(4\pi r^2 \rho)^2$ )	g $^2$ s $^{-1}$

#### Notes.

<sup>a</sup> Only when  $L$  is specified.

<sup>b</sup> Only when  $\nabla_T$  is specified.

<sup>c</sup> Only when  $\nabla_T$  is specified and  $L_{\text{conv}} > 0$ .

Therefore, we provide the option of using the alternate definition of Eggleton (1971),  $\lambda'_P = (P/G\rho^2)^{1/2}$ , when  $\lambda'_P < \lambda_P$ . At the center of the star,  $\lambda'_P \sim R$ .

The dependence of mixing instabilities on composition gradients (e.g., semiconvection and thermohaline mixing) are

presently not taken into account by the `mlt` module. To include this capability is a high priority for the MESA project.

### 5.2. Convective Overshoot Mixing

As described in Section 6.2, MESA star treats convective mixing as a time-dependent, diffusive process with a diffusion coefficient,  $D$ , determined by the `mlt` module. In the absence of a three-dimensional hydrodynamical treatment of convection it is necessary to account for the hydrodynamical mixing instabilities at convective boundaries, termed overshoot mixing, via a parametric model. After the MLT calculations have been performed, MESA star sets the overshoot mixing diffusion coefficient

$$D_{\text{OV}} = D_{\text{conv},0} \exp\left(-\frac{2z}{f\lambda_{P,0}}\right), \quad (2)$$

where  $D_{\text{conv},0}$  is the MLT derived diffusion coefficient at a user-defined location near the Schwarzschild boundary,  $\lambda_{P,0}$  is the pressure scale height at that location,  $z$  is the distance in the radiative layer away from that location, and  $f$  is an adjustable parameter (Herwig 2000). In MESA star the adjustable parameter,  $f$ , may have different values at the upper and lower convective boundaries for non-burning, H-burning, He-burning, and metal-burning convection zones.

Parameters are provided to allow the user to set a lower limit on  $D_{\text{OV}}$  below which overshoot mixing is neglected and to limit the region of the star over which overshoot mixing will be considered. So as to model the  $^{13}\text{C}$  pocket needed for  $s$ -process nucleosynthesis, MESA star also allows an increase in the overshooting parameter at the bottom of the convective envelope during the third dredge-up compared to the inter-pulse value (Lugardo et al. 2003). There is also an option to change the value of overshoot mixing at the bottom of the asymptotic giant branch (AGB) thermal pulse-driven convection zone compared to the standard value chosen for the bottom of the He-burning convection zone.

### 5.3. Atmosphere Boundary Conditions

As described in Section 6.2, the pressure,  $P_s$ , and temperature,  $T_s$ , at the top of the outermost cell in MESA star must be set by an atmospheric model. This is done by the `atm` module, which uses  $M$ ,  $R$ , and  $L$  to provide  $P_s$  and  $T_s$ . It also gives partial derivatives of  $T_s$  and  $P_s$  with respect to the input variables. The `atm` module assumes the plane parallel limit, so that the relevant variables are  $g = GM/R^2$  and  $T_{\text{eff}}^4 = L/4\pi\sigma_{\text{SB}}R^2$ . With some options, the user must specify the optical depth  $\tau_s$  to the base of the atmosphere, whereas in other cases, the `atm` module has an implicit value. Three methods are supplied by `atm`: direct integrations, interpolations in model atmosphere tables, and a “simple” recipe.

The integrations of the hydrostatic balance equation,  $dP_{\text{gas}}/d\tau = g/\kappa - (a/3)dT^4/d\tau$ , with  $d\tau = -\kappa\rho dr$  are performed using either the relation  $T^4(\tau) = 3T_{\text{eff}}^4(\tau + 2/3)/4$  (Eddington 1926), or the specific  $T-\tau$  relation of Krishna Swamy (1966). These integrations start at  $\tau = 10^{-5}$  and end at a user specified stopping point,  $\tau_s$ , which defaults to  $\tau_s = 2/3$  (0.312) for Eddington (Krishna Swamy).<sup>22</sup> The routine integrates the gas pressure and then adds the radiation pressure at the stopping point to get  $P_s$ .

<sup>22</sup> If the first attempt to integrate fails, the code makes two further attempts, each time increasing the initial  $\tau$  by a factor of 10. The integration is carried out with the Dormand–Price integrator from the `num` module.

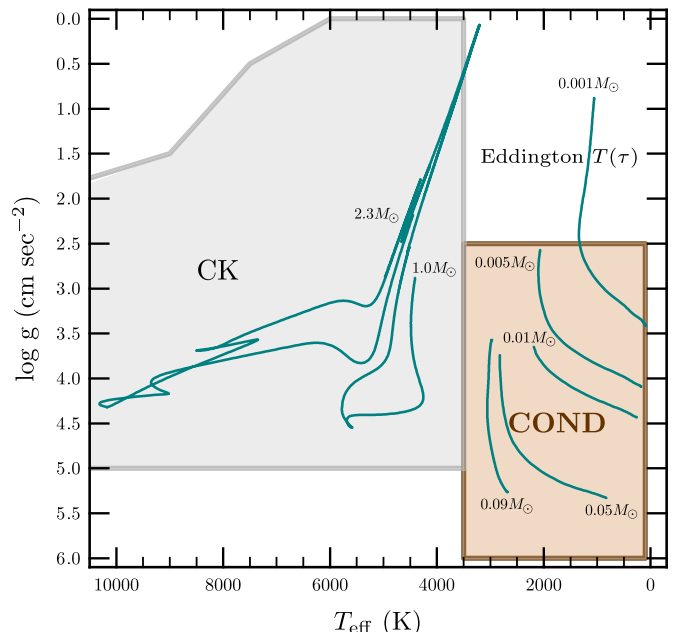


**Figure 6.** Range of  $T_{\text{eff}}$  and  $\log(g)$  covered by the MESA `atm` tables for  $\tau_s = 100$  and solar metallicity. The CK region uses the tables of Castelli & Kurucz (2003), whereas the COND region uses Allard et al. (2001). At lower  $\log(g)$  and cold regions, we use direct integrations of the Eddington  $T-\tau$  relation. The green lines show evolutionary tracks of stars, brown dwarfs and giant planets of the noted masses.

(A color version of this figure is available in the online journal.)

The MESA model atmosphere tables come in two forms. The MESA photospheric tables (which return  $T_s \equiv T_{\text{eff}}$  and assume that  $\tau_s \approx 1$ ) cover  $\log Z/Z_{\odot} = -4$  to  $+0.5$  assuming the Grevesse & Noels (1993) Solar abundance mixture. They span  $\log(g) = -0.5$  to  $5.5$  at  $0.5$  dex intervals and  $T_{\text{eff}} = 2000$ – $50,000$  K at  $250$  K intervals. They are constructed, in precedence order, with, first, the PHOENIX (Hauschildt et al. 1999a, 1999b) model atmospheres (which span  $\log(g) = -0.5$  to  $5.5$  and  $T_{\text{eff}} = 2000$  to  $10,000$  K); and second, the Castelli & Kurucz (2003) model atmospheres (which span  $\log(g) = 0$ – $5$  and  $T_{\text{eff}} = 3500$ – $50,000$  K). In regions where neither table is available, we generate the MESA table entry using the integrations described above with the Eddington  $T-\tau$  relation. The second MESA table is for solar metallicity and gives  $P_s$  and  $T_s$  at  $\tau_s = 100$ . It is primarily for the evolution of low-mass stars, brown dwarfs, and giant planets. It is constructed from Castelli & Kurucz (2003) and, for  $T_{\text{eff}} < 3000$  K, the COND model atmospheres (Allard et al. 2001) which assume gravitational settling of those elements that form dust, depleting those elements from the photosphere. Figure 6 shows the regions where the different sources are used, and in those regions where there are no published results, we use the integration of the Eddington  $T-\tau$  relation.

Finally, there is a simple option where the user specifies  $\tau_s$  and we use the constant opacity,  $\kappa_s$ , solution of radiative diffusion,

$$P_s = \frac{\tau_s g}{\kappa_s} \left[ 1 + 1.6 \times 10^{-4} \kappa_s \left( \frac{L/L_{\odot}}{M/M_{\odot}} \right) \right], \quad (3)$$

where the factor in square brackets accounts for the nonzero radiation pressure (see, e.g., Cox & Giuli 1968, Section 20.1). The temperature is simply given by the Eddington relation. The user can either specify  $\kappa_s$  or it will be calculated in an iterative manner using the initial value of  $P_s$  from an initial guess at  $\kappa_s$ .

(usually given by MESA star as the value in the outermost cell; see Section 6.2). In addition, the atm module has the option to revert to Equation (3) if a model wanders outside the range of the currently used model atmosphere tables or if the atmosphere integration fails for any reason.

#### 5.4. Diffusion and Gravitational Settling

MESA diffusion calculates particle diffusion and gravitational settling by solving Burger's equations using the method and diffusion coefficients of Thoul et al. (1994). The transport of material is computed using the semi-implicit, finite difference scheme described by Iben & MacDonald (1985). Radiative levitation is not presently included. The diffusion module treats the elements present in the stellar model as belonging to “classes” defined by the user in terms of ranges of atomic masses. For each class, the user specifies a representative isotope, and all members of that class are treated identically with their diffusion velocities determined by the representative isotope, and the diffusion equation solved with the mass fraction in that class. The caller can either specify the ionic charge for each class at each cell in the model or has the charge calculated by the ionization module, which estimates the typical ionic charge as a function of  $T$ ,  $\rho$ , and free electrons per nucleon from Paquette et al. (1986).

The lines in Figure 7 plot four classes (H, He, O, and Fe) with a solar model from MESA star and compares where possible to the results from Figure 9 of Thoul et al. (1994), shown by the filled green circles. The agreement is excellent for H, O, and Fe (when we fix Fe to have the  $Z = 21$  ionization state chosen by Thoul et al. 1994). Thoul et al. (1994) did not exhibit the He velocity, so we have no comparison. For Fe, we also show the diffusion velocity when ionization finds a changing ionization state in the  $Z = 16, 17, 18$  region (shown by the upper dot-dashed blue line), highlighting the need to better determine the Fe ionization state (Gorshkov & Baturin 2008). We also compared the diffusion output to the recent calculations of Gorshkov & Baturin (2008), finding agreement at better than 5% for the Fe case at  $Z = 26$  and for O.

The diffusion calculation can be restricted to areas where the temperature is above some minimum value, or where the mass fraction of a diffusing element is above some minimum value, aiding the convergence of solutions in a variety of environments. The physics implementation is presently limited to regions where the Coulomb coupling parameter,  $\Gamma$ , is less than unity. At present, this inhibits an accurate calculation for segregation and settling of the remaining envelope H and He envelope on a cooling white dwarf.

#### 5.5. Testing MESA Modules in an Existing Stellar Evolution Code

The complex, nonlinear behavior of stellar structure and evolution models makes it difficult to disentangle the effects of model components (e.g., EOS, opacities, boundary conditions, etc.) when comparing results of separate codes. By design, the modularity of MESA allows individual physics modules to be incorporated into an existing stellar evolution code, tested, and then compared against the prior implementation of comparable physics in the same code.

During the development of MESA, several MESA modules were integrated into the Dartmouth Stellar Evolution Program (DSEP; Dotter et al. 2007). This section reports the results of using four MESA modules, eos, kap, atm, and mlt, in DSEP to compute

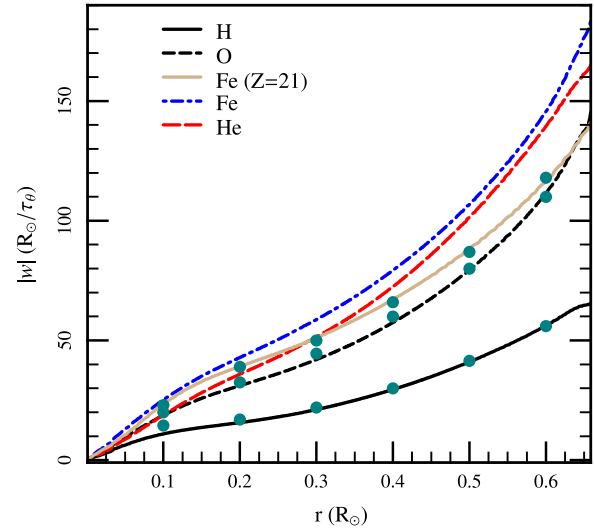


**Figure 7.** Absolute values of the diffusion velocities from diffusion (lines) and those published by Thoul et al. (1994). All results are plotted in units of  $R_\odot/\tau_\theta$ , where  $\tau_\theta = 6 \times 10^{13}$  yr is the characteristic diffusion timescale for the Sun (Thoul et al. 1994). The dark solid and dashed lines are the diffusion results for H and O. The filled green circles show the results of Thoul et al. (1994) for H, O, and Fe ( $Z = 21$ ). The diffusion results for helium are shown as the dashed red line. The diffusion results for Fe include one for  $Z = 21$  (dotted blue line) and one for ionization states determined by ionization (the dot-dashed blue line).

(A color version of this figure is available in the online journal.)

the evolution of a  $1.0 M_\odot$  star with initial values of  $X = 0.70$  and  $Z = 0.02$ . The star was evolved from the fully convective pre-main sequence (PMS) to the onset of the core He flash. This was done six times: once, as the control case, using only DSEP routines and no MESA modules; next, using each of four MESA modules individually; and, finally, using the four MESA modules at the same time in DSEP.

DSEP employs a  $\rho(P, T)$  EOS and so the MESA  $P_{\text{gas}}-T$  tables were used during the eos test. Though DSEP and kap use the same sources for radiative opacities, they differ in interpolation methods and the treatment of electron conduction opacities (see Bjork & Chaboyer 2006, for a thorough list of the physics in DSEP). When atm was tested, we used the Eddington gray atmosphere model integrated to  $\tau = 2/3$ . DSEP uses the Henyey et al. (1965) modification of the MLT, which is available in mlt, and assumes that convective regions are instantaneously mixed to a uniform composition.

DSEP tracks employing either the atm or the mlt modules produce results that agree with the DSEP-only track to about one part in  $10^4$ . DSEP tracks employing the kap and eos modules exhibit some difference when compared to the DSEP-only track but, even in these cases, the main-sequence lifetime differs by less than 0.3% and  $T_{\text{eff}}$  differs by less than 10 K along the main sequence. As shown in Figure 8, the largest discrepancy between the DSEP-only track and the one that employs all four MESA modules appears in the  $T_c-\rho_c$  diagram when  $\rho_c > 3 \times 10^4$  g cm $^{-3}$ , corresponding to the growing helium core in the center of the red giant. Above  $\log \rho_c = 4$ , the track employing MESA modules is hotter than the DSEP-only track by  $\sim 0.02$  in  $\log T_c$  at constant  $\log \rho_c$ . The center of the model has entered the region of electron degeneracy and electron conduction has become an important source of opacity. The majority of the difference is due to the EOS whereas the opacity difference amounts to about  $-0.005$  in  $\log T_c$ , in the opposite direction to the EOS. The hotter conditions produced

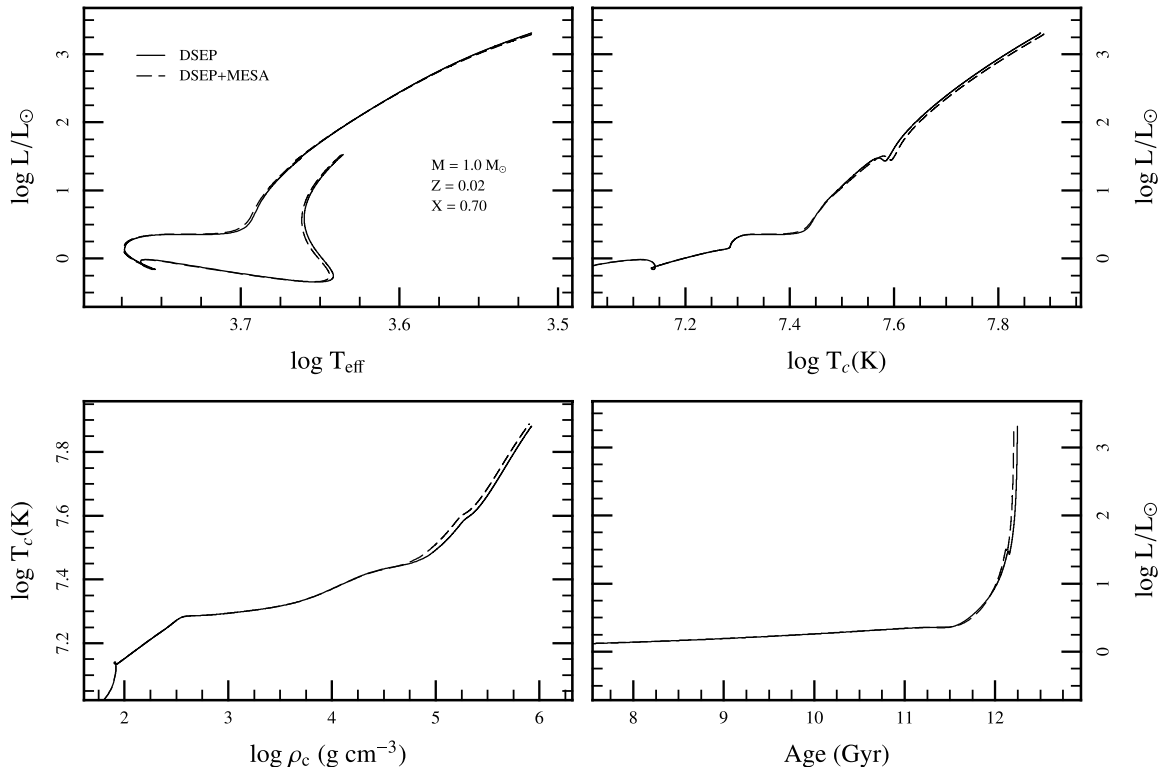


**Figure 8.** Comparison of DSEP tracks using built-in physics modules and MESA modules for opacities, EOS, MLT, and the atmospheric boundary condition. These tracks are for a  $1.0 M_{\odot}$  star with initial  $X = 0.70$  and  $Z = 0.02$  evolved from the fully convective PMS to the onset of the He core flash. Only the H-R diagram shows the full evolutionary track. The  $T_c$  panels omit the PMS in order to highlight the regions where the differences are most pronounced; the lifetime panel focuses on the end of the main sequence and red giant phase for the same reason.

by the eos module are likely the cause for the slightly shorter red giant branch (RGB) lifetime that can be seen in Figure 8.

## 6. STELLAR STRUCTURE AND EVOLUTION

MESA star is a full-featured stellar structure and evolution library that utilizes the numerics and physics modules described in Sections 3–5. It provides a clean-sheet implementation of a Henyey style code (Henyey et al. 1959) with automatic mesh refinement, analytic Jacobians, and coupled solution of the structure and composition equations. The design and implementation of MESA star were influenced by a number stellar evolution and hydrodynamic codes that were made available to us: EV (Eggleton 1971), EVOL (Herwig 2004), EZ (Paxton 2004), FLASH-the-tortoise (Lesaffre et al. 2006), GARSTEC (Weiss & Schlattl 2008), NOVA (Starrfield et al. 2000), TITAN (Gehmeyr & Mihalas 1994), and TYCHO (Young & Arnett 2005).

We now briefly describe the primary components of MESA star. MESA star first reads the input files and initializes the physics modules (see Section 6.1) to create a nuclear reaction network and access the EOS and opacity data. The specified starting model or PMS model is then loaded into memory (see Section 6.1), and the evolution loop is entered. The procedure for one timestep has four basic elements. First, it prepares to take a new timestep by remeshing the model if necessary (Sections 6.4 and 6.5). Second, it adjusts the model to reflect mass loss by winds or mass gain from accretion (Section 6.6), adjusts abundances for element diffusion (Section 5.4), determines the convective diffusion coefficients (Sections 5.1 and 5.2), and solves for the new structure and composition (Sections 6.2 and 6.3) using the Newton–Raphson solver (Section 3). Third, the next timestep

is estimated (Section 6.4). Fourth, output files are generated (Section 6.1).

### 6.1. Starting Models and Basic Input/Output

MESA star receives basic input from two Fortran namelist files. One file specifies the type of evolutionary calculation to be performed, the type of input model to use, the source of EOS and opacity data, the chemical composition and nuclear network, and other properties of the input model. The second file specifies the controls and options to be applied during the evolution.

There are two ways to start a new evolutionary sequence with MESA star. The first is to use a saved model from a previous run. A variety of saved models are distributed with MESA as a convenience. These saved models fall into three general categories: (1) zero age main sequence (ZAMS) models for  $Z = 0.02$  with 32 masses between  $0.08$  and  $100 M_{\odot}$  (MESA star will automatically interpolate any mass within this range); (2) very low mass, PMS models for  $Z = 0.02$  and masses from  $0.001$  to  $0.025 M_{\odot}$ ; and (3) white dwarf models for  $Z = 0.02$  with He cores of  $0.15$ – $0.45 M_{\odot}$ , C/O cores of  $0.496$ – $1.025 M_{\odot}$ , and O/Ne cores of  $1.259$ – $1.376 M_{\odot}$ . The user can also create saved models for essentially any purpose through available controls.

The second way to start a new evolution is to create a PMS model by specifying the mass,  $M$ , a uniform composition, a luminosity, and a central temperature,  $T_c$  low enough that nuclear burning is inconsequential ( $T_c = 9 \times 10^5$  K by default). For a fixed  $T_c$  and composition, the total mass depends only on the central density,  $\rho_c$ . An initial guess for  $\rho_c$  is made by using the  $n = 1.5$  polytrope, which is appropriate for a fully convective star, but we do not assume that the star is fully

convective during the subsequent search for a converged PMS model. Instead, MESA star uses the `mlt`, `eos`, and Newton solver from `num` to search for a  $\rho_c$  that gives a model of the desired mass. The PMS routine presently creates starting models for  $0.02 \leq M/M_\odot \leq 50$ . Beyond these limits we find challenges converging the generated PMS model within the MESA star evolutionary loop. For such cases, it is currently better to generate a starting model within the acceptable mass range, save it, relax it to a new mass with a specified mass gain or loss (see Section 6.6), and save that model.

MESA star has the ability to create a binary file of its complete current state, called a photo, at user-specified timestep intervals. Restarting from a photo ensures no differences in the ensuing evolution. When restarting from a photo, many controls and options can be changed. A photo is different than a saved model in that a saved model is a text file containing a minimal description of the structure and composition but does not have enough information to allow a perfect restart. However, saved models are not tied to a particular version of the code and therefore are suitable for long-term use or sharing with other users.

There are two additional types of output files, logs and profiles. A log records evolutionary properties over time such as stellar age, current mass, and a wide array of other quantities. A profile records model properties at a specified timestep at each zone from surface to center. MESA star can also output models in the FGONG format<sup>23</sup> for use with stellar pulsation codes and `se` output for nucleosynthesis post-processing with NuGrid codes.<sup>24</sup> Finally, a few simple lines of user-supplied code allows for saving variables or combinations of variables that are not in the list of predefined options.

## 6.2. Structure and Composition Equations

MESA star builds one-dimensional, spherically symmetric models by dividing the structure into cells, anywhere from hundreds to thousands depending on the complexity of nuclear burning, gradients of state variables, composition, and various tolerances. Cells are numbered starting with one at the surface and increasing inward. MESA star does not require the structure equations to be solved separately from the composition equations (operator splitting). Instead, it simultaneously solves the full set of coupled equations for all cells from the surface to the center. The solution of the equations is done by the Newton solver from `num` using either banded or sparse matrix routines from `mtx`. The partial derivatives for use by the solver are calculated analytically using the partials returned by modules such as `eos`, `kap`, and `net`.

Each cell has some variables that are mass-averaged and others that are defined at the outer face, as shown in Figure 9. This way of defining the variables is a consequence of the finite volume, flux conservation formulation of the equations, and improves stability and efficiency (Sugimoto et al. 1981). The inner boundary of the innermost cell is usually the center of the star and, therefore, has radius, luminosity, and velocity equal to zero. Nonzero center values can be used for applications that remove the underlying star (e.g., the envelope of a neutron star), in which case the user must define the values of  $M_c$  and  $L_c$  at the inner radius  $R_c$ . The cell mass-averaged variables are density  $\rho_k$ , temperature  $T_k$ , and mass fraction vector  $X_{i,k}$ . The boundary variables are mass interior to the face  $m_k$ , radius

$r_k$ , luminosity  $L_k$ , and velocity  $v_k$ . In addition to these basic variables, composite variables are calculated for every cell and face, such as  $\epsilon_{\text{nuc}}$ ,  $\kappa$ ,  $\sigma_k$ , and  $F_k$  (see Table 1 for variable definitions). All variables are evaluated at time  $t + \delta t$  unless otherwise specified.

The density evolution of cell  $k$  is determined by a finite volume form of the mass conservation equation

$$\rho_k = \frac{dm_k}{(4/3)\pi(r_k^3 - r_{k+1}^3)} . \quad (4)$$

For the innermost cell,  $r_{k+1}$  is replaced by the inner boundary condition which is typically zero but can be nonzero for some applications. We reformulate many of our equations to improve numerical stability of the linear algebra and minimize round-off errors. We thus rewrite Equation (4) as

$$\ln r_k = \frac{1}{3} \ln \left[ r_{k+1}^3 + \frac{3}{4\pi} \frac{dm_k}{\rho_k} \right] . \quad (5)$$

The velocity of face  $k$  is zero unless the hydrodynamics option is activated, in which case

$$v_k = r_k \frac{d(\ln r_k)}{dt} \quad (6)$$

is the Lagrangian time derivative of the radius at face  $k$ . For enhanced numerical stability, we rescale this equation by dividing by the local sound speed.

The pressure  $P_k$  is set by momentum conservation at interior cell boundaries,

$$P_{k-1} - P_k = \overline{dm}_k \left[ \left( \frac{dP}{dm} \right)_{\text{hydrostatic}} + \left( \frac{dP}{dm} \right)_{\text{hydrodynamic}} \right] \\ = \overline{dm}_k \left[ -\frac{Gm_k}{4\pi r_k^4} - \frac{a_k}{4\pi r_k^2} \right] , \quad (7)$$

where  $\overline{dm}_k = 0.5(dm_{k-1} + dm_k)$ , and  $a_k$  is the Lagrangian acceleration at face  $k$ , evaluated by the change in  $v_k$  over the timestep  $\delta t$ . The acceleration is set to zero if the hydrodynamic option is not used. Similarly, the temperature of interior cells  $T_k$  is set by energy transport across interior cell boundaries,

$$T_{k-1} - T_k = \overline{dm}_k \left[ \nabla_{T,k} \left( \frac{dP}{dm} \right)_{\text{hydrostatic}} \frac{\bar{T}_k}{\bar{P}_k} \right] , \quad (8)$$

where  $\nabla_{T,k} = d \ln T / d \ln P$  at face  $k$  from the MESA module `mlt` (see Section 5.1),  $\bar{T}_k = (T_{k-1}dm_k + T_kdm_{k-1})/(dm_k + dm_{k-1})$  is the temperature interpolated by mass at face  $k$ , and  $\bar{P}_k = (P_{k-1}dm_k + P_kdm_{k-1})/(dm_k + dm_{k-1})$  is the pressure interpolated by mass at face  $k$ . For enhanced numerical stability, we rescale Equation (7) by dividing by  $\bar{P}_k$  and Equation (8) by dividing by  $\bar{T}_k$ .

The pressure and temperature boundary conditions are constructed by using  $P_s$  and  $T_s$  from the MESA module `atm` (see Section 5.3). The difference in pressure and temperature from the surface to the center of the first cell is found from hydrostatic equilibrium and  $\nabla_T$  by

$$dP_s = \frac{Gm_1 dm_1 / 2}{4\pi r_1^4}, \\ dT_s = dP_s \nabla_{T,1} \frac{T_1}{P_1} . \quad (9)$$

<sup>23</sup> [http://www.phys.au.dk/~jcd/solar\\_models/](http://www.phys.au.dk/~jcd/solar_models/)

<sup>24</sup> <http://forum.astro.keele.ac.uk:8080/nugrid>

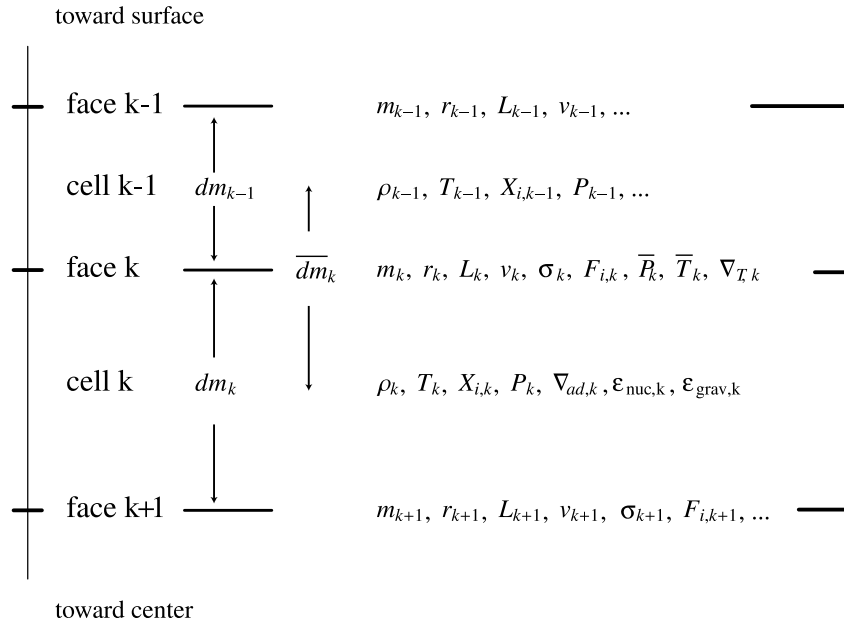


Figure 9. Schematic of some cell and face variables for MESA star.

The boundary conditions are then

$$\begin{aligned} \ln T_1 &= \ln(T_s + dT_s), \\ \ln P_1 &= \ln(P_s + dP_s). \end{aligned} \quad (10)$$

These implicit equations for  $P_1$  and  $T_1$  are solved together with the regular structure and composition equations.

Our finite volume form of energy conservation for cell  $k$  is

$$L_k - L_{k+1} = dm_k(\epsilon_{\text{nuc}} - \epsilon_{v,\text{thermal}} + \epsilon_{\text{grav}}), \quad (11)$$

where  $\epsilon_{\text{nuc}}$  (from module `net` or `jina`) is the total nuclear reaction specific energy generation rate minus the nuclear reaction neutrino-loss rate, and  $\epsilon_{v,\text{thermal}}$  (from module `neu`) is the specific thermal neutrino-loss rate. The  $\epsilon_{\text{grav}}$  term is the specific rate of change of gravitational energy due to contraction or expansion,

$$\epsilon_{\text{grav}} = -T \frac{ds}{dt} = -TC_P \left[ (1 - \nabla_{\text{ad}}\chi_T) \frac{d \ln T}{dt} - \nabla_{\text{ad}}\chi_\rho \frac{d \ln \rho}{dt} \right], \quad (12)$$

where  $d \ln T/dt$  and  $d \ln \rho/dt$  are Lagrangian time derivatives at cell center by mass, and the other symbols are defined in Tables 3 and 6. For the innermost cell,  $L_{k+1}$  is replaced by the inner boundary condition which is typically zero but can be nonzero,  $L_c$ , in specific applications. For additional numerical stability, we rescale Equation (11) by dividing by a scale factor that is typically the surface luminosity of the previous model.

The equation for mass fraction  $X_{i,k}$  of species  $i$  in cell  $k$  is

$$\begin{aligned} X_{i,k}(t + \delta t) - X_{i,k}(t) &= dX_{\text{burn}} + dX_{\text{mix}} \\ &= \frac{dX_{i,k}}{dt} \delta t + (F_{i,k+1} - F_{i,k}) \frac{\delta t}{dm_k}, \end{aligned} \quad (13)$$

where  $dX_{i,k}/dt$  is the rate of change from nuclear reactions reported by `net` or `jina`,  $F_{i,k}$  is the mass of species  $i$  flowing across face  $k$

$$F_{i,k} = (X_{i,k} - X_{i,k-1}) \frac{\sigma_k}{dm_k}, \quad (14)$$

where  $\sigma_k$  is the Lagrangian diffusion coefficient from the combined effects of convection (Section 5.1) and overshoot mixing (Section 5.2). For numerical stability,  $\sigma_k$  is calculated at the beginning of the timestep and held constant during the implicit solver iterations. This assumption accommodates the non-local overshooting algorithm and significantly improves the numerical convergence. It leads to a small inconsistency between the mixing boundary and the convection boundary as calculated at the end of the timestep.

Equations (5), (7), (8), (11), (14), and, optionally Equation (6), are by default solved fully coupled and simultaneously with a first-order backward differencing time integration.

### 6.3. Convergence to a Solution

The generalized Newton–Raphson scheme is represented by

$$0 = \vec{F}(\vec{y}) = \vec{F}(\vec{y}_i + \delta \vec{y}_i) = \vec{F}(\vec{y}_i) + \left[ \frac{d\vec{F}}{d\vec{y}} \right]_i \delta \vec{y}_i + O(\delta \vec{y}_i^2), \quad (15)$$

where  $y_i$  is a trial solution,  $\vec{F}(\vec{y}_i)$  is the residual,  $\delta \vec{y}_i$  is the correction, and  $[d\vec{F}/d\vec{y}]_i$  is the Jacobian matrix.

MESA star uses the previous model, modified by remeshing, mass change, and element diffusion, as the initial trial solution for the Newton–Raphson solver. This is generally successful because we use analytic Jacobians and have sophisticated timestep controls (see Section 6.4). The use of analytic Jacobians in MESA star requires that each of the MESA modules provides not just the required output quantities but also quality, preferentially analytic, partial derivatives with respect to the input quantities. At each timestep, MESA star converges on a final solution by iteratively improving upon the trial solution. We calculate the residuals, construct a Jacobian matrix, and solve the resulting system of linear equations with the solvers in `mtx` to find the corrections to the variables.

The trial solution is accepted when the corrections and residuals meet a specifiable set of comprehensive convergence criteria. In most cases, the solver is able to satisfy these limits in two or three iterations. However, under difficult circumstances

like the He core flash or advanced nuclear burning in massive stars, MESA star can automatically adjust the convergence criteria. The corrections to the variables will, generally, not produce zero residuals because the system of equations is nonlinear. In some cases, the corrections might make the residuals larger rather than smaller. In such cases, the length of the correction vector is reduced by a line search scheme<sup>25</sup> until they improve the residuals. In principle, the residuals can be made arbitrarily small, but this may take a prohibitively large number of iterations. In practice, the use of the line search scheme helps the convergence rate in many cases, but cannot ensure convergence in all cases.

If convergence cannot be achieved with the current timestep, then MESA star will first try again with a reduced timestep (a “retry”) anticipating that a smaller timestep will reduce the nonlinearity. If the retry fails, MESA star will return to the previous model and with a smaller timestep than it used to get to the current model (a “backup”). If the backup fails, MESA star will continue to reduce the timestep until either the model converges or the timestep reaches some pre-defined minimum, in which case the evolutionary sequence is terminated.

#### 6.4. Timestep Selection

Timestep selection is a crucial part of stellar evolution. The timesteps should be small enough to allow convergence in relatively few iterations, but large enough to allow efficient evolutions. Changes to the timestep should also provide for rapid responses to varying structure or composition conditions, but need to be carefully controlled to avoid overcorrections that can reduce the convergence rate.

MESA star does timestep selection as a two stage process. The first stage proposes a new timestep using a scheme based on digital control theory (Soderlind & Wang 2006). The second stage implements a wide range of tests that can reduce the proposed timestep if certain selected properties of the model are changing faster than specified. For the first stage, we use a low-pass filter. The control variable  $v_c$  is the unweighted average over all cells of the relative changes in  $\ln \rho$ ,  $\ln T$ , and  $\ln R$ . The target value  $v_t$  is  $10^{-4}$  by default. For improved stability and response, the low-pass filter method uses the previous two results. Let  $\delta t_{i-1}$ ,  $\delta t_i$ , and  $\delta t_{i+1}$  be the previous, current, and next timestep, respectively, while  $v_{c,i-1}$  and  $v_{c,i}$  are the previous and current values of  $v_c$ . The timestep for model  $i + 1$  is then determined by

$$\delta t_{i+1} = \delta t_i f \left[ \frac{f(v_i/v_{c,i})f(v_t/v_{c,i-1})}{f(dt_i/dt_{i-1})} \right]^{1/4}, \quad (16)$$

where  $f(x) = 1 + 2 \tan^{-1}[0.5(x - 1)]$ . The control scheme implemented by Equation (16) allows rapid changes in timestep without undesirable fluctuations.

The timestep proposed by this low-pass filtering scheme can be reduced according to a variety of special tests that have hard and soft limits. If a change exceeds its specified hard limit, the current solution is rejected, and the code is forced to do a retry or a backup. If a change exceeds its specified soft limit, the next timestep is reduced proportionally. Examples of special tests include limits on the maximum absolute or relative changes in mesh structure, composition variables, nuclear burning rate,  $T_{\text{eff}}$ ,  $L$ ,  $M$ ,  $T_c$ ,  $\rho_c$ , and integrated luminosity from various types of nuclear burning.

<sup>25</sup> This is a globally convergent method and is similar to what is described in Section 9.7 of Press et al. (1992).

#### 6.5. Mesh Adjustment

MESA star checks the structure and composition profiles of the model at the beginning of each timestep and, if necessary, adjusts the mesh. Cells may be split into two or more pieces, or they may be made larger by merging two or more adjacent cells. The overall remeshing algorithm is designed such that most cells are not changed during a typical remesh. This minimizes numerical diffusion and tends to help convergence. Remeshing is divided into a planning stage and an adjustment stage.

The planning stage determines which cells to split or merge based on allowed changes between adjacent cells. Mesh revisions minimize the number of splits and maximize the number of merges while ensuring that the magnitudes,  $\Delta$ , of differences between any two adjacent cells are below specific thresholds:  $\Delta \log P < \theta_P$ ,  $\Delta \log T < \theta_T$ , and  $\Delta \log[X(^4\text{He}) + X(^4\text{He}_0)] < \theta_{\text{He}}$ , where  $X(^4\text{He})$  is the helium mass fraction and  $X(^4\text{He}_0)$  sets an effective lower limit on the sensitivity to the helium abundance. The default thresholds are  $\theta_P = 1/30$ ,  $\theta_T = 1/80$ ,  $\theta_{\text{He}} = 1/20$ , and  $X(^4\text{He}_0) = 0.01$ . Options are available for specifying allowed changes between cells for other mass fractions,  $\Delta \nabla_{\text{ad}}$  and  $\Delta \log(T/(T + T_0))$  for arbitrary  $T_0$ .

Local reductions in the magnitude of allowed changes will place higher resolution in desired regions of the star. For example, the default is to increase resolution in regions of nuclear burning having  $\Delta \log \epsilon_{\text{nuc}}$  large compared to  $\Delta \log P$ . This increase takes effect at a minimum  $\log \epsilon_{\text{nuc}} = -2$  and increases to a maximum factor of four in resolution for  $\log \epsilon_{\text{nuc}} \geq 4$ . The size and range of enhancement can also be set for various specific types of burning. Similarly, it is possible to increase resolution near the boundaries of convection zones over a distance measured in units of the pressure scale height. Different enhancements and distances can be specified for above and below the upper and lower boundaries of zones with or without burning. There are also options to increase spatial resolution in regions having  $\Delta \log X_i$  large compared to  $\Delta \log P$ , or near locations where there are spatial gradients in the most abundant species. Finally, further splitting is done as necessary to limit the relative sizes of adjacent cells.

The adjustment stage executes the remesh plan. Cells to be split are constructed by first performing a monotonicity-preserving cubic interpolation (Steffen 1990) in mass to obtain the luminosities and enclosed volumes at the new cell boundaries. The new densities are then calculated from the new cell masses and volumes, as shown in Equation (4). Next, new composition mass fraction vectors are calculated. For cells being merged, this is straightforward. For cells being split, neighboring cells are used to form a linear approximation of mass fraction for each species as a function of mass coordinate within the cell. The slopes are adjusted so that the mass fractions sum to one everywhere, and the functions are integrated over the new cell mass to determine the abundances.

Finally, the method for calculating the new temperature varies according to electron degeneracy. As the electrons become degenerate (i.e.,  $\eta > 0$ ), split cells simply inherit their temperature while merged cells take on the mass average of their constituent temperatures. If the electrons are not degenerate (i.e.,  $\eta < 0$ ), then a reconstruction parabola is created for the specific internal energy profile of the parent and its neighbor cells (Stiriba 2003). The parabola is integrated over the new cell to find its total internal energy. The new cell temperature is determined by repeatedly calling the eos module using the new composition and density with trial temperatures until the desired internal energy is found.

### 6.6. Mass Loss and Accretion

Mass adjustment for mass loss or accretion is done at each timestep before solving the equations for stellar structure and composition. MESA star offers a variety of ways to set the rate of mass change  $\dot{M}$ . A constant mass accretion or mass-loss rate may be specified in the input files (see Section 6.1). Implementations of Reimers (1975) for red giants, Blöcker (1995) for AGB stars, de Jager et al. (1988) for a range of stars in the H-R diagram, mass loss for massive stars by Glebbeek et al. (2009), Vink et al. (2001), Nugis & Lamers (2000), and Nieuwenhuijzen & de Jager (1990), supersonic mass loss inspired by Prialnik & Kovetz (1995), and super-Eddington mass loss (Paczynski & Proszyński 1986) are available options. An arbitrary mass accretion or mass-loss scheme may be implemented by writing a new module. An example of such a routine provided with MESA star is Mattsson et al. (2010) mass loss for carbon stars. Finally, one may write a wrapper program that calculates  $\dot{M}$  for each timestep and then calls the MESA star module.

Since MESA star allows for simulations with a fixed (and unmodeled) inner mass,  $M_c$ , the total mass is  $M = M_c + M_m$ , where  $M_m$  is the modeled mass. For cell  $k$ , MESA star stores the relative cell mass  $dq_k = dm_k/M_m$  and the relative mass interior to a cell face  $q_k = m_k/M_m = 1 - \sum_{i=1}^{i=k-1} dq_i$  (see Figure 9). Rather than evaluate  $dq_k$  as  $q_k - q_{k+1}$ , it is essential to define  $q$  in terms of  $dq$  to maintain accuracy (Lesaffre et al. 2006). For example, in the outer envelope of a star where the  $q_k$  approach 1, the  $dq_k$  can be  $10^{-12}$  or smaller. Subtraction of two adjacent  $q_k$  to find a  $dq_k$  leads to a intolerable loss of precision.

After a change in mass,  $\delta M$ , has been determined, the mass structure of the stellar model is modified. This procedure changes the mass location of some cells and revises the composition of those cells to match their new location. It does not add or remove cells, nor does it change the initial trial solution for the structure variables such as  $\rho$ ,  $T$ ,  $r$ , or  $L$ . The mass structure is divided into an inner (usually the central regions of the star), an intermediate, and an outer region (usually the stellar envelope). The boundaries of the inner and outer regions are initially set according to temperature, with defaults of  $\log T = 6$  for the inner boundary and  $\log T = 5$  for the outer boundary. This range is automatically expanded, for enhanced numerical stability, if the mass in the intermediate region is not significantly larger than  $\delta M$ . The range is first enlarged by moving the outer boundary to the surface. If the enclosed mass in the intermediate region is still too small, then the inner boundary can be moved inward subject to certain limits. One limit is that the inner boundary does not cross a region of the model where the composition changes rapidly. Another limit is that the fractional mass of the intermediate region cannot change by more than a factor of two from its previous value nor exceed 10% of the total mass.

Once the regions have been defined, the  $dq_k$  are updated. In the inner region the  $dq_k$  are rescaled by  $M/(M+\delta M)$ . Thus,  $dm_k$ ,  $m_k$ , and  $X_k$  have the same values before and after a change in mass to eliminate the possibility of unwanted numerical mixing in the center. In the outer region, cells retain the same value of  $dq_k$  to improve convergence in the high entropy regions of the star (Sugimoto et al. 1981). The  $dq_k$  in the intermediate region are scaled so that  $\sum dq_k = 1$ . The composition of cells in the intermediate and outer regions is then updated. In the case of mass accretion, the composition of the outermost cells whose enclosed mass totals  $\delta M$  is set to match the specified accretion abundances. Cells that were part of the old structure have their compositions set to match the previous composition.

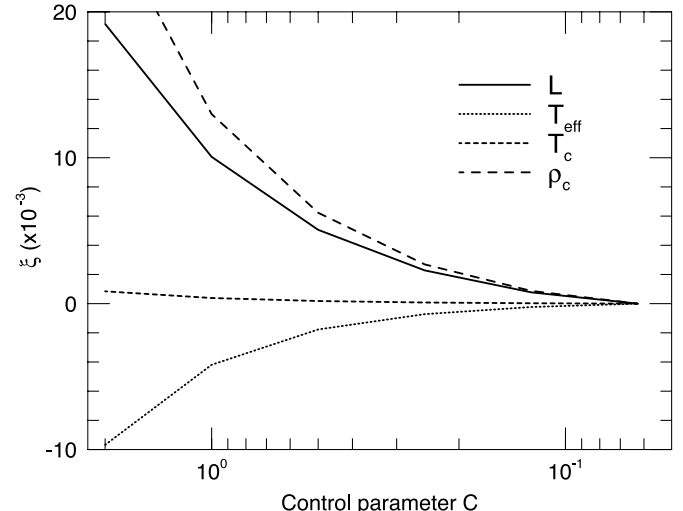


**Figure 10.** Convergence,  $\xi$ , for  $L$ ,  $T_{\text{eff}}$ ,  $T_c$ , and  $\rho_c$  for a  $1 M_\odot$  model at 11.0 Gyr as a function of the control parameter  $C$ . These differences are all with respect to the  $C = 1/16$  model.

### 6.7. Resolution Sensitivity

We examined the resolution convergence properties of a  $1 M_\odot$  model by varying the parameters for mesh refinement and timestepping. The mesh refinement parameter multiplies the limits for variable changes across mesh cells and is closely correlated with the cell size. The timestepping parameter controls the tolerance of the cell average of the relative changes between timesteps in  $\log \rho$ ,  $\log T$ , and  $\log R$  (see Section 6.4) and is closely correlated with the timestep. We varied the mesh refinement and timestepping controls in tandem through a parameter  $C$ , which is a multiplicative factor on their default values of 1 and  $10^{-4}$ , respectively. Therefore,  $C$  is anti-correlated with the time and space resolution.

Table 7 and Figure 10 detail the convergence properties with  $C$  of a solar metallicity,  $1.0 M_\odot$  model with an  $\eta_R = 0.5$  Reimers mass-loss model (Reimers 1975; see Section 6.6). These calculations begin at the ZAMS and are terminated at 11.0 Gyr, when the model stars are turning off the main sequence. As a measure of convergence, we use the difference,  $\xi$ , between a quantity at a given resolution and the quantity at the highest resolution considered ( $C = 1/16$ ). In order to determine how convergence depends on resolution ( $|\xi| \propto C^\alpha$ ), we determine the order of convergence,  $\alpha$ , for increasingly resolved pairs in Table 7:

$$\alpha = \log \left( \frac{\xi_{\text{fine}}}{\xi_{\text{coarse}}} \right) / \log \left( \frac{C_{\text{fine}}}{C_{\text{coarse}}} \right). \quad (17)$$

The convergence orders show that all values converge linearly at large values of  $C$  and display super-linear convergence ( $\alpha \sim 1.6$ ) at smaller values of  $C$ . These convergence orders are plausible given that we use a first-order time integration scheme and a finite volume differencing scheme that is second-order accurate on uniform grids.

Table 8 and Figure 11 detail the same stellar models as a function of  $C$  except the calculations are stopped at  $L = 100 L_\odot$ , when the stars are on the RGB. Table 8 suggests the age of the star converges linearly at larger values of  $C$  and super-linearly ( $\alpha \sim 1.5$ ) at smaller values of  $C$ . However,  $T_{\text{eff}}$ ,  $T_c$ ,  $\rho_c$ ,  $M$ , and  $M_{\text{He}}$  all display oscillatory behavior about the  $C = 1/16$  solution, suggesting factors other than spacetime resolution are

**Table 7**  
 $1 M_{\odot}$  Model Convergence Properties at 11.00 Gyr

Control Parameter, C	2	1	1/2	1/4	1/8	1/16
Number of cells	457	732	1385	2740	5426	10777
Number of timesteps	93	135	225	418	813	1608
$L (L_{\odot})$	2.06094	2.04251	2.03241	2.02678	2.023737	2.02217
$\xi (\times 10^{-3})$	19.17	10.06	5.06	2.28	0.775	0.0
$\alpha$		0.93	0.99	1.15	1.56	
$T_{\text{eff}} (\text{K})$	5543.195	5573.935	5587.434	5593.334	5596.064	5597.361
$\xi (\times 10^{-3})$	-9.68	-4.19	-1.77	-0.72	-0.232	0.0
$\alpha$		1.21	1.24	1.30	1.63	
$\log T_c$	7.301645	7.298305	7.296797	7.296052	7.295676	7.295486
$\xi (\times 10^{-3})$	0.8442	0.3864	0.1797	0.0776	0.0260	0.0
$\alpha$		1.13	1.10	1.21	1.57	
$\log \rho_c$	3.393658	3.348505	3.32615	3.314372	3.308441	3.305552
$\xi (\times 10^{-3})$	26.65	12.99	6.23	2.69	0.874	0.0
$\alpha$		1.04	1.06	1.22	1.61	

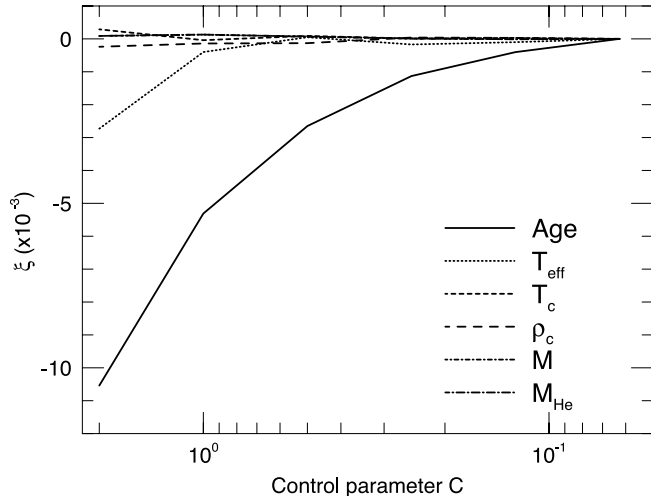


**Figure 11.** Convergence properties in stellar age,  $T_{\text{eff}}$ ,  $T_c$ ,  $\rho_c$ ,  $M$ , and  $M_{\text{He}}$  for a  $M_i = 1 M_{\odot}$  model at  $100 L_{\odot}$  as a function of the control parameter  $C$ . These differences are all relative to the  $C = 1/16$  model. Factors other than the spacetime resolution are dominating the differences for quantities other than the stellar age.

dominating the error at this stage of the evolution. Such factors could be limits in the precision attained by interpolation in the various tables (e.g., 4 significant figures for opacities,  $\sim 6$  significant figures for the OPAL and SCVH EOS), or small changes in boundary conditions.

The lower panel of Figure 12 shows the sound speed profile for the  $100 L_{\odot}$  model with  $C = 1/16$ , our highest resolution case. The helium core and convective zone boundaries are labeled. The mass interior to the convective zone boundary is  $0.95 M_{\odot}$ . The upper panel of Figure 12 shows the convergence properties of the sound speed profile with resolution in the hydrogen layer. Both the  $C = 1$  and  $C = 1/2$  profiles have sound speeds that are smaller than the  $C = 1/16$  profile, while the  $C = 1/4$  and  $C = 1/8$  profiles have larger sound speeds. Note that the difference between the various profiles becomes less as the parameter  $C$  is made smaller, indicating that the convergence rate is becoming smaller. This suggests that factors other than spacetime resolution are dominating the convergence rates at this stage of the evolution. Again, this could be due to the precision attained by table interpolations, small changes in boundary conditions, or differencing errors.

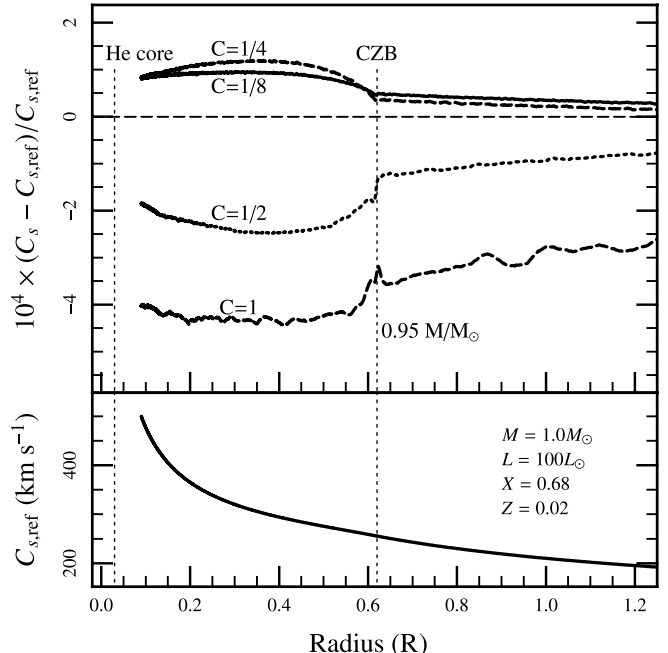


**Figure 12.** Sound speed profile (lower panel) and convergence properties (upper panel) for the  $1 M_{\odot}$  model at  $100 L_{\odot}$  with respect to the reference case,  $C = 1/16$ . The helium core boundary and convective zone boundary are labeled.

### 6.8. Multithreading

MESA modules are designed to be thread-safe (see Section 2), thereby enabling parallel execution. Table 9 lists the execution times in seconds of several specific tasks from four identical evolutionary calculations, each with a different number of threads (one thread per core). The essential difference between modules that scale as the inverse of the number of threads (eos and net) and those that do not (e.g., kap and neu) is the ratio of the overhead associated with parallel execution to the actual time required for each module to perform its calculation. The time required to complete serial tasks sets a lower limit on the total execution time of MESA star.

### 6.9. Visualization with PGstar

By default, MESA star provides alphanumeric output at regular intervals. In addition, it provides the option for concur-

**Table 8**  
 $1 M_{\odot}$  Model Convergence Properties at  $100 L_{\odot}$

Control Parameter, C	2	1	1/2	1/4	1/8	1/16
Number of cells	763	1616	3262	6550	13146	26248
Number of timesteps	689	1181	2291	4547	8992	17812
Age (Gyr)	12.302	12.367	12.400	12.419	12.428	12.433
$\xi (\times 10^{-3})$	-10.54	-5.31	-2.65	-1.13	-0.402	0.0
$\alpha$		0.99	1.00	1.24	1.49	
$T_{\text{eff}}$ (K)	4173.850	4183.587	4185.450	4184.537	4184.823	4185.260
$\xi (\times 10^{-3})$	-2.73	-0.40	0.05	-0.17	-0.10	0.0
$\alpha$		2.77	3.14	-1.93	0.73	
Log $T_c$	7.61573	7.61327	7.61421	7.613652	7.613793	7.613556
$\xi (\times 10^{-3})$	0.29	-0.04	0.09	0.01	0.03	0.0
$\alpha$		2.93	-1.19	2.77	-1.30	
Log $\rho_c$	5.42340	5.42393	5.42402	5.424929	5.424868	5.424713
$\xi (\times 10^{-3})$	-0.24	-0.14	-0.13	0.04	0.03	0.0
$\alpha$		0.75	0.18	1.68	0.48	
$M (M_{\odot})$	0.984444	0.984482	0.984416	0.984356	0.984345	0.984351
$\xi (\times 10^{-3})$	0.09	0.13	0.07	0.01	-0.01	0.0
$\alpha$		-0.49	1.01	3.70	-0.26	
$M_{\text{He}} (M_{\odot})$	0.28080	0.28062	0.28085	0.281016	0.281039	0.281001
$\xi (\times 10^{-3})$	0.09	0.13	0.07	0.01	-0.01	0.0
$\alpha$		-0.49	1.01	3.70	-0.26	

**Table 9**  
Execution Times (s) with Multiple Threads

Task	Number of Threads			
	1	2	4	8
Total <sup>a</sup>	12.2146	8.0099	5.8963	5.0634
Ratio	...	1.53	1.36	1.16
Threaded tasks				
net	6.2602	3.1721	1.6047	0.8182
eos	1.7185	0.8897	0.4539	0.2399
mlt	0.2479	0.1384	0.0704	0.0357
kap	0.2285	0.1386	0.1044	0.0875
neu	0.0240	0.0209	0.0139	0.0098
Subtotal	8.4791	4.3597	2.2473	1.1911
Ratio	...	1.95	1.94	1.89
Fraction of total	0.69	0.54	0.38	0.24
Serial tasks				
File output	1.1848	1.0301	1.0036	1.1679
Matrix linear algebra	0.6569	0.7654	0.7885	0.7926
Miscellaneous	1.8938	1.8547	1.8569	1.9118
Subtotal	3.7355	3.6502	3.6490	3.8723
Fraction of total	0.31	0.46	0.62	0.76

Note. <sup>a</sup> These numbers do not include initialization, e.g., loading of data tables.

rent graphical output. PGstar uses the PGPLOT<sup>26</sup> library to create on-screen plots or images in PNG format that can be post-processed into animations of an evolutionary sequence. A wide variety of visualization options are provided and these are all configurable through the PGstar inlist. For example, the PGstar window can simultaneously hold: an H-R diagram, a  $T_c - \rho_c$  diagram, and interior profiles of physical variables, such as nuclear energy generation, and composition. Animation is very useful for visualizing complex, time-dependent processes. For example, view the short selection from the MESA Web site that shows the He core flash in a  $1 M_{\odot}$  star.<sup>27</sup>

<sup>26</sup> We thank Philip Pinto for initiating this MESA capability, see <http://www.astro.caltech.edu/~tjp/pgplot/>

<sup>27</sup> <http://mesa.sourceforge.net/pdfs/1MHeflash.mov>

## 7. MESA star RESULTS: COMPARISONS AND CAPABILITIES

As with any modeling approach, MESA star must be verified (“Is it solving the equations correctly?”; Roache 1998) and validated (“Does it solve the right equations?”) to demonstrate its accuracy and predictive credibility (e.g., Oberkampf 2004). V&V is a maturing discipline (e.g., Roache 1998; Calder et al. 2002), with the goal of assessing the error and uncertainty in a numerical simulation, which also includes addressing sources of error in theory, experiment, observation, and computation (Calder et al. 2004). The results of V&V testing are historical statements of reproducible evidence that a simulation demonstrates a quantified level of accuracy in the solution of a specific problem.

V&V is an ongoing activity for MESA via the MESA test suite (see Appendix B), where code modules are tested individually, and, where possible, the integrated code MESA star is verified and validated. Verification for MESA includes a systematic study of the effect of mesh and timestep refinement on simulation accuracy (Section 6.7), specific module comparisons (Section 5.5), and stellar evolution code comparisons presented in this section.

This section shows MESA star evolution calculations of single stellar and substellar objects with  $10^{-3} M_{\odot} < M < 1000 M_{\odot}$  (in Sections 7.1–7.3) as well as verification results (Sections 7.1.1, 7.1.2, 7.2.1, 7.2.2, 7.3.1, and 7.3.2). In Section 7.1.3, we compare the MESA star Solar model with helioseismic data. As examples of the many other experiments that are possible with MESA, we model prolonged accretion of He onto a neutron star and a mass-transfer scenario relevant to cataclysmic variables in Section 7.4.

### 7.1. Low-mass Stellar Structure and Evolution

MESA star has sufficiently broad input physics to compute the evolution of low-mass stars and substellar objects down to Jupiter’s mass ( $\approx 10^{-3} M_{\odot}$ ), as well as complete evolutionary sequences of low-mass stars ( $M \lesssim 2 M_{\odot}$ ) from the PMS to the white dwarf cooling curve without any intervention. Figure 13 shows evolutionary tracks in the H-R diagram for 1 and  $1.25 M_{\odot}$

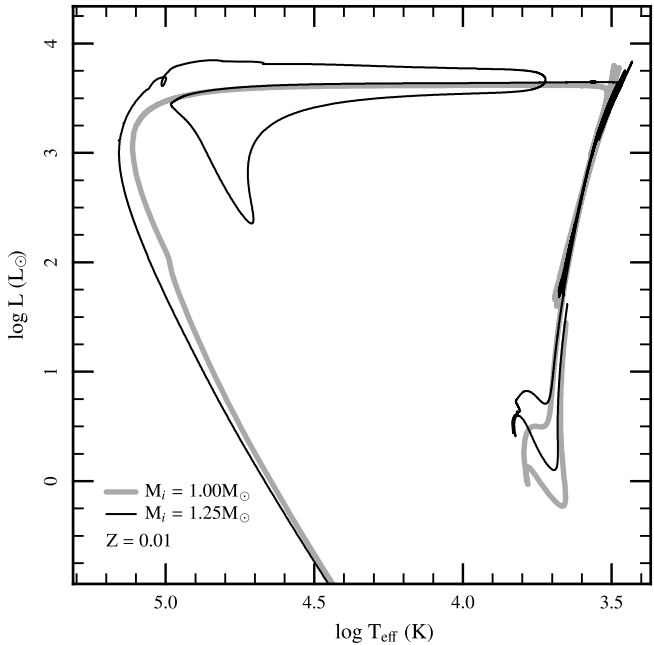


**Figure 13.** MESA star evolution of a  $1 M_{\odot}$  and a  $1.25 M_{\odot}$ ,  $Z = 0.01$  star from the PMS to cooling white dwarfs.

models with  $Z = 0.01$ .<sup>28</sup> The  $1.25 M_{\odot}$  model exhibits a late He-shell flash during the pre-white dwarf phase.

Figure 14 provides further examples, spanning  $0.9$ – $2 M_{\odot}$  at  $Z = 0.02$ ; for clarity, the PMS portion of the tracks was removed and the runs were terminated after the models left the thermally pulsating asymptotic giant branch (TP-AGB). The bottom panel shows the evolution in the  $T_c$ – $\rho_c$  plane, exhibiting the convergence of the  $0.9$ ,  $1.2$ , and  $1.5 M_{\odot}$  models to nearly identical, degenerate, helium cores when on the RGB. The  $2 M_{\odot}$  model ignites He at a lower level of degeneracy.

Though the required MESA star timesteps get short ( $\approx$  hours) during the off-center He core flash in the  $0.9$ ,  $1.2$  and  $1.5 M_{\odot}$  models, the stellar model does not become dynamic; the entropy change timescales are always longer than the local dynamical time (Thomas 1967; Serenelli & Weiss 2005; Shen & Bildsten 2009; Mocak et al. 2009). The reduction of hydrostatic pressure in the core at the onset of flashes leads to the adiabatic expansion of the core, visible as the drop in  $T_c$  at constant degeneracy. Successive He flashes (Thomas 1967; Serenelli & Weiss 2005) work their way into the core over a  $2 \times 10^6$  year timescale, eventually heating it (at nearly constant pressure; see the dashed red line in the bottom panel of Figure 14) to ignition and arrival onto the horizontal branch. The further evolution during He burning and the thermal pulses is seen in the bottom panel, where the small changes in the C/O core during thermal pulses on the AGB are resolved in MESA star.

We start the more detailed calculations and comparisons to previous work in Section 7.1.1 by displaying the MESA star PMS evolution of low-mass stars, brown dwarfs and giant planets, and comparing to prior results of Baraffe et al. (2003).

#### 7.1.1. Low-mass Pre-main Sequence Stars, Contracting Brown Dwarfs and Giant Planets

The PMS evolution of low-mass stars (Burrows et al. 1989; D’Antona & Mazzitelli 1994; Baraffe et al. 1998) and gravitationally contracting brown dwarfs and giant planets (Burrows

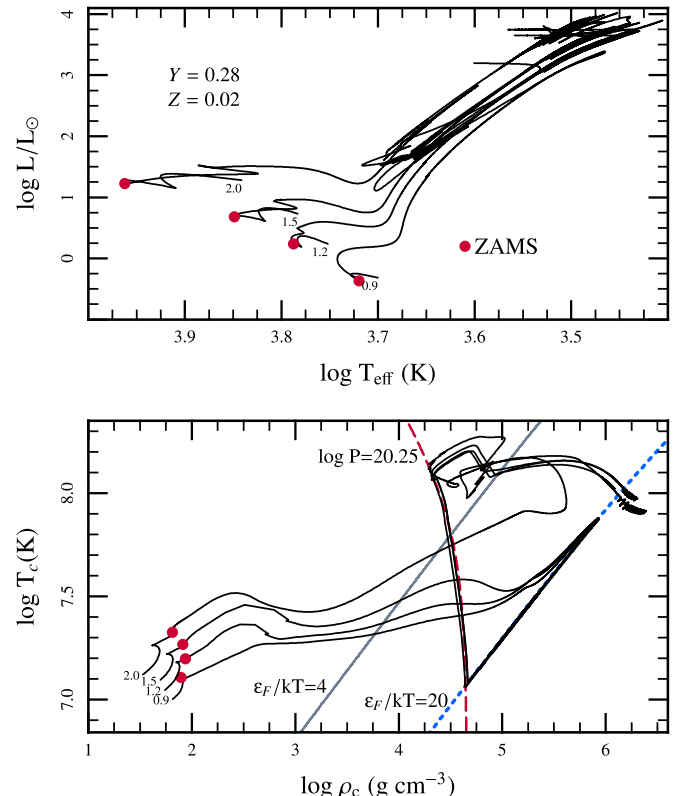


**Figure 14.** Evolution from MESA star of  $0.9$ ,  $1.2$ ,  $1.5$ , and  $2 M_{\odot}$  stars with  $Z = 0.02$  up to the end of the TP-AGB. The top panel shows their evolution in the H-R diagram, where the solid red point is the ZAMS. The bottom panel shows the evolution in the  $T_c$ – $\rho_c$  plane, exhibiting the He core flash and later evolution of the C/O core during the thermal pulses. The dashed blue (heavy gray) line shows a constant electron degeneracy of  $\epsilon_F/k_B T = 20(4)$ . The dashed red line is for a constant pressure of  $\log P = 20.25$ ; relevant to the He core flash.

(A color version of this figure is available in the online journal.)

et al. 1997; Chabrier et al. 2000; Chabrier & Baraffe 2000; Burrows et al. 2001) has been studied extensively. The lasting importance of these problems motivates us to ensure that MESA star can successfully perform these evolutions.

Figure 15 shows the evolution of PMS stars with masses of  $0.08 M_{\odot} < M < 1 M_{\odot}$ . Each solid line starts on the PMS Hayashi track for a fixed mass,  $M$ , and ends at an age of 1 Gyr. All stars with  $M \geq 0.2 M_{\odot}$  have reached the ZAMS ( $L = L_{\text{nuc}}$ ) by this time. The red circles show the location where the  $^7\text{Li}$  is depleted by a factor of 100, but only for  $M < 0.5 M_{\odot}$ . Stars with  $M > 0.5 M_{\odot}$  deplete their  $^7\text{Li}$  after the core becomes radiative (D’Antona & Mazzitelli 1994; Chabrier et al. 1996; Bildsten et al. 1997), adding an uncertain dependence on convective overshoot that we do not investigate here.

Lower-mass stars ( $M < 0.3 M_{\odot}$ ) remain fully convective throughout their PMS and arrival on the main sequence. In Figure 16 we show the evolution in the  $T_c$ – $\rho_c$  plane for these objects. The light solid line in the upper left denotes the  $T_c \propto \rho_c^{1/3}$  relation expected during the Kelvin–Helmholtz contraction for a fixed mass non-degenerate star. Deviations from this relation occur when electron degeneracy occurs, which is shown by the gray line at  $\eta \approx \epsilon_F/k_B T = 4$ , roughly where the electron degeneracy has increased the electron pressure to twice that of an ideal electron gas. We extend the mass range down to  $M = 0.01 M_{\odot}$  to reveal the distinction between main sequence stars and brown dwarfs. That distinction becomes clearer in

<sup>28</sup> Each calculation takes a few hours on a laptop computer.

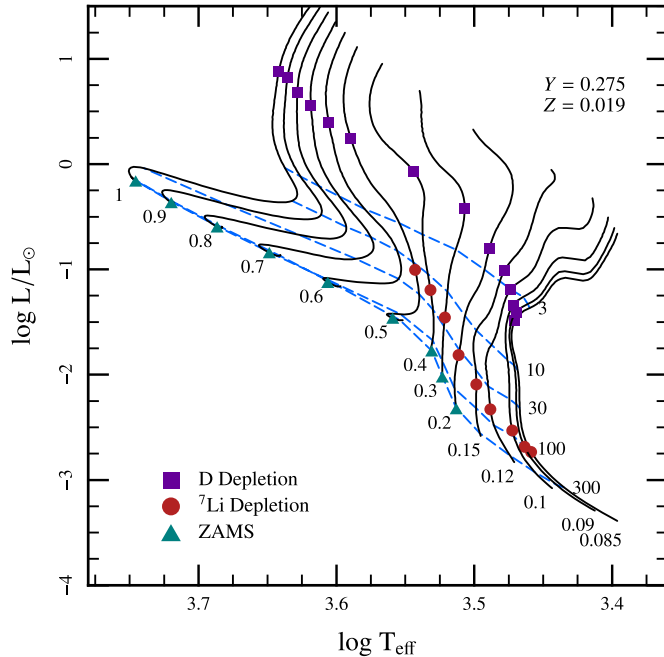


**Figure 15.** Location in the Hertzsprung-Russell (H-R) diagram for  $0.085 M_{\odot} < M < 1 M_{\odot}$  stars as they arrive at the main sequence for  $Y = 0.275$  and  $Z = 0.019$ . The mass of the star is noted by the values at the bottom of the line. The dashed blue lines are isochrones for ages of 3, 10, 30, 100 and 300 Myr, as noted to the right. The purple squares ( ${}^7\text{Li}$ ) show where D ( ${}^7\text{Li}$ ) is depleted by a factor of 100. The green triangles show the ZAMS.

(A color version of this figure is available in the online journal.)

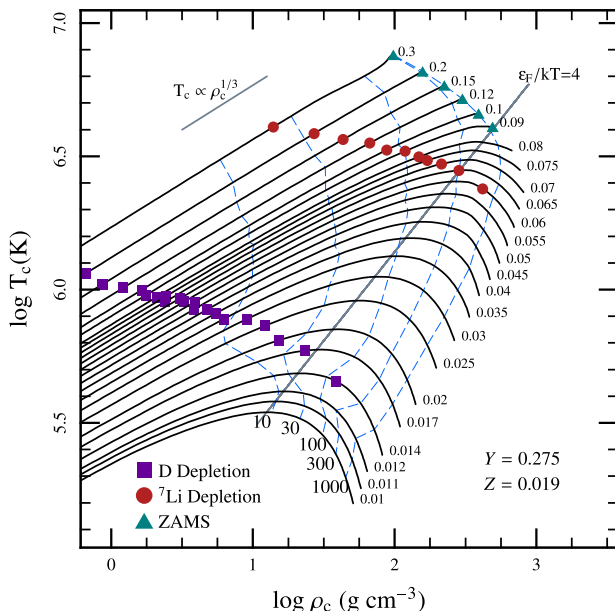


**Figure 16.** Trajectories of central conditions for fully convective  $M < 0.3 M_{\odot}$  stars as they approach the main sequence ( $M > 0.08 M_{\odot}$ ) or become brown dwarfs for  $Y = 0.275$  and  $Z = 0.019$ . Each solid line shows  $T_c$  and  $\rho_c$  for a fixed mass,  $M$ , noted at the end of the line (when the age is 3 Gyr). The dashed blue lines are isochrones for ages of 10, 30, 100, 300 Myr and 1 Gyr. The purple squares and red circles show where D and  ${}^7\text{Li}$  is depleted by a factor of 100. The green triangles show the ZAMS.

(A color version of this figure is available in the online journal.)

Figure 17 which shows the  $L$  evolution for a range of stars with  $M < 0.3 M_{\odot}$ . Only the  $M > 0.08 M_{\odot}$  stars asymptote at late times to a constant  $L$ , whereas the others continue to fade. We also exhibit the expected scaling for a contracting

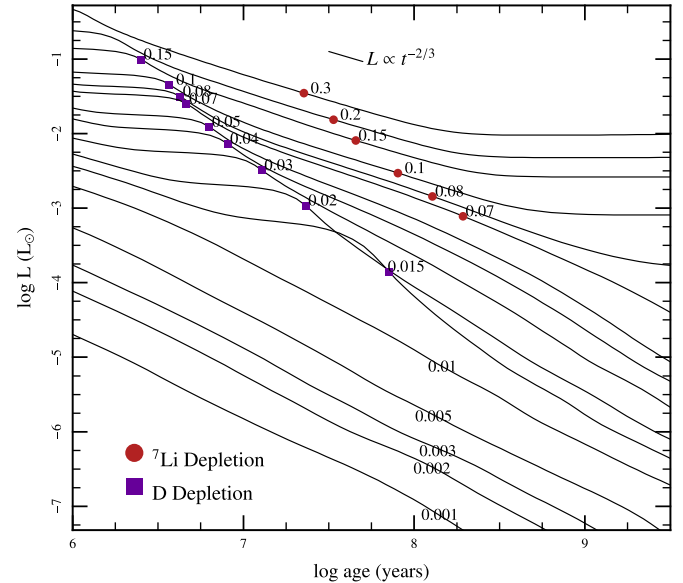


**Figure 17.** Luminosity evolution for fully convective  $M < 0.3 M_{\odot}$  stars as they approach the main sequence ( $M > 0.08 M_{\odot}$ ) or become brown dwarfs for  $Y = 0.275$  and  $Z = 0.019$ . From top to bottom, the lines are for  $M = 0.3, 0.2, 0.15, 0.1, 0.08, 0.07, 0.05, 0.04, 0.03, 0.02, 0.015, 0.01, 0.005, 0.003, 0.002$ , and  $0.001 M_{\odot}$ . The purple squares (red circles) denote where D ( ${}^7\text{Li}$ ) is depleted by a factor of 100.

(A color version of this figure is available in the online journal.)

fully convective star with a constant  $T_{\text{eff}}$ ,  $L \propto t^{-2/3}$ . At the D mass fraction of this calculation,  $X_D = 3 \times 10^{-5}$ , the onset of D burning provides some luminosity for a finite time, causing the evident kink at early times.

MESA star models evolved from the PMS Hayashi line to an age of 10 Gyr with masses ranging from 0.09 to  $0.001 M_{\odot}$  are compared with the models of Baraffe et al. (2003, BCBAH) in Figure 18. Ages in increasing powers of 10 are marked by filled circles along each track from 1 Myr to 10 Gyr. For comparison, separate points from the BCBAH evolutionary models are plotted as plus symbols (“+”). So as to match the choice of BCBAH, we set the D mass fraction at  $X_D = 2 \times 10^{-5}$  (Chabrier et al. 2000). Evolution at the youngest ages is uncertain due to different assumptions regarding D burning but beyond 10 Myr the MESA star and the BCBAH models overlap at almost every point. Note that the BCBAH models were only evolved to 5 Gyr for the two lowest masses shown in Figure 18.

### 7.1.2. Code Comparisons of $0.8 M_{\odot}$ and $1 M_{\odot}$ Models

The Stellar Code Calibration Project (Weiss et al. 2007) was created to provide insight into the consistency of results obtained from different state-of-the-art stellar evolution codes. The contributors performed a series of stellar evolution calculations with the physics choices held constant to the greatest extent possible. This section compares MESA star models with published results from that project for two specific cases. The comparison codes are BaSTI/FRANEC (Pietrinferni et al. 2004), DSEP (Dotter et al. 2007), and GARSTEC (Weiss & Schlattl 2008). MESA star models lie within the range exhibited by BaSTI/FRANEC, DSEP, and GARSTEC in these comparisons.

Two examples are shown here,  $0.8 M_{\odot}$ ,  $Z = 10^{-4}$  evolutionary tracks (Figure 19) and  $1 M_{\odot}$ ,  $Z = 0.02$  evolutionary tracks (Figure 20). In both cases the models were evolved from the pre-MS to the onset of the He core flash. The models assume, as much as possible, the same nuclear reaction rates (NACRE),

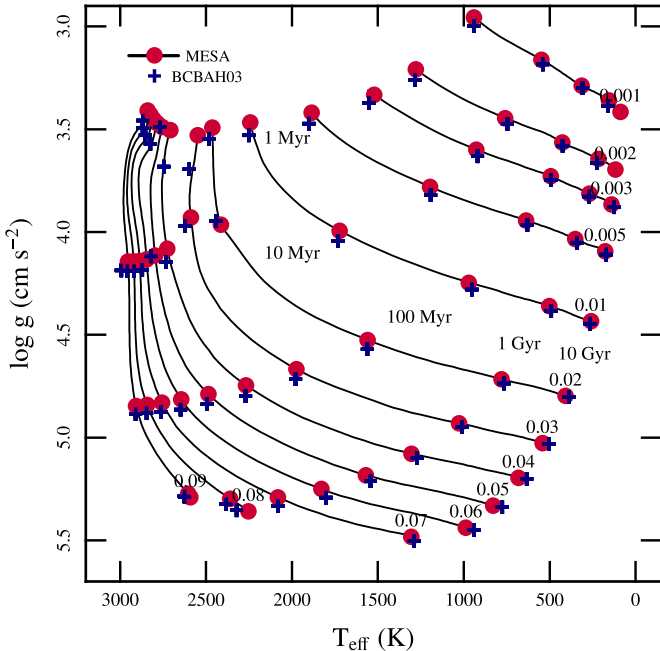


**Figure 18.** Evolution of very low mass stars and substellar objects from  $0.09$  to  $0.001 M_{\odot}$  for  $Z = 0.02$ ,  $Y = 0.28$  in the  $\log(g)$ - $T_{\text{eff}}$  plane. The solid lines are the MESA star tracks, with labeled masses (in  $M_{\odot}$ ) at the bottom of each. The filled circles denote the location of each track at a given age. The plus symbols (+) mark the locations of the BCBAH tracks for the same masses and ages. The two lowest mass tracks from BCBAH do not extend to 10 Gyr.

(A color version of this figure is available in the online journal.)

opacities (OPAL and Alexander & Ferguson 1994), equation of state (FreeEOS), and mixing length ( $\alpha_{\text{MLT}} = 1.6$ ). These

tests do not represent the best models for the various codes. Instead, the goal of the comparisons was to see how consistent the codes would be when using simple assumptions and comparable input physics (Weiss et al. 2007). While the agreement is good in most respects, in temporal resolution there is a discrepancy.

The H-R diagram of the  $0.8 M_{\odot}$ ,  $Z = 10^{-4}$  case in Figure 19 is nearly identical for all four tracks except near the main sequence turnoff, where DSEP and BaSTI/FRANEC are hotter than MESA star and GARSTEC. These models have essentially no convection during the main sequence and there is remarkably little scatter during this phase. In the  $T_c$ - $L$  plane, the models are almost indistinguishable until they enter the red giant phase at  $L \approx 10 L_{\odot}$ , where the central temperatures differ slightly only to re-converge at maximum luminosity on the RGB. Finally, the lifetime-luminosity plane indicates that the four codes split into two pairs with one pair shorter lived by  $\approx 5\%$  than the other pair. It is beyond our scope here to explain the reasons for these differences; the purpose of the present comparison is to indicate that MESA star produces results that are consistent with the range exhibited among the other three codes.

Convection plays a more prominent role in the  $1 M_{\odot}$ ,  $Z = 0.02$  case, as shown in Figure 20, and the scatter is greater than in the  $Z = 10^{-4}$  case. The BaSTI/FRANEC model is hotter than the other three models. Treatment of convection and, in particular, the resolution of the surface convection zone is primarily responsible for the spread seen in the main sequence portion of the tracks.

In both cases, the central conditions are very similar until the models become red giants. In the  $Z = 0.02$  case, the range of lifetimes is somewhat reduced compared to the  $Z = 10^{-4}$  case with BaSTI/FRANEC and MESA star shortest (though the order is reversed with respect to the  $Z = 10^{-4}$  case) followed by DSEP and then GARSTEC.

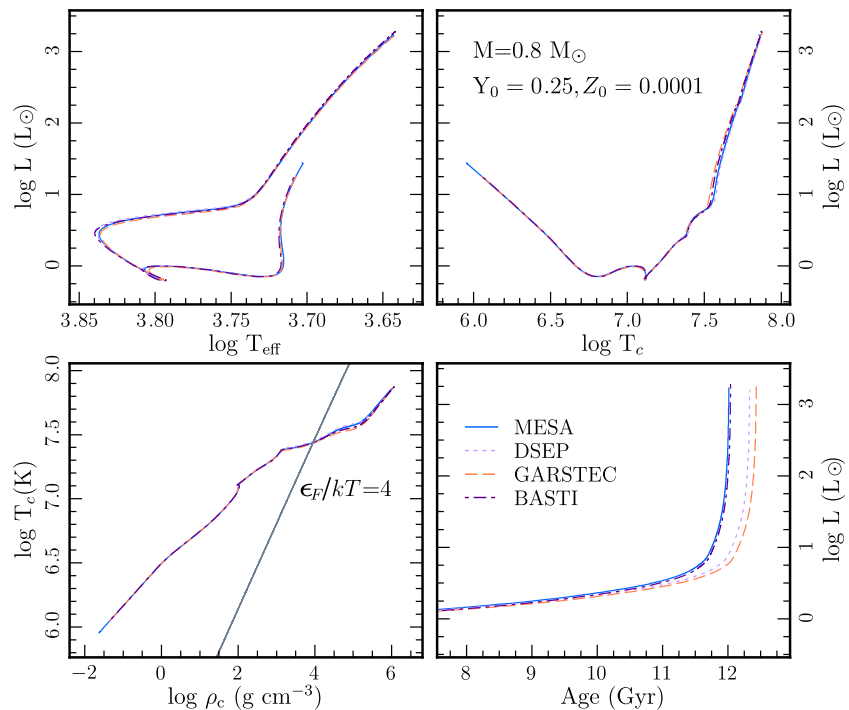


**Figure 19.** Stellar Code Calibration Project evolutionary tracks for the  $0.8 M_{\odot}$ ,  $Z = 10^{-4}$  case. The upper left panels show the H-R diagram; upper right panels show luminosity vs. central temperature; lower left panels show central  $T$ - $\rho$ ; lower right shows luminosity vs. age.

(A color version of this figure is available in the online journal.)

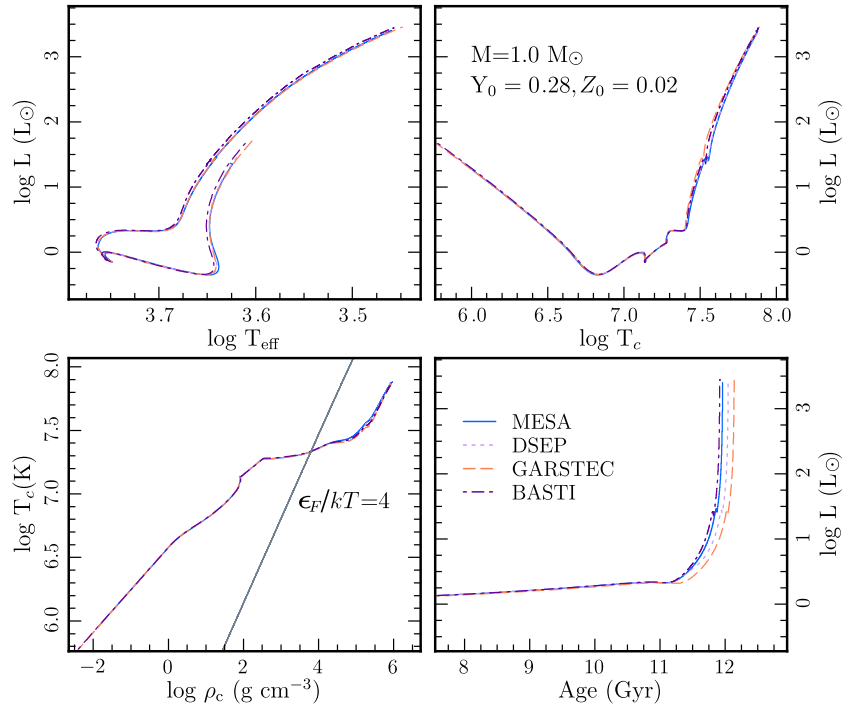


**Figure 20.** Stellar code calibration project evolutionary tracks for the  $1 M_{\odot}$ ,  $Z = 0.02$  case.  
 (A color version of this figure is available in the online journal.)

### 7.1.3. The MESA star Solar Model

MESA star performs a Solar model calibration by iterating on the difference between the final model and the adopted solar parameters of  $L_{\odot}$  and  $R_{\odot}$  (from Bahcall et al. 2005) and the surface value of  $Z_s/X_s$  from Grevesse & Sauval (1998) at 4.57 Gyr. This is done by iteratively varying  $\alpha_{MLT}$  and the initial  $Y_i$  and  $Z_i$  values (all for the abundance ratios of Grevesse & Sauval 1998), while including diffusion.

The properties of the converged model (which reaches the desired parameters to better than one part in  $10^5$ ) are shown in Table 10, and match the measured depth,  $R_{CZ}$ , of the surface convection zone within  $1\sigma$  and the surface helium abundance,  $Y_s$ , within  $2\sigma$  (Bahcall et al. 2005). The difference between the model and the helioseismologically inferred solar sound speed profile is compared with similar results from Bahcall et al. (1998, BBP98) and Serenelli et al. (2009, S09) in Figure 21 demonstrating that MESA star is capable of stellar evolution calculations at the level of one part in  $10^3$  demonstrated by others (Basu & Antia 2008).

### 7.2. Intermediate-mass Structure and Evolution

MESA star can calculate the evolution of intermediate-mass stars ( $2 \lesssim M/M_{\odot} \lesssim 10$ ) through the He-core burning phase and the advanced He-shell burning AGB phase. MESA star produces results compatible with published results from existing stellar evolution codes.

We start by showing in Figure 22 a grid of MESA star evolutionary tracks with masses ranging from 2 to  $10 M_{\odot}$  with  $Z = 0.02$ . The top panel shows the evolution in the H-R diagram, while the bottom panel shows the evolution in the  $T_c - \rho_c$  diagram. The  $8$  and  $10 M_{\odot}$  models start to ignite carbon burning off center, whereas the  $2-7 M_{\odot}$  models do not and will presumably go on to form C/O core white dwarfs. The lack of a complete treatment in MESA star of liquid diffusion inhibits

**Table 10**  
 MESA star Standard Solar Model at 4.57 Gyr

Quantity	Value
Converged input parameters	
$\alpha_{MLT}$	1.9179113764
$Y_i$	0.2744267987
$Z_i$	0.0191292323
Properties of converged model	
$(Z/X)_s$	0.02293
$X_s$	0.73973
$Y_s$	0.24331
$Z_s$	0.01696
$X_c$	0.33550
$Z_c$	0.02125
$R_{CZ}/R_{\odot}$	0.71398
$\log \rho_c$	2.18644
$\log P_c$	17.3695
$\log T_c$	7.19518
rms[( $c_{\text{Model}} - c_{\odot})/c_{\odot}$ )]	0.00093

our ability to verify the resulting white dwarf cooling sequences from MESA star at this time.

### 7.2.1. Comparison of EVOL and MESA star

We compare  $M_i = 2 M_{\odot}$ ,  $Z = 0.01$  stellar models from MESA star and EVOL (Blöcker 1995; Herwig 2004; Herwig & Austin 2004) starting from the PMS to the tip of the thermal pulse AGB (TP-AGB). Both codes employed the exponentially decaying overshoot mixing treatment described by Herwig (2000; see Section 5.2) at all convective boundaries with  $f = 0.014$ , except during the third dredge-up where we adopt  $f = 0.126$  at the bottom of the convective envelope to account for the formation of a  $^{13}\text{C}$  pocket, and at the bottom of the

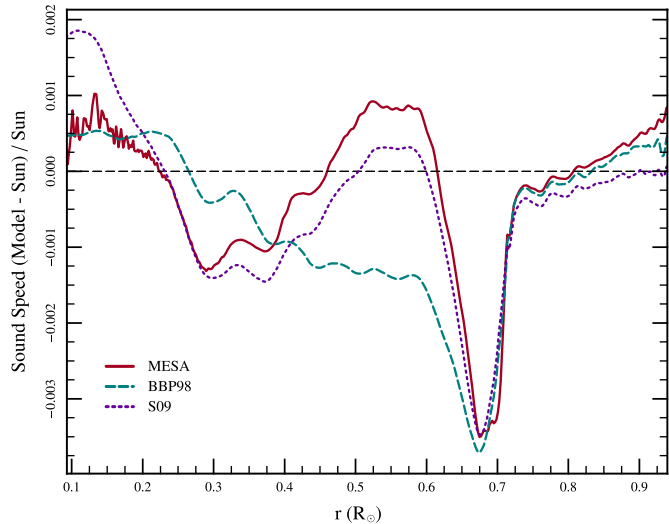


**Figure 21.** Comparisons of the sound speed profiles within the sun. The red solid line shows the relative difference in the sound speed between MESA star predictions and the inferred sound speed profile from helioseismic data (taken from Bahcall et al. 1998). The green-dashed and blue-dotted lines show the same for the standard solar models of Bahcall et al. (1998, BBP98) and Serenelli et al. (2009, S09), respectively.

(A color version of this figure is available in the online journal.)

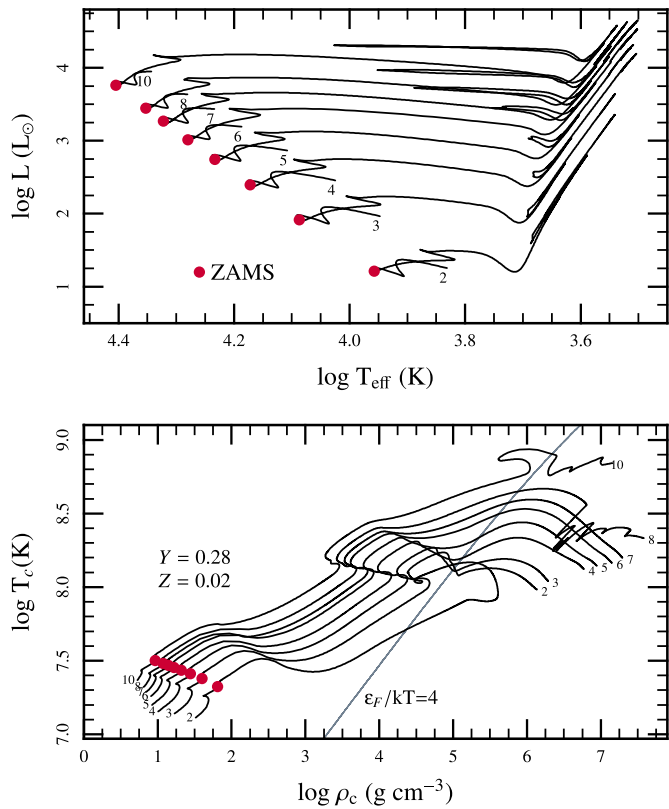


**Figure 22.** Top: MESA star H-R diagram for  $2-10 M_{\odot}$  models from the PMS to the end of the first thermal pulse ( $2-7 M_{\odot}$ ) or into C-burning (8 and  $10 M_{\odot}$ ). Bottom: trajectories of the central conditions. The filled red points show the ZAMS.

(A color version of this figure is available in the online journal.)

He-shell flash convection zone we use  $f = 0.008$  (Herwig 2005).

In both codes we use the mass-loss formula of Blöcker (1995, see Section 6.6). Thermal pulses start at a slightly lower core

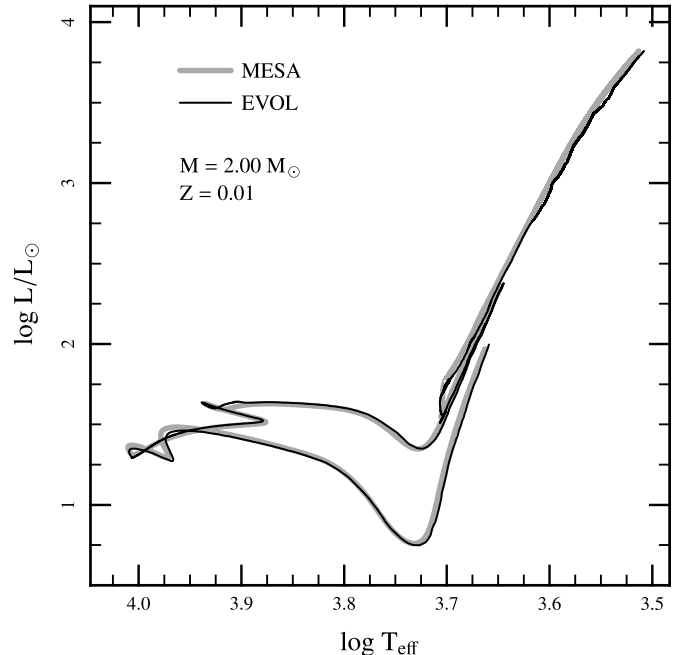


**Figure 23.**  $2 M_{\odot}$ ,  $Z = 0.01$  tracks up to the first thermal pulse from EVOL (solid black line) and MESA star (thick gray line) in the H-R diagram.

mass, and hence luminosity, in the EVOL model. In order to maintain similar envelope mass evolution through the TP-AGB, the parameter  $\eta_{\text{BL}}$  in the mass-loss formula was set to 0.05 in MESA star and 0.1 in EVOL. Every effort has been made to tailor the MESA star model to the EVOL model. However, the AGB evolution is very sensitive to the initial core mass, which depends on the mixing assumptions and their numerical implementation during the preceding He-core burning phase. Consequently, small differences on the TP-AGB are unavoidable when comparing tracks from two codes.

As shown in Figure 23, the EVOL and MESA star tracks compare well in the H-R diagram. Table 11 shows that key properties differ by less than 5%. MESA star has the ability to impose a minimum size on convection zones below which overshoot mixing is ignored. EVOL does not have such limits, leading to more mixing of He into the core and, hence, the  $\approx 4\%$  larger age of the EVOL sequence at the first thermal pulse.

The TP-AGB is characterized by recurrent thermonuclear instabilities of the He-shell, leading to complex mixing and nucleosynthesis. These processes are properly represented in MESA star calculations, as revealed in Figure 24. The ability of MESA star to calculate the evolution of stellar parameters in a smooth and continuous manner even during the advanced thermal pulse phases and beyond is demonstrated in Figure 25. The top panel shows the evolution in the H-R diagram, whereas the bottom panel shows the evolution of the conditions in the C/O core. The adiabatic cooling in the C/O core that occurs during the He flash (due to the pressure dropping at the surface of the C/O core) is evident in the downturns that are parallel to the line of constant degeneracy (which is also the adiabatic slope). The overall trend of increasing  $\rho_c$  reflects the growing C/O core mass, which for this model is shown in the top panel of Figure 24.

An example of the evolution of convection zones, shell burning, and total luminosities as well as core boundaries for two subsequent thermal pulses is shown in Figure 26 as a function of model number; compare to Figure 3 in Herwig (2005).

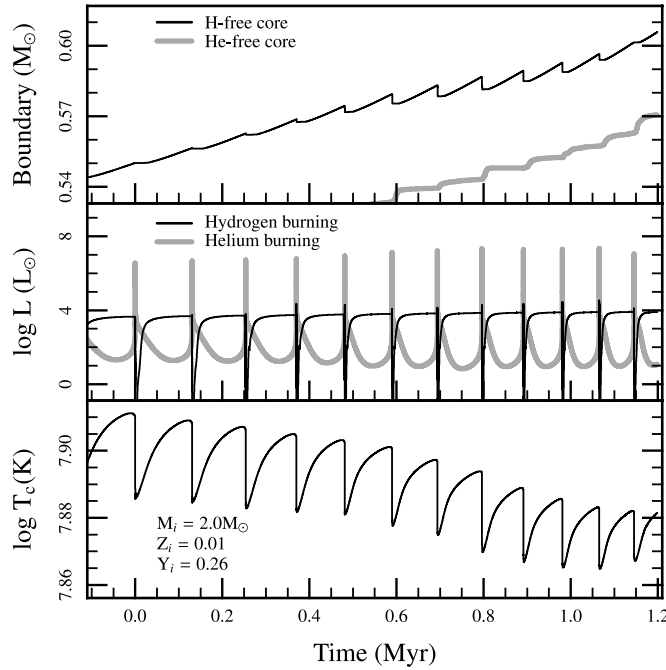


**Figure 24.** Properties of an  $M_i = 2 M_\odot$  star from MESA star as it approaches the end of the AGB. Top: the boundaries of the C/O core and the He layer. Middle: luminosities from hydrogen and helium burning. Bottom: central temperature evolution.

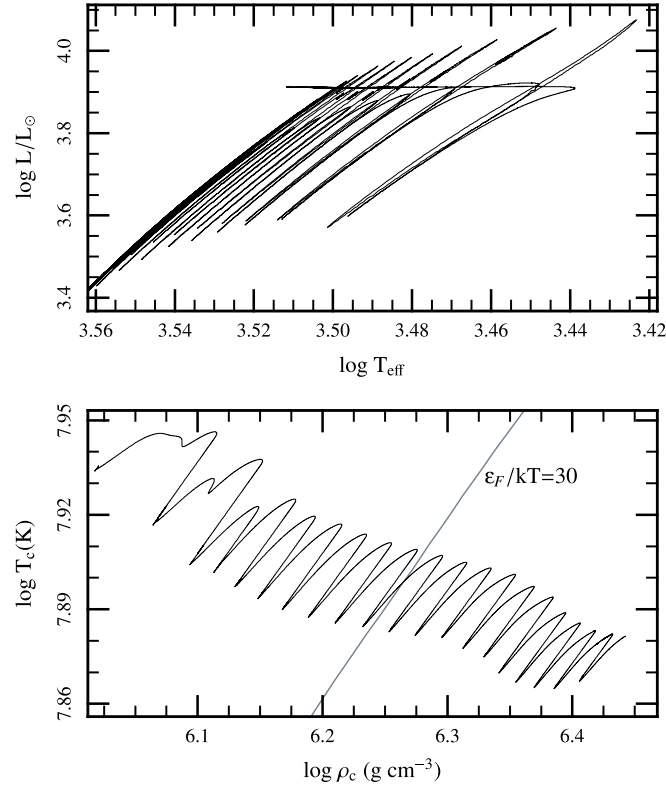


**Figure 25.** Top: H-R diagram for the  $2 M_\odot$  MESA star model from Figures 23 and 24 during the AGB thermal pulses. Bottom: trajectories of the same model's central conditions in during the same interval. The line showing constant degeneracy is marked.

Quantitative comparison of interpulse time, core growth, and dredge-up amount (see Table 11) shows excellent agreement between the MESA star thermal pulses and the equivalent pulses in the EVOL sequence.

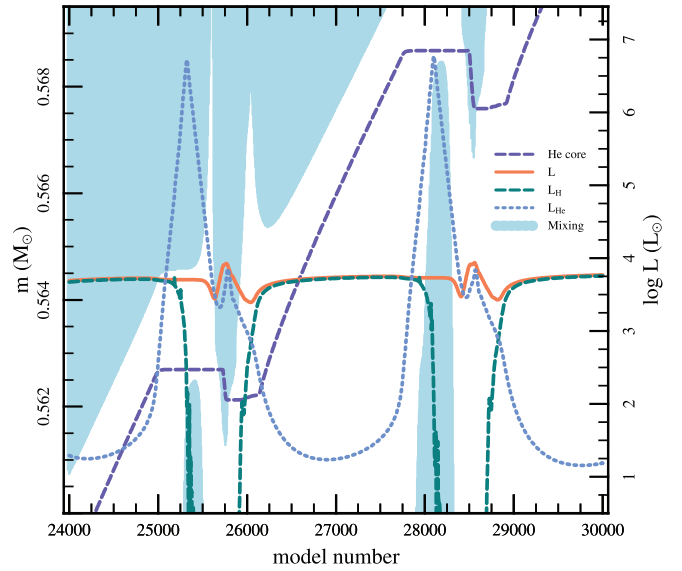


**Figure 26.** Kippenhahn diagram with luminosities for the second and third thermal pulses with third dredge-up of the  $2 M_\odot$ ,  $Z = 0.01$  MESA star track shown in Figure 24.

(A color version of this figure is available in the online journal.)

**Table 11**  
Comparison of MESA star and EVOL Models with  $M_i = 2 M_\odot$ ,  $Z = 0.01$

Quantity	MESA star	EVOL
Main-sequence lifetime (Gyr)	0.939	0.962
Deepest penetration of first dredge-up ( $M_\odot$ )	0.328	0.327
H-free core mass at the end of He-core burning ( $M_\odot$ )	0.466	0.454
Core mass at first thermal pulse ( $M_\odot$ )	0.504	0.481
Age at first thermal pulse (Gyr)	1.269	1.328
Core mass at second thermal pulse with DUP ( $M_\odot$ )	0.563	0.563
Following interpulse time (1000 yr)	116	106
Following pulse-to-pulse core growth ( $10^{-3} M_\odot$ )	6.4	6.9
Dredge-up mass at following pulse ( $10^{-3} M_\odot$ )	1.1	1.3

Another important property of the He-shell flashes is the intershell abundance as a result of the convective mixing and burning. Again, the comparison of results from both codes shows good agreement, which is expected since they both implement the same overshooting mixing assumptions for the He-shell flash convection zone. A consequence of the third dredge-up is the gradual increase of the envelope C/O ratio as thermal pulses repeatedly occur. Since the  $2 M_\odot$  models do not experience hot-bottom burning, the evolution of this ratio is an effective probe of the cumulative efficiency of the third dredge-up in these simulations.<sup>29</sup> The top panel of Figure 27 shows the surface C/O ratio evolution according to EVOL (dashed red line) and MESA star (solid black line). They are in good agreement, e.g., in terms of the time period over which the third dredge-up occurs and the amount by which C/O increases. The mass-loss history over the same time period, shown in the bottom panel of Figure 27, is similar by design.

### 7.2.2. Interior Structure of Slowly Pulsating B Stars and Beta Cepheids

The advent of space-based asteroseismology for main-sequence B stars with the *CoRot* (Degroote et al. 2009) and

<sup>29</sup> For massive AGB stars, MESA star shows the expected hot-bottom burning behavior, including, for example, the avoidance of the C-star phase for a  $5 M_\odot$ ,  $Z = 0.01$  stellar model track despite efficient third dredge-up.

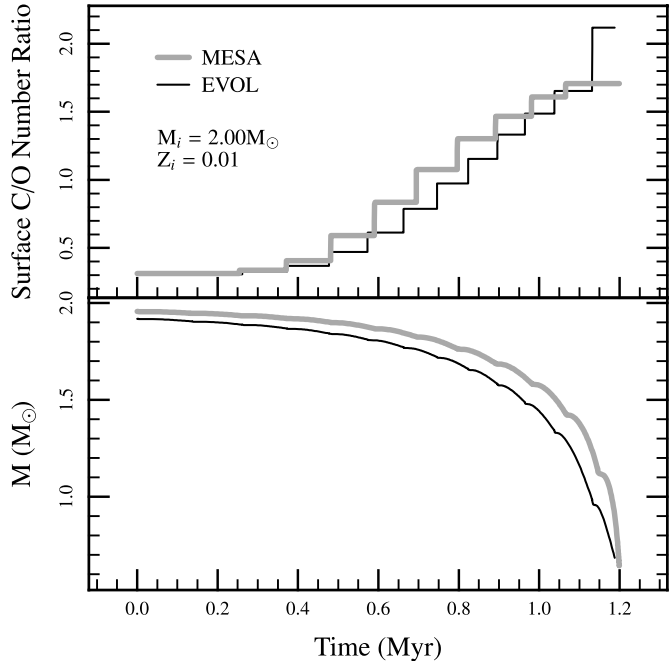


**Figure 27.** C/O number ratio (top panel) and stellar mass,  $M$  (bottom panel) as a function of time from EVOL (solid black line), and MESA star (thick gray line). Time has been set to zero for both tracks at the onset of the third dredge-up.

*Kepler* (Gilliland et al. 2010) satellites is probing the slowly pulsating B stars (SPBs,  $M \approx 3\text{--}8 M_{\odot}$ ) and the more massive ( $M \approx 7\text{--}20 M_{\odot}$ )  $\beta$  Cepheids (Degroote et al. 2009, 2010). These stars are all undergoing main-sequence H burning and are unstably pulsating due to the  $\kappa$  mechanism from the Fe-group opacity bump at  $T \approx 2 \times 10^5$  K (Dziembowski et al. 1993). The observed modes have finite amplitudes deep in the stellar core, demanding a full interior model for mode frequency (and stability) prediction (Dziembowski et al. 1993; Pamyatnykh et al. 2004).

These papers provide a few specific models that allow a direct comparison to the MESA star prediction of the Brunt–Väisälä frequency

$$N^2 = g \left( \frac{1}{\Gamma_1} \frac{d \ln P}{dr} - \frac{d \ln \rho}{dr} \right) = g \left( -\frac{g}{c_s^2} - \frac{d \ln \rho}{dr} \right), \quad (18)$$

where  $c_s^2 = \Gamma_1 P / \rho$  is the adiabatic sound speed, and we used hydrostatic balance,  $dP/dr = -\rho g$ . Numerically, these are obtained by interpolating the sound speed at the cell boundary, whereas  $d \ln \rho/dr$  is estimated by numerical differencing and then smoothed. This method naturally captures the extra restoring force from composition gradients, especially relevant in these evolving stars that leave a He-rich radiative region above the retreating convective core during the main sequence.

Our first comparison is to Dziembowski et al.’s (1993)  $M = 4 M_{\odot}$  main-sequence star with  $Z = 0.02$  at a time when the hydrogen abundance in the convective core is  $X_c = 0.37$ . With no overshoot from the convective core, Dziembowski et al. (1993) found  $\log L/L_{\odot} = 2.51$  and  $\log T_{\text{eff}} = 4.142$  whereas MESA star gives  $\log L/L_{\odot} = 2.50$  and  $\log T_{\text{eff}} = 4.125$ . The top panel in Figure 28 compares the MESA star results (solid line) to the values (green circles) from Figure 3 of Dziembowski et al. (1993). The agreement is remarkable as an integral test of MESA star. The bottom panel of Figure 28 is a comparison to the more massive  $M = 9.858 M_{\odot}$  main-sequence star with

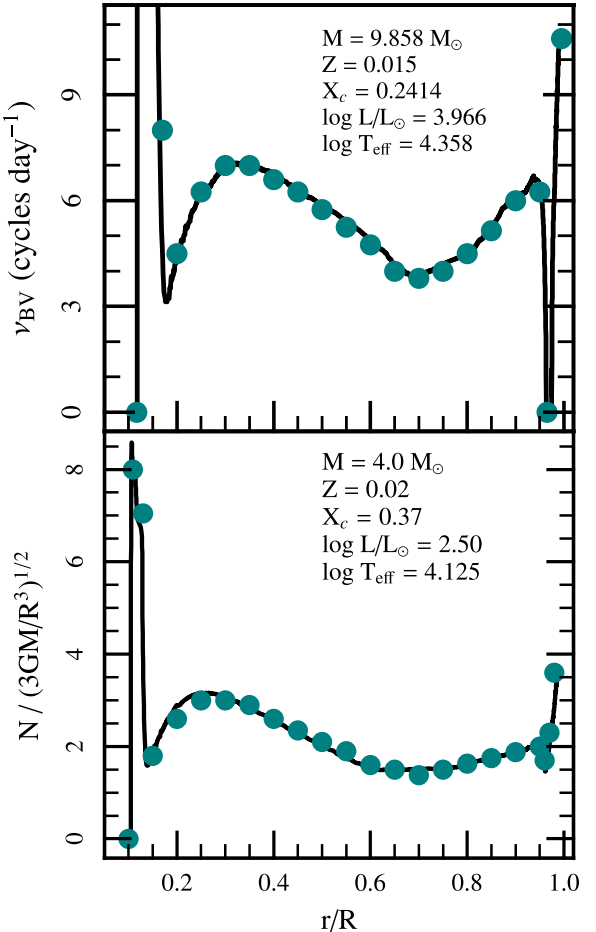


**Figure 28.** Comparison of MESA star predictions of the Brunt–Väisälä frequency,  $N$ , to two cases from the literature; in both cases, the MESA star model is shown as a solid line while the literature values are plotted as filled green circles. Comparisons are made at fixed  $X_c$  for H burning stars. The bottom panel shows a  $4 M_{\odot}$  star from Dziembowski et al. (1993), and the top panel shows an  $M = 9.858 M_{\odot}$  star from Pamyatnykh et al. (2004). In keeping with the way the numbers are presented in these papers, the vertical axes are different in the two panels with the bottom one in dimensionless units of  $N/(3GM/R^3)^{1/2}$  and the top in cycles per day.

(A color version of this figure is available in the online journal.)

$Z = 0.015$  from Figure 5 of Pamyatnykh et al. (2004) at an age (15.7 Myr) when  $X_c = 0.2414$  with  $\log L/L_{\odot} = 3.969$  and  $\log T_{\text{eff}} = 4.3553$ . MESA star gave  $\log L/L_{\odot} = 3.966$ ,  $\log T_{\text{eff}} = 4.358$ , and an age of 16.4 Myr at the same value of  $X_c$ . These comparisons highlight the readiness of MESA star for adiabatic asteroseismological studies of main-sequence stars.

### 7.3. High Mass Stellar Structure and Evolution

To explore MESA star’s results in this mass range, models of  $15 M_{\odot}$ ,  $20 M_{\odot}$ , and  $25 M_{\odot}$  of solar metallicity and  $1000 M_{\odot}$  of zero metallicity were evolved from the Hayashi track to the onset of core collapse. Nuclear reactions are treated with the 21 isotope reaction network, inspired by the 19 isotope network in Weaver et al. (1978), that is capable of efficiently generating accurate nuclear energy generation rates from hydrogen burning through silicon burning (see Section 4.5). This network includes linkages for PP-I, steady-state CNO cycles, a standard  $\alpha$ -chain, heavy ion reactions, and aspects of photodisintegration into  $^{54}\text{Fe}$ . Atmospheres are treated as a  $\tau=2/3$  Eddington gray surface as described in Section 5.3. Mass loss for the solar metallicity stars uses the combined results of Glebbeek et al. (2009), Vink

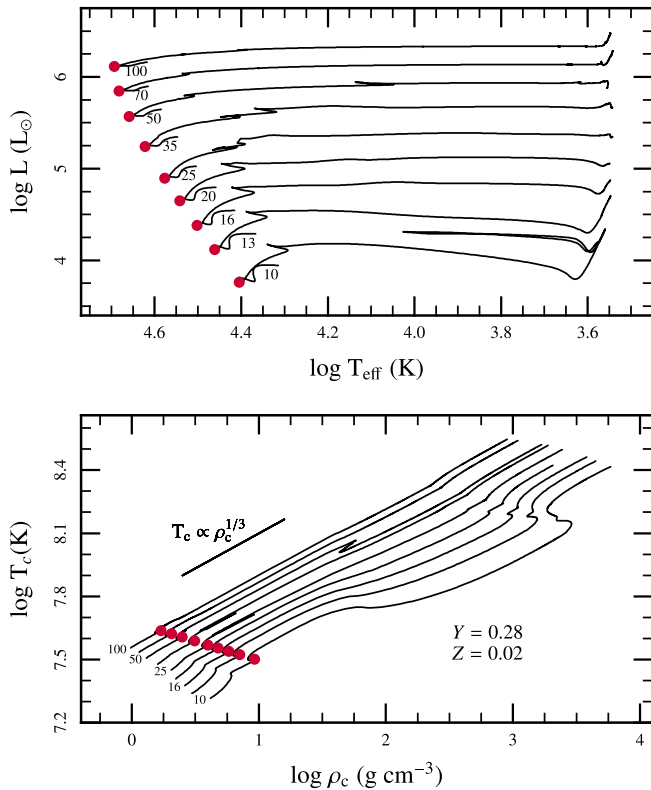


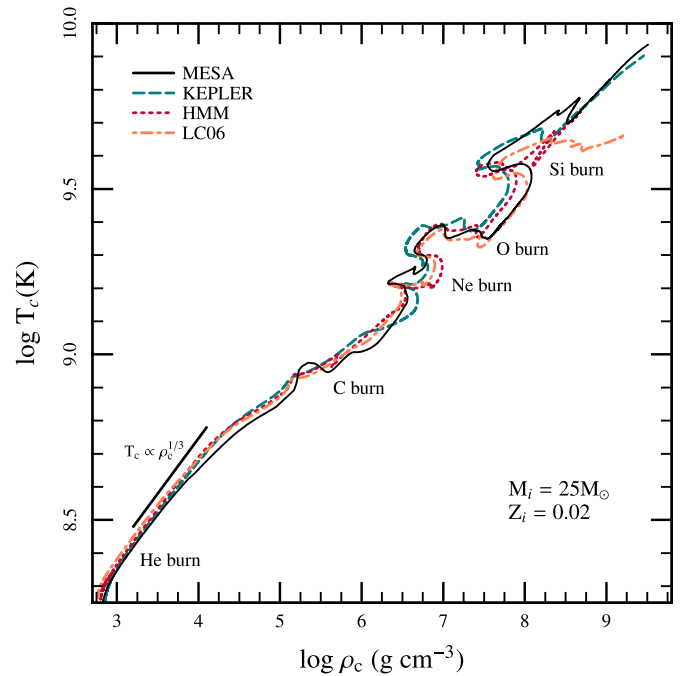
**Figure 29.** Top: H-R diagram for  $10-100 M_\odot$  models from the PMS to the end of core Helium burning for  $Z = 0.02$  but with zero mass loss. Bottom: trajectories of the central conditions in the  $T-\rho$  plane over this same evolutionary period. (A color version of this figure is available in the online journal.)

et al. (2001), Nugis & Lamers (2000), and Nieuwenhuijzen & de Jager (1990), as described in Section 6.6. These massive star models are non-rotating, use no semi-convection, employ a mixing length parameter of  $\alpha_{\text{MLT}} = 1.6$ , and adopt  $f = 0.01$  for exponential diffusive overshoot (see Section 5.2) for convective regions that are either burning hydrogen or are not burning.

Most of this section consists of comparisons to results from other stellar evolution codes. However, for consistency (and completeness), we show in Figure 29 the H-R diagram and central condition evolution of  $10-100 M_\odot$  stars from the PMS to the end of core helium burning. Though these are stars with  $Z = 0.02$ , we turned off mass loss during this calculation so that the plot would be easier to read and of some pedagogical use. The tendency of  $T_c$  to scale with  $\rho_c^{1/3}$  (also a constant radiation entropy) during these stages of evolution is expected from hydrostatic balance with only a mildly changing mean molecular weight. The rest of the calculations in this section included mass loss as described above.

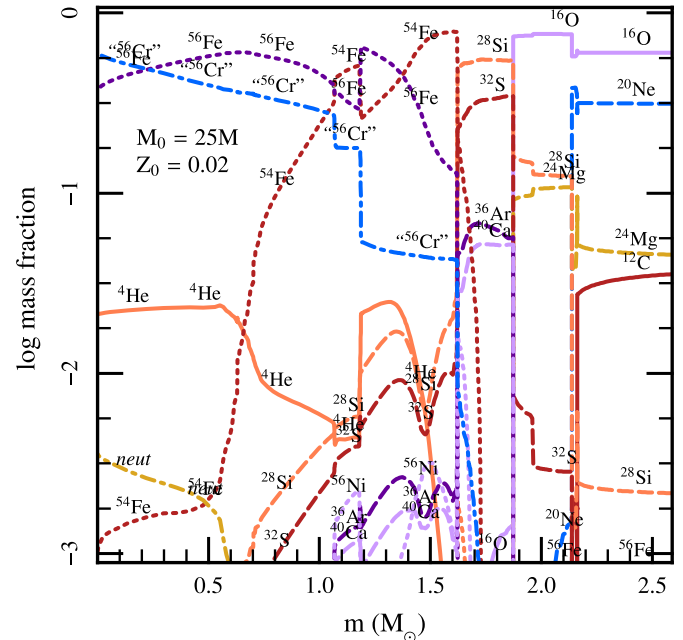
### 7.3.1. $25 M_\odot$ Model Comparisons

Figure 30 shows the  $T_c-\rho_c$  evolution in  $M_i = 25 M_\odot$  solar metallicity models from MESA star, KEPLER (A. Heger 2010, private communication), Hirschi et al. (2004), and FRANEC (Limongi & Chieffi 2006) from helium burning until iron-core collapse. The curves fall below the  $T_c \propto \rho_c^{1/3}$  scaling relation as the mean molecular weight increases due to the subsequent burning stages. The curves are also punctuated with non-monotonic behavior when nuclear fuels are first ignited in shells. Figure 30 shows that MESA star produces core evolutionary tracks consistent with other pre-supernova efforts. The bump in the MESA star curve around carbon burning is



**Figure 30.** Evolution of the central temperature and central density in solar metallicity  $M_i = 25 M_\odot$  models from different stellar evolution codes. The locations of core helium, carbon, neon, oxygen, and silicon burning are labeled, as is the relation  $T_c \propto \rho_c^{1/3}$ .

(A color version of this figure is available in the online journal.)



**Figure 31.** Mass fraction profiles of the inner  $2.5 M_\odot$  of the solar metallicity  $M_i = 25 M_\odot$  model at the onset of core collapse. The reaction network includes links between  $^{54}\text{Fe}$ ,  $^{56}\text{Cr}$ , neutrons, and protons to model aspects of photodisintegration and neutronization.

(A color version of this figure is available in the online journal.)

due to the development of central convection whereas the other codes do not (although see Figure 2 of Limongi et al. 2000). The development of a convective core during carbon burning depends on the carbon abundance left over from core helium burning (Limongi et al. 2000).

The mass fraction profiles of the inner  $2.5 M_\odot$  of this  $M_i = 25 M_\odot$  model are shown in Figure 31 at the onset of core

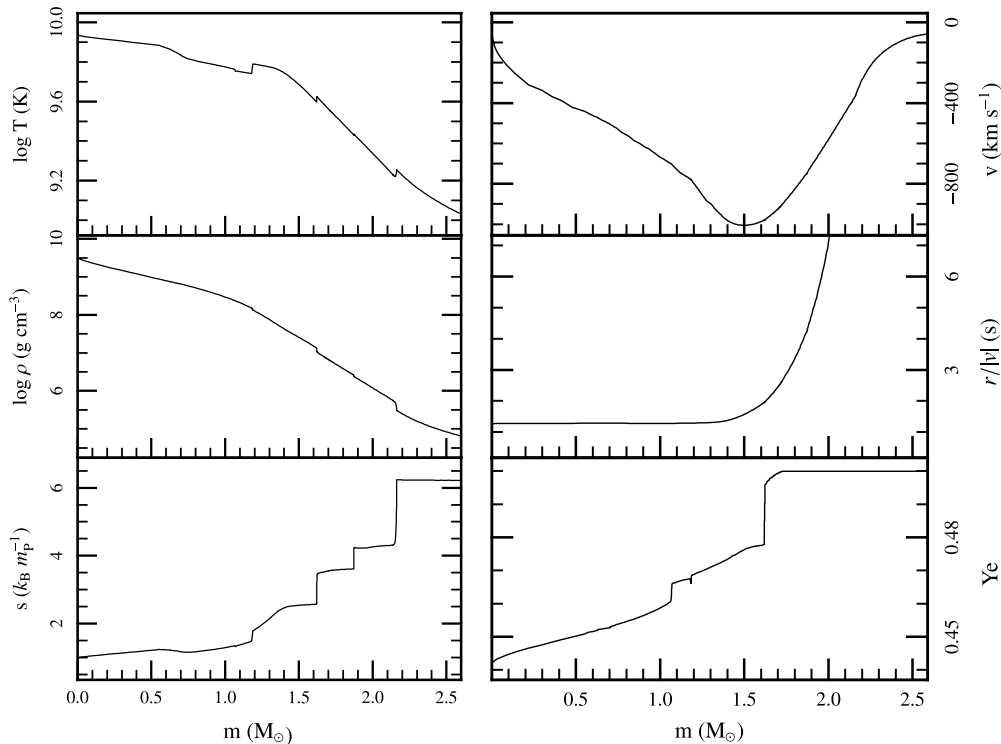


**Figure 32.** Profiles of  $T$  (top left),  $\rho$  (middle left), dimensionless entropy (bottom left), material speed (top right), infall timescale (middle right), and electron fraction  $Y_e = \bar{Z}/\bar{A}$  (bottom right) over the inner  $2.5 M_{\odot}$  of the  $M_i = 25 M_{\odot}$  star at the end of the pre-supernova evolution.

collapse. At the time of these plots, the infall speed has reached  $\approx 1000 \text{ km s}^{-1}$  just inside the iron core (at  $m = 1.5 M_{\odot}$ ) and the electron fraction,  $Y_e$ , has dropped below  $\approx 0.48$ . The oxygen shell lies at  $1.88 \leq m/M_{\odot} \leq 2.5$ , the silicon shell between  $1.61 \leq m/M_{\odot} \leq 1.88$ , and the iron core at  $m \leq 1.61 M_{\odot}$ . Figure 32 shows  $T$ ,  $\rho$ ,  $S$ , the radial velocity, the infall timescale, and  $Y_e$  of this inner  $2.5 M_{\odot}$ . Note the entropy decrements at the oxygen, silicon, and iron core boundaries.

Figure 33 summarizes the history of the inner  $7 M_{\odot}$  of this  $M_i = 25 M_{\odot}$  model as a function of interior mass (left  $y$ -axis). Evolution is measured by the logarithm of time (in years) remaining until the death of the star as a supernova ( $x$ -axis), which reveals the late burning stages. Levels of red and blue shading indicate the magnitude of the net energy generation (nuclear energy generation minus neutrino losses), with red reflecting positive values and blue indicating negative ones. The vertical lines indicate regions that are fully convective. Note the appearance of a convective envelope characteristic of a red supergiant late during helium burning. Abundance profiles of key isotopes during the major burning stages are shown (right  $y$ -axis). The hydrogen core shrinks toward the end of hydrogen burning, and the helium core grows as helium is depleted. The total mass shrinks to about  $M = 12 M_{\odot}$  due to mass loss.

### 7.3.2. Comparison of 15, 20, and $25 M_{\odot}$ Models

Now that we have shown that the  $M_i = 25 M_{\odot}$  MESA star models compare well to previous efforts at the qualitative level, we will make more detailed comparisons to other available results. Table 12 compares the core burning lifetimes of solar metallicity stars with  $M_i = 15, 20$ , and  $25 M_{\odot}$ , from MESA star, Hirschi et al. (2004), Woosley et al. (2002), and Limongi et al. (2000). We define a core burning lifetime to begin when the central mass fraction of fuel has dropped by 0.003 from its maximum value (or onset of central convection) and

**Table 12**  
Massive Star Core Burning Lifetime Comparison

Core Burning	Lifetime (years)				
	Element	HMM	WHW	LSC	MESA
$M_i = 15 M_{\odot}$					
H	1.13	1.11	1.07	1.14	$\times 10^7$
He	1.34	1.97	1.4	1.25	$\times 10^6$
C	3.92	2.03	2.6	4.23	$\times 10^3$
Ne	3.08	0.732	2.00	3.61	
O	2.43	2.58	2.43	4.10	
Si	2.14	5.01	2.14	0.810	$\times 10^{-2}$
$M_i = 20 M_{\odot}$					
H	7.95	8.13	7.48	8.01	$\times 10^6$
He	8.75	11.7	9.3	8.10	$\times 10^5$
C	9.56	9.76	14.5	13.5	$\times 10^3$
Ne	0.193	0.599	1.46	0.916	
O	0.476	1.25	0.72	0.751	
Si	9.52	31.5	3.50	3.32	$\times 10^{-3}$
$M_i = 25 M_{\odot}$					
H	6.55	6.706	5.936	6.38	$\times 10^6$
He	6.85	8.395	6.85	6.30	$\times 10^5$
C	3.17	5.222	9.72	9.07	$\times 10^2$
Ne	0.882	0.891	0.77	0.202	
O	0.318	0.402	0.33	0.402	
Si	3.34	2.01	3.41	3.10	$\times 10^{-3}$

**References.** HMM: Hirschi et al. (2004); WHW: Woosley et al. (2002); LSC: Limongi et al. (2000); MESA: this paper.

to terminate when the central mass fraction has dropped below  $10^{-4}$  (or the end of central convection). Different authors adopt different lifetime definitions, which likely contribute to some of the scatter. The hydrogen burning lifetimes for the  $15 M_{\odot}$ ,  $20 M_{\odot}$ , and  $25 M_{\odot}$  models from the different authors are within

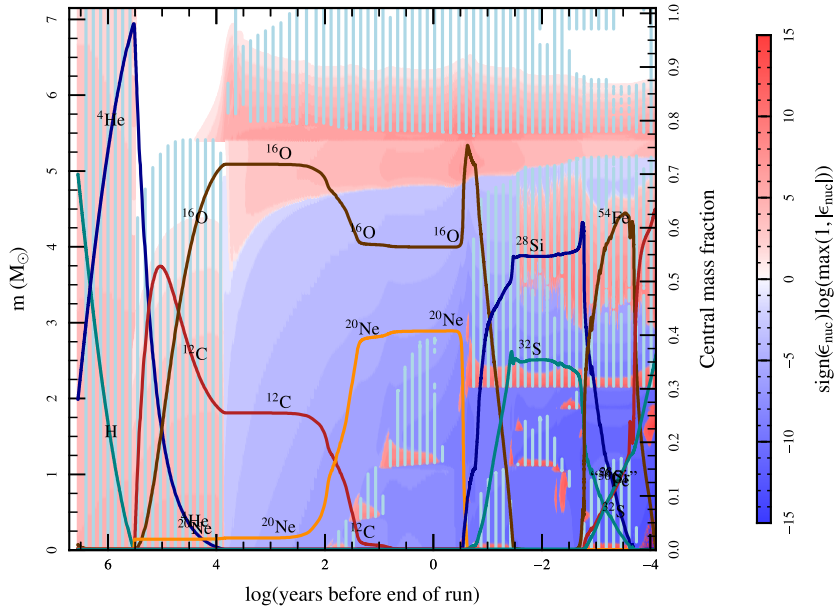


**Figure 33.** Kippenhahn diagram showing the full time evolution of the inner  $7 M_{\odot}$  of the  $M_i = 25 M_{\odot}$  evolutionary sequence from the main sequence to the onset of core collapse. Mass coordinate and abundance mass fraction are labeled on the left and right y-axes, respectively. The shaded bar on the right indicates the net energy generation: red for positive values and blue for negative values. The vertical lines indicate convection.

(A color version of this figure is available in the online journal.)

10% of each other, with the Limongi et al. (2000) models generally having the shortest lifetimes and the Woosley et al. (2002) models having the longest lifetimes. There is more spread in the helium burning lifetimes, with MESA star models showing shorter lifetimes and Woosley et al. (2002) models having the longest lifetimes. The carbon burning lifetimes show agreement within 20% for the  $15 M_{\odot}$  model, but differ by factors of  $\sim 3$  for the  $20 M_{\odot}$  and  $25 M_{\odot}$  models. The neon, oxygen, and silicon burning lifetimes show agreement within 20% between some models, but factor of  $\sim 5$  differences in others. It is beyond the scope of this paper to put the different lifetime definitions on the same footing and explore the reasons for these differences. Nevertheless, Table 12 suggests MESA star produces lifetimes consistent with the range of lifetimes from other works.

Table 13 compares pre-supernova core masses of solar metallicity stars with  $M_i = 15, 20$ , and  $25 M_{\odot}$  models from MESA star, Hirschi et al. (2004), Rauscher et al. (2002), Heger et al. (2000), and Limongi et al. (2000). MESA star core masses are defined as the mass interior to the location where the element mass fraction is 0.5. The definitions used by various authors may differ, contributing to scatter in the results. However, most of the scatter is probably due to the different mass-loss prescriptions used by different authors, resulting in different total masses. The helium yields differ by about 10%, with the Heger et al. (2000) models producing less helium. There is more diversity in the C+O+Ne bulk yields, up to a factor of two for the  $25 M_{\odot}$  model, with the Rauscher et al. (2002) models producing the most and the Heger et al. (2000) models producing the least. Strikingly, the Fe core masses show less variations, with the Hirschi et al. (2004) models producing the heaviest cores. Table 13 suggests MESA star produces bulk yields compatible with previous efforts.

### 7.3.3. $1000 M_{\odot}$ Metal-free Star Capabilities

We close this section with a demonstration of MESA star's capabilities by describing the unlikely scenario of a purely metal-free stellar evolution of an  $M_i = 1000 M_{\odot}$  star. The  $T_c - \rho_c$

**Table 13**  
Pre-supernovae Core Mass Comparisons

Mass ( $M_{\odot}$ )	HMM	RHW	HLW	LSC	MESA
$M_i = 15 M_{\odot}$					
Total	13.232	12.612	13.55	15	12.81
He	4.168	4.163	3.82	4.10	4.37
C+O+Ne	2.302	2.819	1.77	2.39	2.27
“Fe”	1.514	1.452	1.33	1.429	1.510
$M_i = 20 M_{\odot}$					
Total	15.69	14.74	16.31	20	15.50
He	6.21	6.13	5.68	5.94	6.33
C+O+Ne	3.84	4.51	2.31	3.44	3.77
“Fe”	1.75	1.46	1.64	1.52	1.58
$M_i = 25 M_{\odot}$					
Total	16.002	13.079	18.72	25	15.28
He	8.434	8.317	7.86	8.01	8.41
C+O+Ne	5.834	6.498	3.11	4.90	5.49
“Fe”	1.985	1.619	1.36	1.527	1.62

**References.** HMM: Hirschi et al. (2004); RHW: Rauscher et al. (2002); HLW: Heger et al. (2000); LSC: Limongi et al. (2000); MESA: this paper.

trajectory for a  $1000 M_{\odot}$ , zero metallicity, zero mass-loss model is shown in the left panel of Figure 34. The starting time point is in the lower left corner and the final model, at the onset of core collapse, is in the upper right at very high values of  $T_c$  and  $\rho_c$ . Fluid elements in the region to the left of the red dashed line have  $\Gamma_1 < 4/3$ . When the center enters this region, the central portions of the star become dynamically unstable and begin to contract. However, the entire star does not collapse because the infalling regions become denser and hotter, causing the central region to leave the  $\Gamma_1 < 4/3$  region and the infall to slow. Now another part of the star moves into the  $\Gamma_1 < 4/3$  region and begins to infall at high velocity. The net result is that the region where  $\Gamma_1 < 4/3$  starts at the center and moves outward.

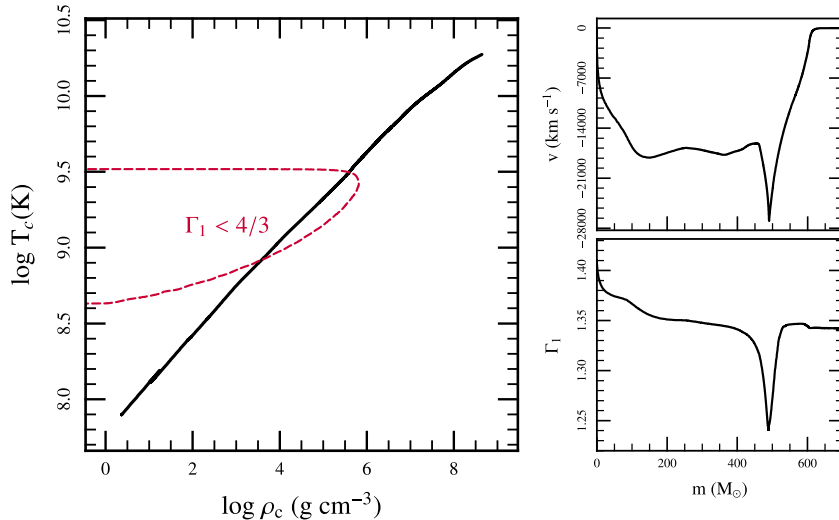


**Figure 34.** Time history (left panel) of  $T_c$  and  $\rho_c$  in a  $1000 M_\odot$ , zero metallicity, zero mass-loss model. Also shown are the boundaries within which  $\Gamma_1 < 4/3$ . Material speed and  $\Gamma_1$  profiles (right panel) for the final model.

(A color version of this figure is available in the online journal.)

The right panel of Figure 34 shows the material speed and  $\Gamma_1$  profiles for the final model, where the infalling region is now at  $m \approx 480 M_\odot$ .

The global history of the  $1000 M_\odot$  model as a function of time is shown in the left panel of Figure 35. A convective envelope appears during late helium burning. Abundance profiles of key isotopes during the major burning stages are shown (right y-axis). Note the short carbon burning era. At late times the core photodisintegrates to  $^4\text{He}$  instead of creating  $^{56}\text{Ni}$  because of the lower central densities encountered in these supermassive progenitors. This also partially causes the large endothermic central regions of the star.

#### 7.4. Stellar Evolution with Mass Transfer

MESA star can be used to examine how a star responds to mass loss or accretion (see Section 6.6). This opens up a large variety of possible applications, including accretion onto white dwarfs for classical novae and thermonuclear supernovae, mass transfer in tight stellar binaries, and learning the response of a star to sudden mass loss. We show two examples where MESA star's results can be compared to previous work. The first is a mass-transfer scenario relevant to  $P_{\text{orb}} < 2$  hr cataclysmic variables, and the second is the response of a neutron star to accretion of pure He.

##### 7.4.1. Mass Transfer in a Binary

To illustrate MESA star's ability to calculate the impact of mass loss on a star, we model the evolution of a compact binary consisting of a Roche Lobe filling low-mass ZAMS ( $M < 0.2 M_\odot$ ) model and an accreting white dwarf with  $M_{\text{WD}} = 0.6 M_\odot$ . These short orbital period ( $P_{\text{orb}} < 2$  hr) cataclysmic variables are the end points of these mass transferring systems (Patterson 1998; Kolb & Baraffe 1999) and are now being discovered in large numbers in the SDSS database (more than 100 studied by Gänsicke et al. 2009).

We model the parameters of the binary system and the Roche lobe overflow triggered mass transfer rate  $M$  as in Madhusudhan et al. (2006). So as to compare to the previous work of Kolb & Baraffe (1999), we presume angular momentum losses from gravitational wave emission and keep the accreting WD mass

**Table 14**  
Mass Transfer History for  $M_i = 0.21 M_\odot$  and  $M_{\text{WD}} = 0.6 M_\odot$

Time (Gyr)	$P_{\text{orb}}$ (hr)	$M/M_\odot$	$T_{\text{eff}}$ (K)	$\log(L/L_\odot)$	$R/R_\odot$	$\log \dot{M}$
0.00	2.1319	0.2100	3278	-2.2688	0.2279	-10.24
0.25	2.0962	0.1987	3262	-2.3041	0.2209	-10.39
0.50	2.0367	0.1887	3242	-2.3467	0.2129	-10.40
0.75	1.9770	0.1787	3217	-2.3939	0.2049	-10.41
1.00	1.9181	0.1693	3191	-2.4414	0.1971	-10.42
1.25	1.8560	0.1599	3167	-2.4904	0.1891	-10.44
1.50	1.7938	0.1510	3142	-2.5404	0.1814	-10.45
1.75	1.7299	0.1421	3113	-2.5952	0.1735	-10.46
2.00	1.6684	0.1336	3074	-2.6563	0.1659	-10.47
2.25	1.6097	0.1252	3018	-2.7277	0.1585	-10.48
2.50	1.5475	0.1170	2965	-2.8004	0.1510	-10.50
2.75	1.4829	0.1093	2916	-2.8737	0.1435	-10.51
3.00	1.4151	0.1016	2854	-2.9590	0.1358	-10.52
3.25	1.3484	0.0942	2774	-3.0577	0.1283	-10.53
3.50	1.2804	0.0868	2666	-3.1796	0.1207	-10.54
3.75	1.2172	0.0796	2525	-3.3273	0.1135	-10.54
4.00	1.1663	0.0726	2355	-3.4987	0.1071	-10.55
4.25	1.1345	0.0659	2161	-3.6915	0.1019	-10.58
4.50	1.1227	0.0596	1963	-3.8930	0.0980	-10.63
4.75	1.1291	0.0541	1771	-4.0949	0.0953	-10.70
5.00	1.1487	0.0495	1595	-4.2924	0.0937	-10.78
5.25	1.1752	0.0457	1445	-4.4725	0.0927	-10.86
5.50	1.2051	0.0426	1314	-4.6436	0.0922	-10.94
5.75	1.2379	0.0399	1201	-4.8016	0.0919	-11.02
6.00	1.2706	0.0377	1110	-4.9398	0.0918	-11.09
6.25	1.3035	0.0358	1028	-5.0720	0.0918	-11.16
6.50	1.3343	0.0343	969	-5.1749	0.0919	-11.22
6.75	1.3636	0.0328	921	-5.2630	0.0920	-11.29
7.00	1.3902	0.0316	879	-5.3425	0.0921	-11.34

fixed at its initial value,  $M_{\text{WD}} = 0.6 M_\odot$ . The evolution of the donor star is carried out by MESA star, using the  $\tau = 100$  atmosphere tables from atm. The evolution shown in Figure 36 is followed for over 6 Gyr until the donor has been reduced to a brown dwarf remnant of  $M \approx 0.03 M_\odot$  (see Table 14). During that time, the binary period drops to a minimum value of 67.4 minutes and then increases, independent of the initial donor mass. This plot is very similar to Figure 1 of Kolb & Baraffe (1999). We also show in Table 14 the evolution in time

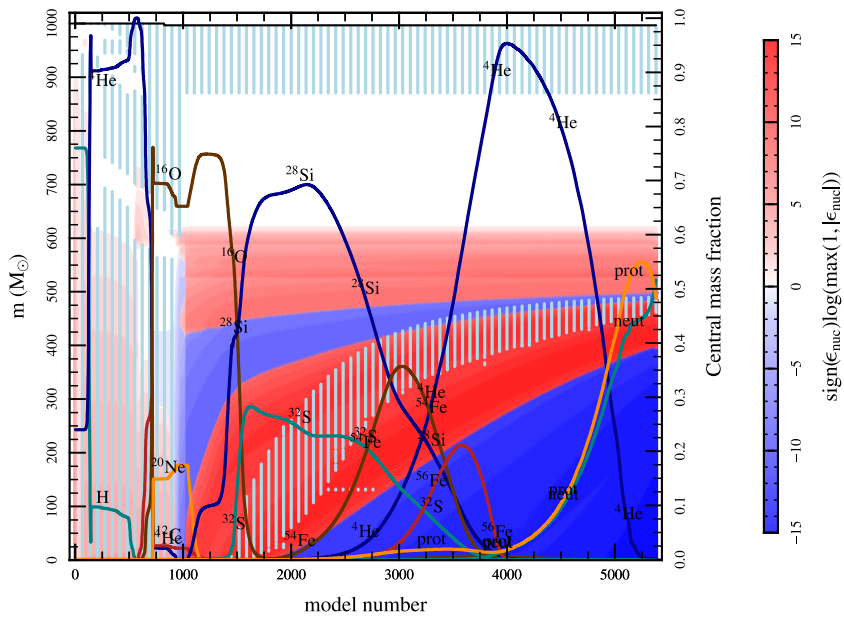


**Figure 35.** Kippenhahn diagram showing the evolution of the  $1000 M_{\odot}$  model. The format is the same as Figure 33.

(A color version of this figure is available in the online journal.)

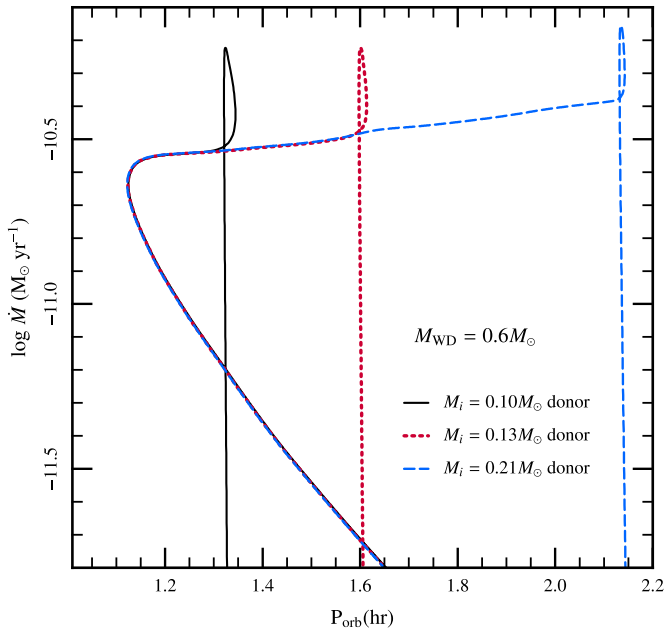


**Figure 36.** Mass transfer rate for cataclysmic variables with low-mass main-sequence donor stars of varying initial masses  $M_i$ . Each line shows the  $\dot{M}$  history for different initial mass donors, all accreting onto a  $M_{WD} = 0.6 M_{\odot}$  white dwarf. After a period of initial adjustment to the mass transfer, each track tends to the same trajectory, showing the orbital period minimum at  $P_{\text{orb}} = 67.4$  minutes.

(A color version of this figure is available in the online journal.)

of the main properties of the donor star and mass transfer rate of the  $M_i = 0.21 M_{\odot}$  model. Again, this agrees with the results in Table 2 of Kolb & Baraffe (1999). The prime differences can be attributed to a slightly different  $R(M)$  relation.

#### 7.4.2. Rapid Helium Accretion onto a Neutron Star

The outer envelope of an accreting neutron star is modeled in MESA star by using non-zero boundary conditions  $M_c$  and  $L_c$  (see discussion in Section 6.2) at a finite radius  $R_c$ . This allows for a time-dependent calculation of the thermonuclear instability

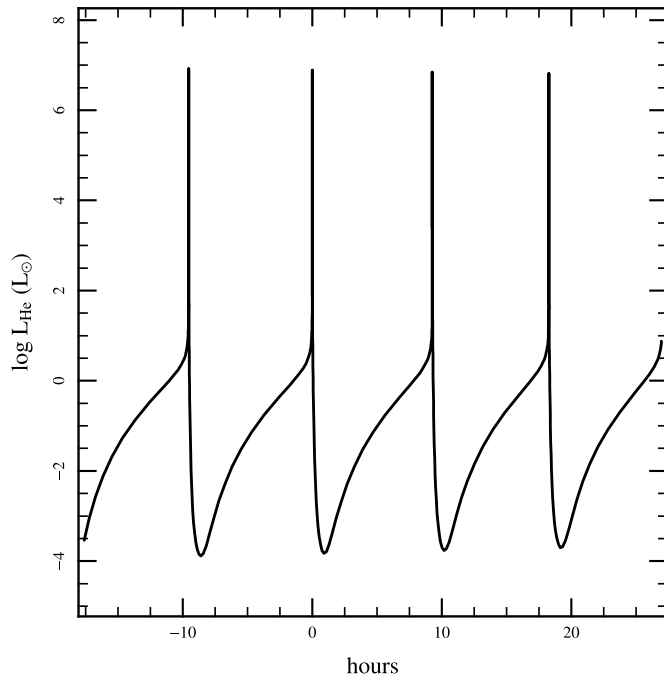
that yields Type I X-ray bursts (Strohmayer & Bildsten 2006) for those accretion rates where the burning is thermally unstable ( $\dot{M} \leq 10^{-8} M_{\odot} \text{ yr}^{-1}$ ). Such calculations have been performed with the KEPLER code (Woosley et al. 2004; Cyburt et al. 2010) and prove very valuable in direct comparisons to observed Type I X-ray burst recurrence times and light curves, especially for the H-rich accreting “clocked burster” GS 1826-24 (Heger et al. 2007). We focus here on pure He accretion, relevant to neutron stars in ultra-compact binaries, such as 4U 1820-30 (Cumming 2003).

For these simulations we set  $M_c = 1.4 M_{\odot}$ ,  $R_c = 10 \text{ km}$ ,  $L_c = 3.6 \times 10^{34} \text{ erg s}^{-1}$ , and  $g = 2.39 \times 10^{14} \text{ cm s}^{-2}$  (correcting for the gravitational redshift). The initial model consisted of  $3 \times 10^{25} \text{ g}$  of pure  $^{56}\text{Fe}$  and accreted pure He at  $\dot{M} = 3 \times 10^{-9} M_{\odot} \text{ yr}^{-1}$ . We require a slightly higher value of core luminosity  $L_c/\dot{M} \approx 0.19 \text{ keV nucleon}^{-1}$  to reach the same ignition column depth ( $5 \times 10^8 \text{ g cm}^{-2}$ ) as Weinberg et al. (2006). We used 31 species in the nuclear reaction network, including the  $^{12}\text{C}$  bypass reaction chain  $^{12}\text{C}(p,\gamma)^{13}\text{N}(\alpha,p)^{16}\text{O}$  and elements ( $^{23}\text{Na}$ ,  $^{27}\text{Al}$ ,  $^{31}\text{P}$ ,  $^{35}\text{Cl}$ , and  $^{39}\text{K}$ ) that can appear as intermediates in  $(\alpha, p)(p, \gamma)$  reactions and serve as the proton source for the  $^{12}\text{C}$  bypass (Weinberg et al. 2006).

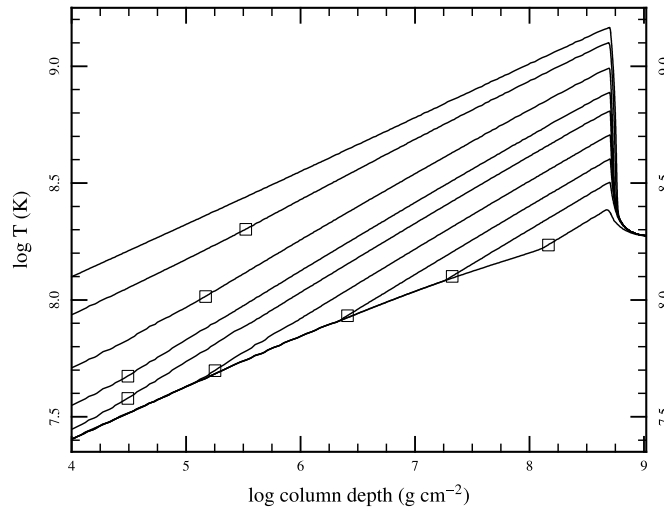
Figure 37 shows a snapshot of the time history of the helium burning luminosity,  $L_{\text{He}}$ , which is periodic at the Type I burst recurrence time of 9.56 hr. This luminosity, as well as  $L$ , very quickly exceeds  $L_{\text{Edd}}$ , in which case we allow for mass loss via a wind (Paczynski & Proszynski 1986). We arbitrarily set our time coordinate to zero at the time of maximum luminosity,  $L$ , in the second burst after the start of accretion. The peak for  $L_{\text{He}}$  is at  $t = -0.0269 \text{ s}$ , and  $L > L_{\text{Edd}}$  for the time interval  $-0.0047 \text{ s} < t < 1.2169 \text{ s}$ .<sup>30</sup>

Figure 38 shows the evolving temperature profile during the convective burning runaway, where time increases upward. Though not for the same ignition depth, this plot is very similar to Figure 2 of Weinberg et al. (2006), including the evolution of the location of the top of the convective zone (open squares).

<sup>30</sup> A movie of this flash (made with PGstar, see Section 6.9) is at <http://mesa.sourceforge.net/pdfs/nshe.mov>



**Figure 37.** Helium-burning luminosity,  $L_{\text{He}}$ , as a function of time for a neutron star of mass  $M_c = 1.4 M_{\odot}$  and radius  $R_c = 10$  km accreting pure helium at  $\dot{M} = 3 \times 10^{-9} M_{\odot} \text{ yr}^{-1}$ . The Type I X-ray bursts occur every 9.56 hr.



**Figure 38.** Evolving temperature profile during the convective burning phase of a Type I burst, as a function of column depth,  $P/g$ . Starting from the bottom, each successive solid line is the temperature profile at a later time. The open squares mark the location of the top of the convective zone. The top curve is at  $t = -0.00716$ .

Weinberg et al. (2006) discussed in detail the onset of heat transport in the outer, thin, radiative layer that allows for the retreat of the top of the convective zone. This MESA star result is the first numerical confirmation of this transition for a pure helium accretor and demonstrates our ability to obtain excellent time and mass resolution as shown in Figure 39. By using nonzero center boundary conditions so that the  $dq$  variables (see Section 6.6) cover only the relatively small envelope mass, we reach a mass resolution of  $\approx 1.5 \times 10^{-20} M_{\odot}$ . The timestep adjustment algorithms (Section 6.4) provide a smooth change from timesteps of almost an hour between bursts down to millisecond steps at peak luminosity (see the middle panel in Figure 39). The secular increase in the number of cells is to track the accumulation of the pile of ashes from each burst. The

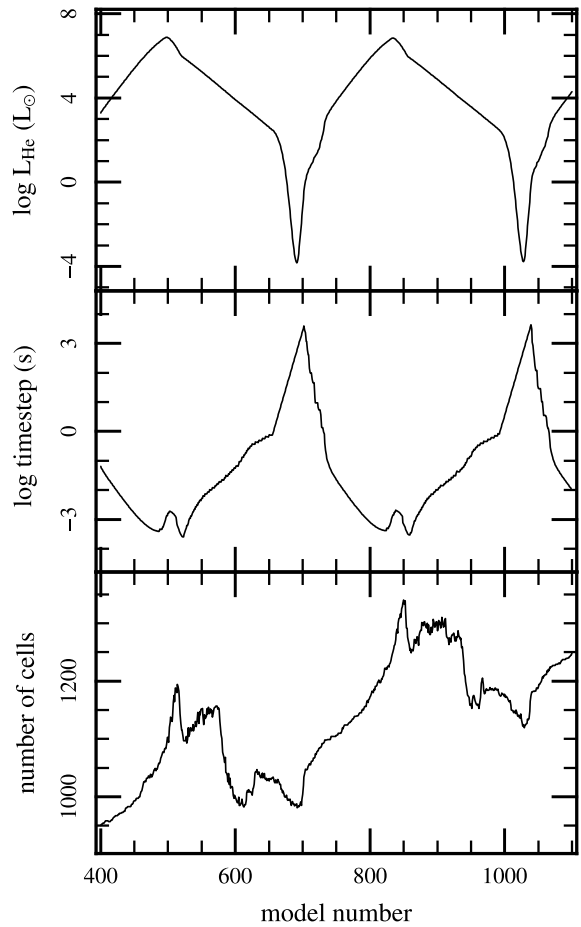


**Figure 39.** He-burning luminosity, timestep, and number of cells as a function of model number for the MESA star simulation of an accreting neutron star. The timestep ranges from a millisecond to an hour, whereas the number of cells only grows by  $\approx 25\%$  during the burst and shows a secular trend upward as partially burned material accumulates.

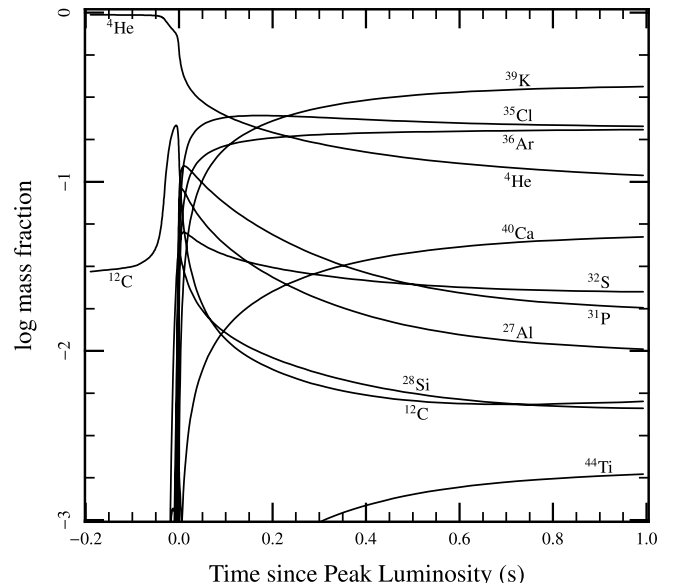


**Figure 40.** Abundances of the dominant isotopes at the base of the convective zone as a function of time during the Type I burst. The temperature at the base of the convective zone at  $t = 1$  s is  $\log T = 9.15$ .

evolution of abundances at the base of the convective zone is shown in Figure 40 and exhibits the presence of the isotopes  $^{35}\text{Cl}$  and  $^{39}\text{K}$ .

We have performed simulations at lower accretion rates but these become dynamical events where the temperature rises on a local dynamical timescale and are beyond the present scope of MESA star. While multi-dimensional hydrodynamical codes (e.g., Zingale et al. 2009) may be needed to follow the details of such an event, MESA star can be used for studying the longer timescale, hydrostatic evolution leading up to the point where hydrodynamic effects become dominant.

## 8. SUMMARY AND CONCLUSION

MESA provides open source, portable, robust, efficient, thread-safe libraries for stellar astrophysics and stellar evolution. It provides tools for a broad community of astrophysicists to explore a wide range of stellar masses and metallicities. State-of-the-art modules include the EOS, opacity, nuclear reaction rates and networks, atmosphere boundary conditions, and element diffusion. MESA features a modern code architecture and runtime environment.

MESA star solves the fully coupled structure and composition equations simultaneously and is capable of calculating full evolutionary tracks without user intervention. It implements adaptive mesh refinement, sophisticated timestep adjustment, mass loss and accretion, and parallelism based on OpenMP.

MESA is subjected to an ongoing testing and verification process. Current capabilities include evolutionary tracks of very low mass stellar objects and gas giant planets, intermediate-mass stars, pulsating stars, accreting compact objects, and massive stars from the PMS to late times. Future versions of MESA will include the addition of a variety of new physics modules, features driven by the MESA user community, and architectural refinements.

We thank Edward Brown and Mike Zingale for carefully reading the manuscript and providing cogent criticisms and clarifications. MESA has benefited from personal communications with many people including, but not limited to, the following: France Allard, Leandro Althaus, Dave Arnett, Phil Arras, Isabelle Baraffe, Arnold Boothroyd, Adam Burgasser, Adam Burrows, Jeff Cash, Brian Chaboyer, Philip Chang, Alessandro Chieffi, Joergen Christensen-Dalsgaard, Chris Deloye, Pavel Denisenkov, Peter Eggleton, J. J. Eldridge, Jason Ferguson, Jonathan Fortney, Michael Gehmeyr, Evert Glebbeek, Ernst Haierer, Francois Hebert, Alexander Heger, Lynne Hillenbrand, Raphael Hirschi, Piet Hut, Alan Irwin, Thomas Janka, Stephen Justham, David Kaplan, Max Katz, Attay Kovetz, Michael Lederer, Marco Limongi, Jinrong Lin, Marcin Mackiewicz, Georgios Magkotsios, Lars Mattsson, Dan Meiron, Michael Montgomery, Ehsan Moravveji, Lorne Nelson, Marco Pignatari, Marc Pinsonneault, Philip Pinto, Phillip Podsiadlowski, Onno Pols, Alexander Potekhin, Saul Rappaport, Yousef Saad, Didier Saumon, Helmut Schlattl, Aldo Serenelli, Ken Shen, Steinn Sigurdsson, Dave Spiegel, Richard Stancilffe, Sumner Starfield, Justin Steinfadt, Peter Teuben, Jonathan Tomshine, Dean Townsley, Don VandenBerg, Roni Waldman, Yan Wang, Nevin Weinberg, and Ofer Yaron. This work was supported by the National Science Foundation under grants PHY 05-51164 and AST 07-07633. A.D. acknowledges support from a CITA National Fellowship. F.H. is supported by an NSERC Discovery Grant. F.X.T. acknowledges support from the National Science Foundation, grants AST 08-07567 and AST 08-06720, and NASA grant NNX09AD106.

## APPENDIX A MANIFESTO

MESA was developed through the concerted efforts of the lead author over a six year period with the engagement and deep involvement of many theoretical and computational astrophysicists. The public availability of MESA will serve education, scientific research, and outreach. This appendix describes the scientific motivation for MESA, the philosophy and rules of use for MESA, and the path forward on stewardship of MESA, and advanced development of future research and education tools. We make MESA openly available with the hope that it will grow into a community resource. We therefore consider it important to explain the guiding principles for using and contributing to MESA. Our goal is to assure the greatest usefulness for the largest number of research and educational projects.

### A.1. Motivation for a New Tool

Stellar evolution calculations (i.e., stellar evolution tracks and detailed information about the evolution of internal and global properties) are a basic tool that enable a broad range of research in astrophysics. Areas that critically depend on high-fidelity and modern stellar evolution include asteroseismology, nuclear astrophysics, galactic chemical evolution and population synthesis, compact objects, supernovae, stellar populations, stellar hydrodynamics, and stellar activity. New observational capabilities are emerging in these fields that place a high demand on exploration of stellar dependencies on metallicity and age. So, even though one-dimensional stellar evolution is a mature discipline, we continue to ask new questions of stars. The emergence of demand requires the construction of a general, modern stellar evolution code that combines the following advantages.

1. **Openness:** should be open to any researcher, both to advance the pace of scientific discovery, but also to share the load of updating physics, fine-tuning, and further development.
2. **Modularity:** should provide independent, reusable modules.
3. **Wide applicability:** should be capable of calculating the evolution of stars in a wide range of environments, including low and massive stars, binaries, accreting, mass-losing stars, early and advanced phases of evolution etc. This will enable multi-problem, multi-object physics validation.
4. **Modern techniques:** should employ modern numerical approaches, including high-order interpolation schemes, advanced AMR, simultaneous operator solution; should support well-defined interfaces for related applications, e.g., atmospheres, wind simulations, nucleosynthesis simulations, and hydrodynamics.
5. **Microphysics:** should allow for up-to-date, wide-ranging, flexible, and modular micro-physics.
6. **Performance:** should parallelize on present and future shared-memory, multi-core/thread and possibly hybrid architectures so that performance continues to grow within the new computational paradigm.

A tool that combines the above features is a significant research and education resource for stellar astrophysics. We acknowledge that some important aspects of stars are truly three dimensional, such as convection, rotation, and magnetism. Those applications remain in the realm of research frontiers with evolving understanding and insights, quite often profound. However, much remains to be gained scientifically (and pedagogically) by accurate one-dimensional calculations, and this is the present focus of MESA.

## A.2. MESA Philosophy

The MESA code library project is open. It explicitly invites participation from anybody (researchers, students, interested amateurs). Participation in MESA can take a wide range of forms, from just using a MESA release for a science project, to testing and debugging (i.e., report bugs, find fixes and submit them for inclusion into the next release) as well as taking on responsibility for the continued stewardship of certain aspects (modules) of the code. The participation of experienced stellar evolution experts is very welcome.

Users are encouraged to add to the capabilities of MESA, which will remain a community resource. However, use of MESA requires adherence to the “MESA code of conduct”.

1. That all publications and presentations (research, educational, or outreach) deriving from the use of MESA acknowledge this paper and the MESA Web site.
2. That user modifications and additions are given back to the community.
3. That users alert the MESA Council (see below) about their publications, either pre-release or at the time of publication.
4. That users make available in a timely fashion (e.g., online at the MESA Web site) all information needed for others to recreate their MESA results—“open know how” to match “open source.”
5. That users agree to help others learn MESA, giving back as the project progresses.

Users are requested to identify themselves by name, email contact, and home location.

## A.3. Establishment of the MESA Council

The MESA project began as an initiative to construct a reliable computational tool for stellar structure and evolution that takes full advantage of modern processor architectures, algorithms, and community engagement. The release of MESA has forced some explicit thinking of what structure is needed so as to achieve the mission of stewarding MESA in its use for scientific research, education, and outreach, while also enabling the development of new tools and ideas. The MESA operating principles are simple: be open in your scientific discussions, give credit to all contributors, and be prepared to give back to the community of users. We hope that this creates an environment where the young are encouraged to become engaged in a career-enhancing manner.

We have established the MESA Council that consists of those engaged in working toward the shared missions outlined here:

1. **Steward MESA.** There are many ways, this will be done: supporting the contributors, maintaining the Web access and Web site updates, seeking enabling funding, holding yearly working groups that allow for continued engagement, documenting MESA development in the peer-reviewed literature, and sustaining advanced development.
2. **Interface with the user community.** This starts with answering questions from users, developing a way to accept new code in an integrated fashion, maintain a user registry, and identify new MESA Council members from those most active and engaged in the intelligent use of MESA.
3. **Enable scientific research and education with MESA.** Promote MESA and its goals, e.g., through scientific contributions at relevant conferences. Identify science opportunities that match MESA capabilities and facilitate and encourage appropriate collaborative activities. Track the science carried out by the community with MESA.

## APPENDIX B

### CODE TESTING AND VERIFICATION

An important part of the ongoing development of a large, complex software project, such as MESA, is regular, systematic testing. Testing is necessary to ensure that MESA continues to function as expected and that the addition of new features does not have unintended consequences for existing features.

MESA is tested at the module level each time it is compiled from the install scripts. These tests check that each module produces results that are consistent with expectations. The next level is the MESA star test suite, which consists of various evolutionary cases that are intended to cover a broad range of applications, including Roche lobe overflow, the He core flash in a low-mass star, the evolution of sub-stellar mass objects, advanced nuclear burning in massive stars, accreting white dwarfs and neutron star envelopes, and more are being added all the time. The test cases come in both short and long varieties. Run in serial, the full set of short tests completes in less than 1 hr on modern hardware. The long tests might each take one or several hours to complete. Many of the evolutionary sequences presented in Section 7 are included in the test suite. Short tests include the very low mass models evolved to 10 Gyr (Figure 18) and the  $0.8 M_{\odot}$ ,  $Z = 10^{-4}$  track (Figures 19), while longer tests include the solar model calibration (Figure 21), the “hands off”  $1 M_{\odot}$  PMS to white dwarf calculation (Figure 13), and Si-burning in a  $15 M_{\odot}$ ,  $Z = 0.02$  model (Tables 12 and 13).

The test suite is readily extended in order to ensure regular testing of certain aspects of MESA that are not covered by the existing set but are important for a particular avenue of research. A template is provided to encourage the creation of new test cases.

## REFERENCES

- Akima, H. 1996, *ACM Algorithm 760, ACM Trans. Math. Software*, 22, 357  
 Alastuey, A., & Jancovici, B. 1978, *ApJ*, 226, 1034  
 Alexander, D. R., & Ferguson, J. W. 1994, *ApJ*, 437, 879  
 Allard, F., Hauschildt, P. H., Alexander, D. R., Tamanai, A., & Schweitzer, A. 2001, *ApJ*, 556, 357  
 Anders, E., & Grevesse, N. 1989, *Geochim. Cosmochim. Acta*, 53, 197  
 Angulo, C., et al. 1999, *Nucl. Phys. A*, 656, 3  
 Arnett, D. 1996, Supernovae and Nucleosynthesis (Princeton, NJ: Princeton Univ. Press)  
 Asplund, M., Grevesse, N., & Sauval, A. J. 2005, in ASP Conf. Ser. 336, Cosmic Abundances as Records of Stellar Evolution and Nucleosynthesis, ed. T. G. Barnes, III & F. N. Bash (San Francisco, CA: ASP), 25  
 Bahcall, J. N. 1997, *Phys. Rev. C*, 56, 3391  
 Bahcall, J. N. 2002, *Phys. Rev. C*, 65, 025801  
 Bahcall, J. N., Basu, S., & Pinsonneault, M. H. 1998, *Phys. Lett. B*, 433, 1  
 Bahcall, J. N., Basu, S., Pinsonneault, M. H., & Serenelli, A. 2005, *ApJ*, 618, 1049  
 Baraffe, I., Chabrier, G., Allard, F., & Hauschildt, P. H. 1998, *A&A*, 337, 403  
 Baraffe, I., Chabrier, G., Barman, T. S., Allard, F., & Hauschildt, P. H. 2003, *A&A*, 402, 701  
 Basu, S., & Antia, H. M. 2008, *Phys. Rep.*, 457, 217  
 Bildsten, L., Brown, E. F., Matzner, C. D., & Ushomirsky, G. 1997, *ApJ*, 482, 442  
 Bjork, S. R., & Chaboyer, B. 2006, *ApJ*, 641, 1102  
 Blöcker, T. 1995, *A&A*, 297, 727  
 Böhm-Vitense, E. 1958, *Z. Astrophys.*, 46, 108  
 Buchler, J. R., & Yueh, W. R. 1976, *ApJ*, 210, 440  
 Burbridge, E. M., Burbridge, G. R., Fowler, W. A., & Hoyle, F. 1957, *Rev. Mod. Phys.*, 29, 547  
 Burrows, A., Hubbard, W. B., & Lunine, J. I. 1989, *ApJ*, 345, 939  
 Burrows, A., Hubbard, W. B., Lunine, J. I., & Liebert, J. 2001, *Rev. Mod. Phys.*, 73, 719  
 Burrows, A., et al. 1997, *ApJ*, 491, 856  
 Calder, A. C., et al. 2002, *ApJS*, 143, 201

- Calder, A. C., et al. 2004, *Comput. Sci. Eng.*, 10, 6
- Cameron, A. G. W. 1957, Chalk River Laboratory Report CRL41 (Chalk River: Atomic Energy of Canada, Ltd.)
- Cassisi, S., Poteckhin, A. Y., Pietrinferni, A., Catelan, M., & Salaris, M. 2007, *ApJ*, 661, 1094
- Castelli, F., & Kurucz, R. L. 2003, in IAU Symp. 210, Modelling of Stellar Atmospheres, ed. N. Piskunov, W. W. Weiss, & D. F. Gray (San Francisco, CA: ASP), A20
- Caughlan, G. R., & Fowler, W. A. 1988, *At. Data Nucl. Data Tables*, 40, 283
- Chabrier, G., & Baraffe, I. 2000, *ARA&A*, 38, 337
- Chabrier, G., Baraffe, I., Allard, F., & Hauschildt, P. 2000, *ApJ*, 542, L119
- Chabrier, G., Baraffe, I., & Plez, B. 1996, *ApJ*, 459, L91
- Chandrasekhar, S. 1939, An Introduction to the Study of Stellar Structure (Chicago, IL: Univ. Chicago Press)
- Christensen-Dalsgaard, J. 2008, *Ap&SS*, 316, 13
- Clayton, D. D. 1984, Principles of Stellar Evolution and Nucleosynthesis (Chicago, IL: Univ. Chicago Press)
- Coelho, P., Bruzual, G., Charlot, S., Weiss, A., Barbuy, B., & Ferguson, J. W. 2007, *MNRAS*, 382, 498
- Cox, J. P., & Giuli, R. T. 1968, Principles of Stellar Structure (New York: Gordon & Breach)
- Cumming, A. 2003, *ApJ*, 595, 1077
- Cyburt, R. H., et al. 2010, *ApJS*, 189, 240
- D'Antona, F., & Mazzitelli, I. 1994, *ApJS*, 90, 467
- Degl'Innocenti, S., Prada Moroni, P. G., Marconi, M., & Ruoppo, A. 2008, *Ap&SS*, 316, 25
- Degroote, P., et al. 2009, *A&A*, 506, 471
- Degroote, P., et al. 2010, *Nature*, 464, 259
- de Jager, C., Nieuwenhuijzen, H., & van der Hucht, K. A. 1988, *A&AS*, 72, 259
- Demarque, P., Guenther, D. B., Li, L. H., Mazumdar, A., & Straka, C. W. 2008, *Ap&SS*, 316, 31
- Dewitt, H. E., Graboske, H. C., & Cooper, M. S. 1973, *ApJ*, 181, 439
- Dotter, A., Chaboyer, B., Jevremović, D., Baron, E., Ferguson, J. W., Sarajedini, A., & Anderson, J. 2007, *AJ*, 134, 376
- Dotter, A., et al. 2010, *ApJ*, 708, 698
- Dziembowski, W. A., Moskalik, P., & Pamyatnykh, A. A. 1993, *MNRAS*, 265, 588
- Eddington, A. S. 1926, Internal Constitution of the Stars (Cambridge: Cambridge Univ. Press)
- Eggenberger, P., Meynet, G., Maeder, A., Hirschi, R., Charbonnel, C., Talon, S., & Ekström, S. 2008, *Ap&SS*, 316, 43
- Egginton, P. P. 1971, *MNRAS*, 151, 351
- Ferguson, J. W., Alexander, D. R., Allard, F., Barman, T., Bodnarik, J. G., Hauschildt, P. H., Heffner-Wong, A., & Tamanai, A. 2005, *ApJ*, 623, 585
- Fujimoto, M. Y., Ikeda, Y., & Iben, I., Jr. 2000, *ApJ*, 529, L25
- Fuller, G. M., Fowler, W. A., & Newman, M. J. 1985, *ApJ*, 293, 1
- Fynbo, H. O. U., et al. 2005, *Nature*, 433, 136
- Gänsicke, B. T., et al. 2009, *MNRAS*, 397, 2170
- Gehmeyr, M., & Mihalas, D. 1994, *Physica D*, 77, 320
- Gilliland, R. L., et al. 2010, *PASP*, 122, 131
- Glebbeek, E., Gaburov, E., de Mink, S. E., Pols, O. R., & Portegies Zwart, S. F. 2002, *A&A*, 497, 255
- Görres, J., Arlandini, C., Giesen, U., Heil, M., Käppeler, F., Leiste, H., Stech, E., & Wiescher, M. 2000, *Phys. Rev. C*, 62, 055801
- Gorshkov, A. B., & Baturin, V. A. 2008, *Astron. Rep.*, 52, 760
- Graboske, H. C., Dewitt, H. E., Grossman, A. S., & Cooper, M. S. 1973, *ApJ*, 181, 457
- Grevessen, N., & Noels, A. 1993, *Phys. Scr. T*, 47, 133
- Grevessen, N., & Sauval, A. J. 1998, *Space Sci. Rev.*, 85, 161
- Hairer, E., & Wanner, G. 1996, Solving Ordinary Differential Equations. II. Stiff and Differential-Algebraic Problems (2nd ed.; Berlin: Springer)
- Hansen, C. J., & Kawaler, S. D. 1995, Stellar Interiors: Physical Principles, Structure, and Evolution (New York: Springer-Verlag)
- Hauschildt, P. H., Allard, F., & Baron, E. 1999a, *ApJ*, 512, 377
- Hauschildt, P. H., Allard, F., Ferguson, J., Baron, E., & Alexander, D. 1999b, *ApJ*, 525, 871
- Heger, A., Cumming, A., Galloway, D. K., & Woosley, S. E. 2007, *ApJ*, 671, L141
- Heger, A., Langer, N., & Woosley, S. E. 2000, *ApJ*, 528, 368 (HLW)
- Heney, L. G., Forbes, J. E., & Gould, N. L. 1964, *ApJ*, 139, 306
- Heney, L. G., Vardya, M. S., & Bodenheimer, P. 1965, *ApJ*, 142, 841
- Heney, L. G., Wilets, L., Bohm, K. H., LeLevier, R., & Levee, R. D. 1959, *ApJ*, 129, 628
- Herwig, F. 2000, *A&A*, 360, 952
- Herwig, F. 2004, *ApJ*, 605, 425
- Herwig, F. 2005, *ARA&A*, 43, 435
- Herwig, F., & Austin, S. M. 2004, *ApJ*, 613, 73
- Hirschi, R., Meynet, G., & Maeder, A. 2004, *A&A*, 425, 649 (HMM)
- Hofmeister, E., Kippenhahn, R., & Weigert, A. 1964, *Z. Astrophys.*, 59, 215
- Hubbard, W. B., & Lampe, M. 1969, *ApJS*, 18, 297
- Hui-Bon-Hoa, A. 2008, *Ap&SS*, 316, 55
- Huynh, H. T. 1993, *SIAM J. Numer. Anal.*, 30, 57
- Iben, I. 1975, *ApJ*, 196, 525
- Iben, I. 1991, *ApJS*, 76, 55
- Iben, I., & Ehrman, J. R. 1962, *ApJ*, 135, 770
- Iben, I., & MacDonald, J. 1985, *ApJ*, 296, 540
- Iglesias, C. A., & Rogers, F. J. 1993, *ApJ*, 412, 752
- Iglesias, C. A., & Rogers, F. J. 1996, *ApJ*, 464, 943
- Imbriani, G., et al. 2005, *Eur. Phys. J. A*, 25, 455
- Itoh, N., Hayashi, H., Nishikawa, A., & Kohyama, Y. 1996, *ApJS*, 102, 411
- Itoh, N., Totsuji, H., Ichimaru, S., & Dewitt, H. E. 1979, *ApJ*, 234, 1079
- Kippenhahn, R., Ruschenplatt, G., & Thomas, H.-C. 1980, *A&A*, 91, 175
- Kippenhahn, R., & Weigert, A. 1996, Stellar Evolution and Nucleosynthesis (New York: Springer-Verlag)
- Kippenhahn, R., Weigert, A., & Hofmeister, E. 1967, in Methods in Computational Physics, Vol. 7, ed. B. Alder, S. Fernbach, & M. Rotenberg (New York: Academic)
- Kolb, U., & Baraffe, I. 1999, *MNRAS*, 309, 1034
- Krishna Swamy, K. S. 1966, *ApJ*, 145, 174
- Kunz, R., Fey, M., Jaeger, M., Mayer, A., Hammer, J. W., Staudt, G., Harissopoulos, S., & Paradellis, T. 2002, *ApJ*, 567, 643
- Langanke, K., & Martínez-Pinedo, 2000, *Nucl. Phys. A*, 673, 481
- Lebreton, Y., et al. 2008, *Ap&SS*, 316, 1
- Lederer, M. T., & Aringer, B. 2009, *A&A*, 494, 403
- Lesaffre, P., Han, Z., Tout, C. A., Podsiadlowski, Ph., & Martin, R. G. 2006, *MNRAS*, 368, 187
- Limongi, M., & Chieffi, A. 2006, *ApJ*, 647, 483
- Limongi, M., Straniero, O., & Chieffi, A. 2000, *ApJS*, 129, 625 (LSC)
- Lodders, K. 2003, *ApJ*, 591, 1220
- Lugaro, M., Herwig, F., Lattanzio, J. C., Gallino, R., & Straniero, O. 2003, *ApJ*, 586, 1305
- Madhusudhan, N., Justham, S., Nelson, L., Paxton, B., Pfahl, E., Podsiadlowski, Ph., & Rappaport, S. 2006, *ApJ*, 640, 918
- Mattsson, L., Wahlin, R., & Höfner, S. 2010, *A&A*, 509, 14M
- Mocak, M., Müller, E., Weiss, A., & Kifonidis, K. 2009, *A&A*, 501, 659
- Mohr, P. J., Taylor, B. N., & Newell, D. B. 2008, *Rev. Mod. Phys.*, 80, 633
- Morel, P., & Lebreton, Y. 2008, *Ap&SS*, 316, 61
- Nieuwenhuijzen, H., & de Jager, C. 1990, *A&A*, 231, 134
- Nugis, T., & Lamers, H. J. G. L. M. 2000, *A&A*, 360, 227
- Oberkampf, W. L. 1998, Bibliography for Verification and Validation in Computational Simulation, Tech. Report SAND98-2041 (Albuquerque, NM: Sandia National Laboratories)
- Oda, T., Hino, M., Muto, K., Takahara, M., & Sato, K. 1994, *At. Data Nucl. Data Tables*, 56, 231
- Paczynski, B., & Proszynski, M. 1986, *ApJ*, 302, 519
- Pamyatnykh, A. A., Handler, G., & Dziembowski, W. A. 2004, *MNRAS*, 350, 1022
- Paquette, C., Pelletier, C., Fontaine, G., & Michaud, G. 1986, *ApJS*, 61, 197
- Patterson, J. 1998, *PASP*, 110, 1132
- Paxton, B. 2004, *PASP*, 116, 699
- Pietrinferni, A., Cassisi, S., Salaris, M., & Castelli, F. 2004, *ApJ*, 612, 168
- Pols, O. R., Tout, C. A., Eggleton, P. P., & Han, Zh. 1995, *MNRAS*, 274, 964
- Potekhin, A. Y., & Chabrier, G. 2010, *Contrib. Plasma Phys.*, 50, 82
- Press, W. H., Teukolsky, S. A., Vetterling, W. T., & Flannery, B. P. 1992, Numerical Recipes in C (Cambridge: Cambridge Univ. Press)
- Prialnik, D., & Kovetz, A. 1995, *ApJ*, 445, 789
- Rauscher, T., Heger, A., Hoffman, R. D., & Woosley, S. E. 2002, *ApJ*, 576, 323
- Rauscher, T., & Thielemann, F.-K. 2000, *At. Data Nucl. Data Tables*, 75, 1
- Reimers, D. 1975, *Mem. Soc. R. Sci. Liege*, 8, 369
- Renka, R. J. 1999, *ACM Algorithm 790*, *ACM Trans. Math. Software*, 25, 70
- Roache, P. J. 1998, Verification and Validation in Computational Science and Engineering (Albuquerque, NM: Hermosa)
- Rogers, F. J., & Nayfonov, A. 2002, *ApJ*, 576, 1064
- Roxburgh, I. W. 2008, *Ap&SS*, 316, 75
- Sakharuk, A., et al. 2006, in AIP Conf. Proc. 819, Capture Gamma-ray Spectroscopy and Related Topics: 12th Int. Symp., ed. A. Woehr & A. Aprahamian (Melville, NY: AIP), 118
- Saumon, D., Chabrier, G., & van Horn, H. M. 1995, *ApJS*, 99, 713
- Schwarzschild, M. 1958, Structure and Evolution of the Stars (Princeton, NJ: Princeton Univ. Press)
- Scuflaire, R., Theado, S., Montalban, J., Miglio, A., Bourge, P.-O., Godart, M., Thoul, A., & Noels, A. 2008, *Ap&SS*, 316, 83
- Seaton, M. J. 2005, *MNRAS*, 362, 1
- Serenelli, A. M., Basu, S., Ferguson, J. W., & Asplund, M. 2009, *ApJ*, 705, 123

- Serenelli, A., & Weiss, A. 2005, *A&A*, **442**, 1041  
 Shen, K. J., & Bildsten, L. 2009, *ApJ*, **699**, 1373  
 Soderlind, G., & Wang, L. 2006, *J. Comput. Appl. Math.*, **225**, 243  
 Starrfield, S., Sparks, W. M., Truran, J. W., & Wiescher, M. C. 2000, *ApJS*, **127**, 485  
 Steffen, M. 1990, *A&A*, **239**, 443  
 Stiriba, Y. 2003, *Appl. Numer. Math.*, **45**, 499  
 Strohmayer, T., & Bildsten, L. 2006, in *Compact Stellar X-Ray Sources*, ed. W. H. G. Lewin & M. van der Klis (Cambridge: Cambridge Univ. Press), 113  
 Sugimoto, D. 1970, *ApJ*, **159**, 619  
 Sugimoto, D., Nomoto, K., & Eriguchi, Y. 1981, *Progr. Theor. Phys. Suppl.*, **70**, 115  
 Suresh, A., & Huynh, H. T. 1997, *J. Comput. Phys.*, **136**, 83  
 Thomas, H.-C. 1967, *Z. Astrophys.*, **67**, 420  
 Thoul, A. A., Bahcall, J. N., & Loeb, A. 1994, *ApJ*, **421**, 828  
 Timmes, F. X. 1999, *ApJS*, **124**, 241  
 Timmes, F. X., & Swesty, F. D. 2000, *ApJS*, **126**, 501  
 Timmes, F. X., Woosley, S. E., & Weaver, T. A. 1995, *ApJS*, **98**, 617  
 VandenBerg, D. A. 2000, *ApJS*, **129**, 315  
 Ventura, P., D'Antona, F., & Mazzitelli, I. 2008, *Ap&SS*, **316**, 93  
 Vink, J. S., de Koter, A., & Lamers, H. J. G. L. M. 2001, *A&A*, **369**, 574  
 Weaver, T. A., Zimmerman, G. B., & Woosley, S. E. 1978, *ApJ*, **225**, 1021  
 Weinberg, N. N., Bildsten, L., & Schatz, H. 2006, *ApJ*, **639**, 1018  
 Weiss, A., Cassisi, S., Dotter, A., Han, Z., & Lebreton, Y. 2007, in *IAU Symp. 241, Stellar Populations as Building Blocks of Galaxies*, ed. A. Vazdekis & R. F. Peletier (Cambridge: Cambridge Univ. Press), 28  
 Weiss, A., & Schlattl, H. 2008, *Ap&SS*, **316**, 99  
 Woosley, S. E., Heger, A., & Weaver, T. A. 2002, *Rev. Mod. Phys.*, **74**, 1015 (WHW)  
 Woosley, S. E., et al. 2004, *ApJS*, **151**, 75  
 Worthey, G. 1994, *ApJS*, **95**, 107  
 Yakovlev, D. G., & Urpin, V. A. 1980, *SvA*, **24**, 303  
 Young, P. A., & Arnett, D. 2005, *ApJ*, **618**, 908  
 Zingale, M., Almgren, A. S., Bell, J. B., Nonaka, A., & Woosley, S. E. 2009, *ApJ*, **704**, 196